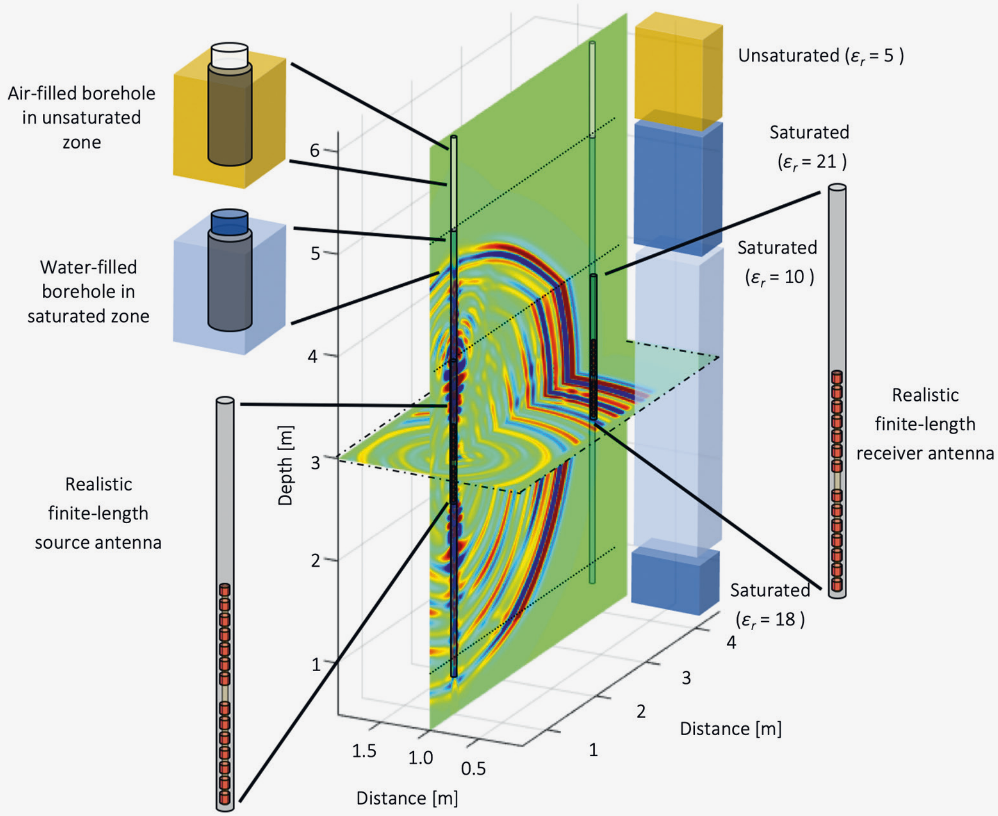

Towards 3D crosshole GPR full-waveform inversion

Amirpasha Mozaffari

Energie & Umwelt / Energy & Environment
Band / Volume 574
ISBN 978-3-95806-623-6

Mitglied der Helmholtz-Gemeinschaft

JÜLICH
Forschungszentrum

Schriften des Forschungszentrums Jülich
Reihe Energie & Umwelt / Energy & Environment Band / Volume 574

Forschungszentrum Jülich GmbH
Institut für Bio- und Geowissenschaften
Agrosphäre (IBG-3)

Towards 3D crosshole GPR full-waveform inversion

Amirpasha Mozaffari

Schriften des Forschungszentrums Jülich
Reihe Energie & Umwelt / Energy & Environment Band / Volume 574

ISSN 1866-1793 ISBN 978-3-95806-623-6

Bibliografische Information der Deutschen Nationalbibliothek.
Die Deutsche Nationalbibliothek verzeichnet diese Publikation in der Deutschen Nationalbibliografie; detaillierte Bibliografische Daten sind im Internet über http://dnb.d-nb.de abrufbar.

Herausgeber und Vertrieb:	Forschungszentrum Jülich GmbH Zentralbibliothek, Verlag 52425 Jülich Tel.: +49 2461 61-5368 Fax: +49 2461 61-6103 zb-publikation@fz-juelich.de www.fz-juelich.de/zb
Umschlaggestaltung:	Grafische Medien, Forschungszentrum Jülich GmbH
Druck:	Grafische Medien, Forschungszentrum Jülich GmbH
Copyright:	Forschungszentrum Jülich 2022

Schriften des Forschungszentrums Jülich
Reihe Energie & Umwelt / Energy & Environment, Band / Volume 574

D 82 (Diss. RWTH Aachen University, 2022)

ISSN 1866-1793
ISBN 978-3-95806-623-6

Vollständig frei verfügbar über das Publikationsportal des Forschungszentrums Jülich (JuSER) unter www.fz-juelich.de/zb/openaccess.

تقدیم به پدر و مادرم برای همه فداکاری‌ها, مهربانی‌ها و بزرگواری‌ها

"Far better an approximate answer to the right question, which is often vague, than an exact answer to the wrong question, which can always be made precise."

John W. Tukey, 1962 , Future of data analysis

Abstract

High-resolution imaging of the subsurface improves our understanding of the subsurface flow and solute transportation that can directly help us protect groundwater resources and remediate contaminated sites. The ground penetrating radar (GPR) is a useful non/minimal invasive method that consists of a transmitter (Tx) unit that emits electromagnetic (EM) waves and a receiver (Rx) that measures the arriving electromagnetic waves and can provide high-resolution tomograms of the subsurface properties.

In specific, the crosshole GPR setup in which two-neighbouring boreholes are placed in the earth can provide much more in-depth access to the target area. However, the interpretation of the GPR data remains challenging. The simpler ray-based inversion (RBI) is computationally attractive while fail to provide high-resolution tomograms as the results always smoothed over the target area. The full-waveform inversion (FWI) can provide detailed subsurface tomograms that can carry up to more than an order of the magnitude resolution compared to RBI from the same data set. A sophisticated method such as FWI requires detailed modelling tools and powerful inversion algorithm that needs significant computational resources. In last decades, by exponential increase in computing power and the memory, alongside to wider usage of high performance computing resources; FWI application in GPR data gain popularity. All these computational advances such as FWI method. could be very demanding to be modelled in 3D domain. Thus, some fundamentals assumptions are made to reduce the computational requirements, especially computational time and required memory by using 2D modeling domain. Despite the usefulness of these simplifications, these assumptions led to introducing inaccuracy that compromises the performance of the FWI in complex structures. We investigated the effect of the assumption that enables us to use a 2D model instead of a computationally expensive 3D modelling to simulate the EM propagation. These assumptions are made for specific state that not necessary is always valid, and therefore it can introduce inaccuracies in transferred data. Study of several synthetic cases revealed that the performance of the 3D to 2D transformation in complex structures such as high contrast layer is much lower than what is anticipated. Therefore, in the complex subsurface system; 2D transferred data inherently carry inaccuracy that jeopardises the accuracy of any further analysis such as FWI. Thus, we introduced a FWI that utilise a native 3D forward model to use the original measured 3D data. The novel method is called 2.5D FWI, and it showed improvements compared to 2D FWI for synthetic and measured data.

A better modelling tool such as the 3D forward model provides a useful platform for simulating the subsurface and measuring devices involved to a higher degree of accuracy. We used previously introduced 3D forward model to build a realistic model

of the GPR Tx and Rx antenna that called finite-length antennas and the boreholes that these antenna are placed to carry out the measurements. Our studies showed that realistic antenna and borehole-fluid representation provides more realistic travel-time and wave-form shape for GPR data. These more accurate simulated data increases the accuracy of the FWI results as reducing the uncertainty in the inversion system.

It is a known issue for GPR community that EM waves that travelled with a high-angle between the Tx and Rx shows inconsistency in their travel-time and therefore could jeopardise travel-time inversion results. Even though this effect is almost consistent, there was no concerts reason for this issue except systematic erroneous measurements. Thus, it is common pre-processing standard to discard these high-angle data (usually above 50°). Our findings regarding the contribution of the borehole-fluid to changes in travel-time of the EM waves showed the high-angle travel-time is not an error rather than consistent effect the borehole-fluid in travel times. We laid the mathematical explanation of this phenomena and introduced a correction method that could predict this issue and compensate for it. Lastly, we applied this correction method on the realistic synthetic data and showed that RBI results improved when the correction method is used.

Zusammenfassung

Die hochauflösende Bildgebung des Untergrunds verbessert unser Verständnis der unterirdischen Strömung und des Transports von gelösten Stoffen, was uns direkt dabei helfen kann, Grundwasserressourcen zu schützen und kontaminierte Standorte zu sanieren. Das Bodenradar (GPR) ist eine nützliche, minimalinvasive Methode, die aus einer Sendeeinheit (Tx), die elektromagnetische (EM) Wellen aussendet, und einem Empfänger (Rx) besteht, der die ankommenden EM-Wellen misst und hochauflösende Tomogramme liefern kann.

Insbesondere kann eine crosshole GPR-Anordnung, bei der zwei benachbarte Bohrlöcher in der Erde platziert werden, einen viel tieferen Zugang zur Zieltiefe ermöglichen. Allerdings bleibt die Interpretation der GPR-Daten eine Herausforderung. Die einfacheren Strahlenbasierte Inversion (SI) sind zwar rechnerisch attraktiv, liefern aber keine hochauflösenden Tomogramme. Die Vollewellenforminversion (VWI)-Methode liefert detaillierte Tomogramme des Untergrunds, die im Vergleich zu (SI) aus demselben Datensatz mehr als eine Größenordnung an Auflösung aufweisen können. Andererseits erfordert eine anspruchsvolle Methode wie VWI detaillierte Modellierungswerkzeuge und einen leistungsstarken Inversionsalgorithmus, der erhebliche Rechenressourcen benötigt.In den letzten Jahrzehnten hat die exponentielle Zunahme der Rechenleistung und des Speichers neben der breiteren Nutzung von Hochleistungs-Rechenressourcen dazu geführt, dass die Anwendung von VWI in GPR-Daten immer beliebter wird. Trotz all dieser rechnerischen Fortschritte könnte die VWI-Methode sehr anspruchsvoll sein. Daher werden einige grundlegende Annahmen getroffen, um die Berechnungsanforderungen zu reduzieren. Trotz der Nützlichkeit dieser Vereinfachungen führten diese Annahmen zur Einführung von Ungenauigkeiten, die die Leistung des VWI in komplexen Strukturen beeinträchtigen. In Kapitel 3 haben wir die Auswirkung der Annahme untersucht, die es uns ermöglicht, ein 2D-Modell anstelle einer rechenaufwendigen 3D-Modellierung zur Simulation der EM-Ausbreitung zu verwenden. Trotz der Nützlichkeit der 2D-Modellierung zur Reduzierung der Rechenzeit und des benötigten Speichers basiert sie auf Annahmen, die eine Plattform zur Übertragung der gemessenen 3D-Daten auf eine hypothetische 2D-Domäne bieten. Diese Annahmen werden für bestimmte Zustände getroffen, die nicht immer erfüllt sein müssen, und daher kann es zu Ungenauigkeiten in den übertragenen Daten kommen. Die Untersuchung mehrerer synthetischer Fälle hat gezeigt, dass die Leistung der 3D-zu-2D-Transformation in komplexen Strukturen wie einer kontrastreichen Schicht (Wellenleiter) viel geringer ist als erwartet. Daher sind die übertragenen 2D-Daten in einem komplexen Untergrundsystem von Natur aus mit Ungenauigkeiten behaftet, die die Genauigkeit jeder weiteren Analyse,

wie z. B. Die VWI, gefährden. Daher haben wir ein VWI eingeführt, das ein natives 3D-Vorwärtsmodell verwendet, um die ursprünglichen gemessenen 3D-Daten zu nutzen. Die neue Methode wird 2,5D VWI genannt und zeigte Verbesserungen im Vergleich zu 2D VWI für synthetische und gemessene Daten.

Ein besseres Modellierungswerkzeug wie das 3D-Vorwärtsmodell bietet eine nützliche Plattform für die Simulation des Untergrunds und der beteiligten Messgeräte mit einem höheren Genauigkeitsgrad. In Kapitel 4 haben wir das zuvor eingeführte 3D-Vorwärtsmodell verwendet, um ein realistisches Modell der GPR Tx und Rx Antenne, die Resisitiv belastete Antenne mit endlicher Länge (RLFLA) genannt wird, und der Bohrlöcher, in denen diese Antenne zur Durchführung der Messungen platziert wird, zu erstellen. Unsere Studien haben gezeigt, dass eine realistische Darstellung der Antenne und des Bohrloch-Fluids realistischere Laufzeiten und Wellenformen für GPR-Daten liefert. Diese genaueren simulierten Daten erhöhen die Genauigkeit der VWI-Ergebnisse, da sie die Unsicherheit im Inversionssystem verringern.

Es ist ein bekanntes Problem für die GPR-Gemeinschaft, dass EM-Wellen, die mit einem großen Winkel zwischen Tx und Rx verlaufen, Inkonsistenz in ihrer Laufzeit zeigen und daher die Ergebnisse der Laufzeitinversion gefährden könnten. Auch wenn dieser Effekt nahezu konsistent ist, gab es keinen konzertierten Grund für dieses Problem, außer systematischen Fehlmessungen. Daher ist es ein üblicher Vorverarbeitungsstandard, diese Daten mit hohem Winkel (normalerweise über 50°) zu verwerfen. Unsere Ergebnisse bezüglich des Beitrags des Bohrloch-Fluids zu den Änderungen der Laufzeit der EM-Wellen zeigten, dass die Hochwinkel-Laufzeit kein Fehler ist, sondern dass das Bohrloch-Fluid einen konsistenten Einfluss auf die Laufzeiten hat. In Kapitel 5 haben wir die mathematische Erklärung dieses Phänomens gelegt und eine Korrekturmethode eingeführt, die dieses Problem vorhersagen und kompensieren kann. Schließlich haben wir diese Korrekturmethode auf die realistischen synthetischen Daten angewendet und gezeigt, dass sich die Ergebnisse von SI verbessern, wenn die Korrekturmethode verwendet wird.

Publications

At the time of writing this dissertation, parts of the doctoral thesis have been published by scientific journals and contributed to scientific meetings as specified in chronicle order as below.

(1) Klotzsche, A., van der Kruk, J., **Mozaffari, A.**., Gueting, N., & Vereecken, H. (2015). *Crosshole GPR full-waveform inversion and waveguide amplitude analysis: Recent developments and new challenges.* 2015 8th International Workshop on Advanced Ground Penetrating Radar, IWAGPR 2015, July. `https://doi.org/10.1109/IWAGPR.2015.7292647`

(2) **Mozaffari, A.**, Klotzsche, A., He, G., Warren, C., Giannopoulos, A., Vereecken, H., & van der Kruk, J. (2016). *Towards 3D full-waveform inversion of crosshole GPR data.* GPR Conference 2016, 5–8. `https://doi.org/10.1109/ICGPR.2016.7572687`

(3) van der Kruk, J., Liu, T., **Mozaffari, A.**., Gueting, N., Klotzsche, A., Vereecken, H., Warren, C., & Giannopoulos, A. (2018). *GPR full-waveform inversion, recent developments, and future opportunities.* 2018 17th International Conference on Ground Penetrating Radar, GPR 2018, May 2020, 1–6. `https://doi.org/10.1109/ICGPR.2018.8441667`

(4) **Mozaffari, A.**, Klotzsche, A., Warren, C., He, G., Giannopoulos, A., Vereecken, & H., van der Kruk, J. (2020). *2.5D crosshole GPR full-waveform inversion with synthetic and measured data* . Geophysics, 85(4), H71–H82. `https://doi.org/10.1190/geo2019-0600.1`

(5) **Mozaffari, A.**, Klotzsche, Zhou, Z., A., Vereecken, H., & van der Kruk, J. (2021). *3D electromagnetic modelling explains the apparent velocity increase in crosshole GPR data - borehole fluid effect correction method enables the incorporation of high-angle travel time data* . IEEE Transactions on Geoscience and Remote Sensing, 1–10. `https://doi.org/10.1109/TGRS.2021.3107451.`

Contents

Chapter 1

Introduction

1.1 All is about the earth and climate

I am writing this thesis in 2020, a year most probably strangest year ever I had (and probably you), where nothing is familiar. A year that started with the highest average temperature ever recorded [10] followed by one of the worst wildfire disasters in modern history in Australia [54], continued and continuing with an unprecedented global pandemic and health crisis , a massive wildfire in California [129],... and the list goes on and on. It made me think about why I am getting a PhD in environmental science, while clearly we are failing, and the writing is on the wall. We are going down and down every year. When I was researching about the fact of how far we are from normalcy in 2020, I came across some news that was not all bad. For the first time, earth overshoot day is shifted back almost 20 days, short term air quality improvement in cities both due to Covid-19 lock-downs and much less travel in the world [127, 106, 64]. It made me realise that regardless of how huge is our problems in hand, we still have an extreme effect on our environment, and yet we can change the path if we believe that our livelihood depends on it (literally). So, I want to believe that we still can change it. I think the United Nations (UN) sustainable development goals (SDG) and 2016 Paris agreement are our most immense collective effort to address the most significant threats that humanity ever faced. Therefore, I wanted to formulate my thesis in the context of the SDG goal, and how I hope my work could be a grain in our collective effort to make tomorrow better. So, I tell that one somebody who opened this thesis; the introduction of this work will talk about why it is more vital than ever to invest in science and look up to it to find a way out of what we are.

1.2 Statement of the problem

SDG with its 17 goals could be a good indicator for what we as humankind should try to achieve in the upcoming years [158]. As a knowledge society, we necessarily rely on scientific research, when we try to chart the course towards a sustainable future. In the context of sustainability; earth and environmental sciences could contribute prominently to furthering the SDG agenda [140]. Earth and environmental sciences have enormous scope from inner-core to the last layer of the atmosphere (exosphere). Despite the vast size diameter of the earth; only a few kilometres of surface and near-surface environment of earth sustains nearly all terrestrial life. This *"heterogeneous, near-surface environment in which complex interactions involving rock, soil, water, air, and living organisms regulate the natural habitat and determine the availability of life-sustaining resources"* is called earth's critical zone [122]. This zone also serves as the repository for most of our municipal, industrial, and governmental wastes and contaminants, intentional or otherwise [138]. The study of the critical zone is an interdisciplinary field of research exploring the interactions among the land surface, vegetation, and water bodies that the extend of the survey include the pedosphere, unsaturated vadose zone, and saturated groundwater zone [19]. Geophysics and especially near-surface geophysics play a crucial role to study the critical zone. Near-surface use the geophysical methods to investigate the nature of small-scale features of the very outermost part of the earth's crust. These methods are closely related to applied geophysics or exploration geophysics with vast applications in engineering, geotechnical, environmental, groundwater, mining, archaeological and biogeochemical [25].

The groundwater constitutes over the 95% of the earths unfrozen freshwater. It often represents only freshwater resources in areas with limited or polluted surface waters for the agriculture, production and the drinking water. Meanwhile, the ever increasing demands for fresh water and pollution lead to depletion of clean groundwater resources in many parts of the world [166]. In the area with limited freshwater, the right to access to these resources led to conflicts between countries, states and groups that termed "water conflicts", that expected to be seen more in upcoming years [56, 9].The world health organisation (WHO) and UN consider the protecting the quality of the ground water and securing its sustained availability a priority goal for the sustainability and the peace of the earth in both the present and the future [158, 176].

From 17 SDGs, three goals (2:zero-hunger; 6:clean water and sanitation and 15:life on land), are directly and many more are in-directly related to the groundwater and its sustainable consumption. The field of the hydrogeophysics is the intersection of the geophysics and the water-resources engineering that has developed in recent years to investigate the potential that geophysical methods hold for providing quantitative information about subsurface hydrogeological parameters, or processes [138]. The hydrogeophysics delivers a suite of tools that may assist in addressing the demands on the provision of suitable quantities of groundwater at appropriate quality; determining the legacy of industrial, agricultural, and military sources of groundwater contamination; quantifying terrestrial carbon cycling feed-backs to climate; ensuring food security, and understanding water resource impacts on ecosystem function through the quantification of the structure and function of the shallow subsurface [16]. The scope of the collected data vary from satellites and aircraft in the regional scale (10^1 - 10^5m), at the ground surface in the local scale (10^{-1} - 10^2m) and within and between boreholes in the point scale (10^{-4} - 1m). The goal of securing sustainable and adequate water resources is required precise understanding of the flow and transportation process in aquifers that rely heavily on the hydrogeophysics methods [70, 77]. The aquifer structure could contain decimetre-scale heterogeneity that has a profound implication on the monitoring and remediation processes that are carried out in subsurface. These heterogeneities could be a layer with a material that has different material, or it could be preferential flow paths or impervious clay zones [181, 59]. Thus, an accurate estimation of the localisation of the heterogeneity plays a crucial role in to identify the nature of the heterogeneous layer, which most of traditional aquifer characterisation methods come short. Most of these methods are operating in a small spatial sampling scale and high resolution such as slug tests and logging tools; or with an average resolution over a large volume, such as pumping or tracer tests [20]. The hydrogeophysics methods like seismic, electrical resistivity tomography (ERT) and ground penetrating radar (GPR) can bridge this gap [15, 99, 42, 143, 16]. Especially, GPR; which its higher frequency range can provide the highest tomography resolution in aquifer studies in compare to ERT and seismic [42]. Moreover, implementing a GPR setup requires much less time compared to ERT. Furthermore, GPR has significant potential to characterise the saturated aquifer and the vadose zone either as non-invasive surface method, or as minimally-invasive crosshole GPR method [156, 15, 105, 85]. Moreover, GPR sensitivity to water content provides a technique for the mapping water table, perched water tables, and groundwater contamination [138, 5].

1.3 GPR to bridge the gap

GPR is a well-accepted non-invasive geophysical method of choice for many applications. The method uses radio waves to probe the “the ground” or any low loss dielectric material that nowadays equally applied to other media such as wood, concrete, and asphalt. GPR has a wide range of applications due to long list of lossy dielectric material environments and the broad radio frequency spectrum. The most common form of GPR measurements deploys a transmitter and a receiver in, which are moved over the surface to detect reflections from subsurface features. Despite a wide range of application for surface GPR, the depth of investigation is limited to tens of meters as reflected signals will be too attenuated before reaching to the receivers located on the surface in much deeper [5, 138, 4]. A crosshole GPR setup extends the investigation depth significantly as it is illustrated in a figure (1.1). Crosshole GPR can be used to map the spatial distribution of subsurface properties on full cross-sections directly at the location of interest.The two-dimensionality of the tomographic images provides the opportunity to characterise the lateral distribution of structures and to evaluate their architecture and connectivity. The combination of these features led to crosshole GPR has gained popularity amongst geophysical methods for high resolution tomography of the near surface in a wide field of applications in last three decades [69, 142, 154, 105, 85, 44, 59].

Figure (1.2) shows the two most commons methods of crosshole GPR transilumination setups . The zero offset profiling (ZOP) is a quick and straightforward survey method to locate the areas that electromagnetic (EM) velocity change drastically or lose energy (velocity anomalies or attenuation zones that discussed in chapter 2). As this method is easy and quick, normally it is used as preliminary method for assessing the experiment field and its finding can be used a prior information for next steps of studies to follow. The transmitter (Tx) and receiver (Rx) are moved from one station to next station in synchronous shift. Second most common method for GPR measurements is to use multi-offset gather (MOG) that provides the basis for tomographic imaging. The objective of MOG is to measure a large number of rays with different angels passing through the volume between the boreholes. This aim is achieved by fixing a Tx in a single depth and then lower the Rx in the second borehole until the entire borehole depth is covered as it illustrated in figure (1.2). Then the Tx is lowered to next station and the Rx stations is repeated for next combination [53, 4].

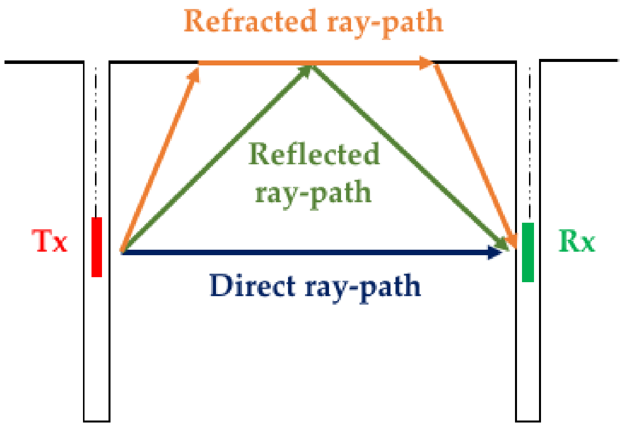

Figure 1.1: Crosshole GPR setup including Tx, Rx, direct, reflected and refracted ray-paths illustrated based on Annan [4] with some modification.

In this thesis, whenever author refer to GPR, it means crosshole GPR ; except explicitly said otherwise.

1.4 The need for better tools

Despite the advantages of applying the GPR in hydrogeological site characterisation ; there is a significant difficulties. The interpretation of geophysical data almost always relies on inversion methods, because most of the times, there is not enough data to lead to a unique solution. The surface and crosshole GPR data are also

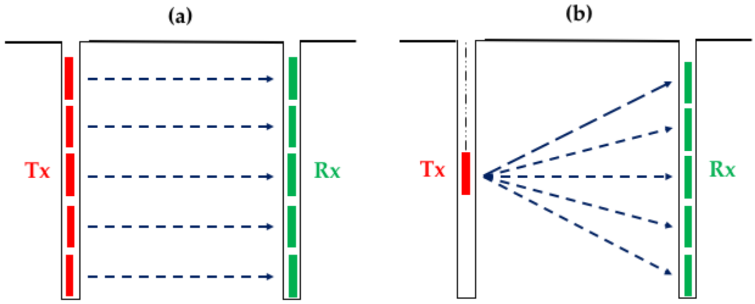

Figure 1.2: (a) ZOP and (b) MOG surveys illustrated based on Annan [4] with some modification.

not except non-deterministic (the solution is not unique) nature of the inversion. A non-deterministic system allows different models to predict the same outcome, and all be acceptable [8, 152]. The conventional geophysical inversion techniques are often limited in spatial resolution, thus yielding only relatively smooth images of the subsurface. Consequently, it is expected that the results of these methods suffer when the goal is to describe solute transport that could depend on small-scale structures acting as preferential flow paths or flow barriers [180]. In addition to this challenge, the absence of the direct and universal relationship between the geophysical hydrogeological properties makes the interpretation of the geophysical data even harder [16].

Ground-breaking work by Tarantola and Valette [153] laid the foundation of the high-fidelity data fitting technique for seismic data known as full-waveform inversion (FWI). FWI consists of a forward model that simulates the earth response and a cost function that tries to reduce the differences between the simulated data and the measured data. In contrast to conventional inversion method, FWI incorporates the entire waveform (or at least the first few cycles) of the signal that can drastically improve the resolution of the tomograms [177, 40, 133, 39, 12, 165, 167]. Within the last two decades, FWI was adapted for EM wave propagation, especially for crosshole FWI. Kuroda, Takeuchi, and Kim [89] introduced a time-domain 2D FWI for synthetic studies. At the same time, independently Ernst et al. [47] developed a 2D FWI that utilise a gradient-based method to obtain high resolution tomograms, and applied it to synthetic and experimental data [46]. Meles et al. [110] extended the method by incorporating the vector-based properties of the EM fields into the FWI and simultaneous update of the fields.

Since the initial application, GPR FWI has been continuously developed to enhance the application to experimental data, and multiple field applications have been conducted, including the characterisation of aquifers [80, 59], karst [78], and clayey till

[104]. Studies related to the Widen site [80] and the Boise hydrogeophysical test site [84] specifically indicated the potential of FWI to obtain high-resolution subsurface images including high-contrast layers that were not able to be detected by ray-based inversion (RBI). Such layers are important to accurately map and detect because they can be linked to hydrologically relevant features such as high porosity zones, preferential flow paths, and impermeable clay lenses that can significantly effect to flow and transport characteristic of aquifers. High resolution 2D forward modelling demonstrates that such high contrast layers, related to an increased permittivity, can act as low-velocity waveguides causing late arrival high amplitude events in the data. Next to the time-domain approaches, several frequency-domain FWI approaches have been developed in the last few years. For example, Lavoué [94] proposed a frequency-domain 2D FWI that could reconstruct the ε_r and σ of multi-offset GPR for a synthetic model. An overview of the current state-of-the-art of crosshole GPR FWI and its application to experimental data is provided by Klotzsche, Vereecken, and van der Kruk [79].

Almost all crosshole GPR FWI studies are carried out in the 2D domain that is computationally attractive. To use a 2D modelling tool, it is necessary to transfer the 3D measured data to an equivalent 2D domain [161]. Despite the usefulness of the 2D modelling to reduce the computational intensity, it is based on assumptions that limit its applications and reliability. Moreover, 2D modelling fails to capture complex structures and therefore, it can not realistically simulate the natural propagation of the EM. A 3D modelling tool makes a 3D to 2D transformation redundant. Besides, a more realistic tool incorporates the small-scale features such as borehole-filling, borehole-casing, GPR system and antennas that improve the simulated data. Thus, our understanding of the subsurface and EM propagation in the subsurface medium could be improved by utilising better tools. Finally, applying a detailed 3D modelling tool can be used to explain phenomena that can not be explained by rudimentary modelling tools.

1.5 Objective and thesis outline

A previous section, showed that we need better tools to utilise all that GPR has to offer. This thesis has two main objectives. The primary objective is to improve the performance and accuracy of the crosshole GPR FWI for investigating the subsurface. The secondary aim is to refine the understanding of the physics behind the EM wave propagation in crosshole GPR setup that can eventually enhance the effectiveness of the FWI as well. In the contexts of this thesis; we formulate these objectives as the following hypothesis:

(1) A 3D to 2D transformation negatively effects the conductivity tomograms obtained by FWI. This issue can be addressed by utilising a fully 3D modelling tool that doesn't need a 3D to 2D transformation.

(2) A borehole-fluid has a significant impact on the EM wave's velocity, and

therefore on resulted permittivity tomograms. By including a borehole-fluid into a forward model, the FWI for permittivity will improve.

(3) Borehole-fluid and GPR antenna have simultaneous and elaborate effect on the GPR data that is hard to isolate. Including these models into a forward model, will improve the consistency of the FWI.

(4) A borehole fluid presence contributes to an inconsistency in crosshole GPR inversion when the incident angle is increased. This issue is well-known, but it is not well-described. A detailed 3D model that includes borehole-fluid; could quantify the effect.

The hypothesis 1,2 and 3 and 4 were investigated in the chapter (3), chapter (4) and chapter (5), respectively. Chapter (2) contain the general theory about the fundamental of the EM and GPR system. It follows with short description about the numerical modelling and its application for GPR modeling. Chapter (2) ends by short review of the inversion problem and its implication on GPR RBI and FWI. Chapters (3-5) each include a specific introduction, a description of the methods used, and a discussion of the obtained results. The remaining manuscript is organised as follows:

Chapter (3) investigates the possible drawbacks of 2D FWI due to utilising an asymptotic transformation to convert the 3D acquired data to the 2D domain. The new 2.5D crosshole GPR FWI is introduced that utilise a complete 3D forward model and its performance is compared against the more conventional 2D FWI. In following, several optimisation strategies were examined to reduce the computational intensity of multiple times 3D modelling. Lastly, the application of the 2.5D crosshole GPR FWI is verified for experimental data.

Chapter (4) introduces a detailed borehole-fluid and crosshole GPR antenna model to increase the realism of the simulated data. In following, these models are used to investigate the possible effect of the borehole-fluid and GPR system on travel times and wavelet angular-dependency for synthetic and previously measured data. These models are combined in a single 3D forward model that provides multi-offset full-wave traces for any arbitrary subsurface model with fine-discretisation. Lastly, we incorporate the borehole-fluid model into the 2.5D crosshole GPR FWI (that was introduced in chapter 3) and performance of the 2D FWI, 2.5D FWI vanilla and 2.5D FWI with borehole-fluid model integrated is compared for synthetic data.

In chapter (5), 3D borehole-fluid and GPR antenna models (that are introduced in chapter 4) are used to investigate the increased apparent velocity of EM waves by increasing the ray-path angles in GPR setup. In following, a novel pre-processing method is introduced that can correct for increased apparent velocity by making use of wide angular aperture while ensuring the consistency inversion results. Lastly, the pre-processing method is verified for synthetic homogeneous and heterogeneous subsurface models.

Finally, Chapter (6) summaries the overall conclusions of this thesis and indicates possible future research directions.

Chapter 2

Theory

In this Chapter, first the fundamentals of EM wave propagation are introduced. After describing a basics of GPR, numerical modelling in GPR is discussed. Later, inversion and ill-posed and its application for inverting GPR data with RBI and FWI schemes are briefly explained.

2.1 Fundamental of electromagnetic wave

2.1.1 Fundamental of electromagnetic

Maxwell equations provide a fundamental platform to understand the behaviour of the EM and how to determine the electric and magnetic properties of materials [108]. First equation (2.1) declares that electric current flow causing the magnetic field:

$$\nabla \times \boldsymbol{H} = \boldsymbol{J} + \partial \boldsymbol{D}/\partial t, \tag{2.1}$$

where $\boldsymbol{H}$ is the magnetic field, $\boldsymbol{J}$ is the current density, and $\boldsymbol{D}$ is the electric displacement. The second equation (2.2) states that electric fields results from time-varying magnetic induction fields is:

$$\nabla \times \ \boldsymbol{E} = -\partial \ \boldsymbol{B}/\partial \ t, \tag{2.2}$$

where $\boldsymbol{E}$ is the electric field vector and $\boldsymbol{B}$ is the magnetic induction vector. Now let's take a look at some electrical properties of the materials. Constitutive equations describing the material responses to EM fields including three equations.

(i) Electrical conductivity (σ): We can us the Ohm's law to build a constitutive relationship between behaviour of the EM fields resulted from the Maxwell equations and the properties of the subsurface structure,

$$\boldsymbol{J} = \sigma \ \boldsymbol{E}, \tag{2.3}$$

where σ is electrical conductivity of the medium and because $\boldsymbol{E}$ and $\boldsymbol{J}$ are both vectors, σ must be tensor. The inverse of the conductivity is called resistivity, which is used in various geophysical sounding or induced polarisation methods.

(ii) Dielectric permittivity (ε): This equation relates the electrical field intensity with displacement through defining dielectric permittivity ε and it is a tensor.

$$\boldsymbol{D} = \varepsilon\ \boldsymbol{E}, \tag{2.4}$$

In the free space vacuum, ε has defined value of $8.854 \times 10^{(-12)}$ F/m in free space. It is common to relate the dielectric permittivities values with the value of the free space ($\varepsilon_r = \frac{\varepsilon}{\varepsilon_0}$), which in this case is called relative dielectric permittivity and noted as (ε_r)

(iii) Magnetic permeability (μ): Third constitutive equations is relating the magnetic field strength and magnetic induction

$$\boldsymbol{B} = \mu\ \boldsymbol{H}, \tag{2.5}$$

where μ is defined as the magnetic permeability. In the absence of the material, the value of the magnetic permeability is equal to $4\pi 10^{-7}$ H/m.

2.1.2 EM wave propagation

We exploit the wave characteristic of EM fields for geophysical investigation. Maxwell's equations (2.1) and (2.2) describe a coupled set of electric and magnetic fields when the fields vary with time. Depending on the relative magnitude of energy loss (associated with conductivity) to energy storage (associated with permittivity and permeability), the fields may diffuse or propagate as waves. Such solutions are referred to as plane wave solutions to Maxwell's equations. For the GPR system, we are mostly interested in the EM, and it has the following form:

$$\boldsymbol{E} = f\left(\boldsymbol{r}, \boldsymbol{k}, t\right) \hat{u}, \tag{2.6}$$

where $\boldsymbol{r}$ is a vector describing spatial position and $f\left(\boldsymbol{r}, \boldsymbol{k}, t\right)$ satisfies the scalar equation below

$$\partial^2 / \left(\partial \beta^2\right) f\left(\beta, t\right) - \mu \sigma \partial / \partial\ t f\left(\beta, t\right) - \mu \varepsilon \partial^2 / \left(\partial t^2\right) f\left(\beta, t\right) \equiv 0, \tag{2.7}$$

where $\beta = \overline{r}.\hat{k}$ k is distance in the propagation direction. In low-loss conditions

$$f\left(\beta, t\right) \approx\ f\left(\beta \pm v\ t\right) e^{(\pm \alpha \beta)}, \tag{2.8}$$

where $\boldsymbol{v}$ and α are velocity and attenuation. The real part of the bulk dielectric permittivity in natural medium can be derived with c as the radar wave velocity in air ($< 0.3 \frac{m}{ns}$) and for high frequencies, low loss and non-magnetic materials as $\mu \approx 1$ and $\mu = \mu_0.\mu_r$ with $\mu_0 = 4\pi 10^{(-7)}$ H/m [100].

$$\boldsymbol{v} = \frac{c}{\sqrt{\varepsilon}} \tag{2.9}$$

For high frequency and low loss attenuation and electrical properties, with σ as electrical conductivity in mS/m and μ relative permittivity, the following formula used to calculate the attenuation of the signal:

$$\alpha = \frac{\sigma}{2}\sqrt{\frac{\mu}{\varepsilon}} \tag{2.10}$$

The table (2.1), includes a list of most common material and their corresponding ε_r, σ , velocity v and α attenuation values [100].

Table 2.1: Permittivity ε_r, conductivity σ, velocity v, and attenuation α for selected materials for a frequency of 100 MHz [100].

	$\varepsilon_r[-]$	$\sigma[mS/m]$	$v[m/ns]$	$\alpha[dB/m]$
air	1	0	2.998	0
fresh water	80	0.5	0.033	0.1
salt water	80	30 000	0.01	1000
dry sand	3 - 5	0.01	0.15	0.01
saturated sand	20 - 30	0.1 - 1	0.06	0.03 - 0.3
silt	5 - 30	1 - 100	0.07	1 - 100
clay	5 - 40	2 - 100	0.06	1 - 300
limestone	4 - 8	0.5 - 2	0.12	0.4 - 1
granite	6	0.01 - 1	0.12	0.01 - 1
dry salt	6	0.001 - 0.1	0.125	0.01 - 1
ice	3.18	0.01	0.168	0.02

2.1.3 Reflection and refraction of the EM waves

Figure (2.1) shows a simple case that a Tx placed on the surface. The interface between the mediums (air and ground for figure 2.1) plays a crucial role in EM behaviour. The field at any point along the ground interface can be identified as a planner wave on the boundary based on the specific incidence angle defined by geometry by [4]. A ray-path is a path or a direction that EM field propagates and a signal is a path that emitted by a Tx and detected by a Rx. Most of the EM methods and especially GPR is depending on detecting of reflected or scattered signal. The *Snell's law* is a formula that describes the refraction at the medium interfaces as the ratio of the sinus of the incident angle θ_1 divided by the sinus of the transmitted angle θ_2, which equals the ratio of the two velocities or the inverse ratio of the squares of the ε_r in the first medium with ε_1 and the second medium with ε_2 [55].

$$\frac{\sin\theta_1}{\sqrt{\varepsilon_2}} = \frac{\sin\theta_2}{\sqrt{\varepsilon_1}}, \tag{2.11}$$

where $\sin\theta_1$ and $\sin\theta_2$ are the incident and transmitted angles with EM with ε_1 and ε_2 in the first and second mediums, respectively. This issue is discussed in more detail in chapter (4).

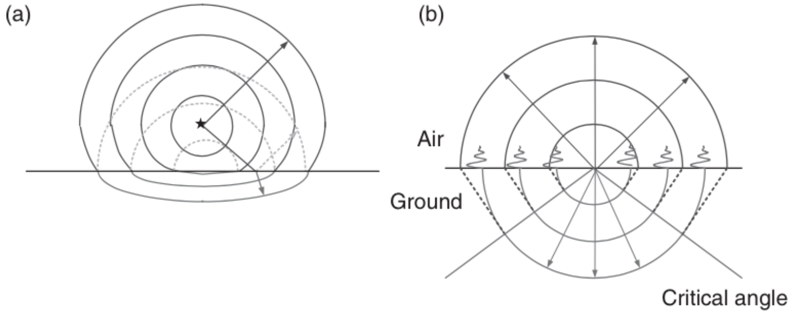

Figure 2.1: Wavefronts spreading out from a localised source. In (a), the source is located above the ground. The dotted lines indicate the reflected signal. In (b), the source is located on the air-ground interface. The dashed lines indicate refracted waves. The oscillating lines indicate evanescent waves, adopted from Annan [4].

2.2 Numerical modelling of GPR data

2.2.1 Finite-difference method

As it motioned in section (2.1), Maxwell [108] equations are governing the EM (equation 2.1), and to solve them numerically we use the differential equations methods by calculation their derivatives. A finite-difference methods (FDM), is one of the major numerical analysis tools to solve differential equations. The FDM approximates the sets of equations in a discretisation (time, space, frequency,...) and calculate the finite differences and the derivatives. FDM converts the linear differential equation and non-linear partial differential equations into a system of equations that can be solved by matrix algebra techniques which are suited for modern computation. In a wide range of FDM, **Finite-difference frequency-domain (FDFD)** and **finite-difference time-domain (FDTD)** are most common methods that both based on an essential same sets of equations where fields and devices are represented as points on arrays. The system solves these sets of equations for each of these array points and advances to next point. In FDFD these arrays are put into the matrix form and solved by using standard linear algebra methods for each specific frequency. For the FDTD system, setup is governed under a containing time-loop and try to solve the above equations for each time steps for every point on the grid and then advance to next time-step. In comparison, we can assume a FDFD system as a series of snapshots of the fields at specific frequencies, where FDTD is a movie of the evolution and scattering of the wavefront through the grid points before obtaining a solution for the system. FDFD is well suited for incorporating material dispersion, small or highly resonant structures, while FDTD is more suited for non-linear devices, transient phenomena and large and extremely large devices. Moreover, FDFD is significantly slower to simulate a 3D medium (except for fast iterative solver) due to difficulties with matrix inversions, whereas FDTD can easily handle large 3D devices as it is fully explicit solver [118, 130, 126]. As GPR setup is relatively large system and we are interested in modelling in 3D environment, all our future numerical solvers are using FDTD as their computing domain.

2.2.2 Finite-difference time-domain

As it was briefly mentioned before, the FDTD method belongs to differential numerical modelling methods. To implement an FDTD, a computational domain (*computing volume*) must first be established, which is a physical region over which the simulation will be performed. In this computational domain, the material of each cell in specifically permeability, permittivity, and conductivity must be defined. Then the time-dependent Maxwell's equations are discretised in the computation domain, using central-difference approximations to space and time partial derivatives. These resulting finite-difference equations are solved in a leap-frog manner where the electric field vector components in a specific spatial volume are solved at a given instant in time. In the next step, the magnetic field vector components are solved for the next instant in the same spatial volume. These two steps will lead to determined $\boldsymbol{E}$ and $\boldsymbol{H}$ fields (equations 2.1 and 2.2) at specific spatial-temporal instance [115, 130]. This chain of steps are repeated over and over again until the EM is fully solved. Figure (2.2) shows the 3D cube that introduced by Yee [178] (known as Yee's cell), who pioneered the FDTD techniques. The 2D FDTD cell is easily obtained by simplification of the 3D Yee cell [52].

2.2.2.1 Courant–Friedrichs–Lewy

As explained above, Maxwell's equations are discretised in both space and time and the solution is obtained in an iterative manner as EM fields propagate in FDTD grid, where each iteration corresponds to an elapsed simulated time of a Δt. The price of obtaining an explicit numerical solution in time-domain is that the value of temporal discretisation Δt and spatial discretisation (3D) Δx, Δy and Δz can not be assigned independently from each other. Simply, this stability condition ensures that information is not travelling faster than the speed of light. The Courant–Friedrichs–Lewy (CFL) stability condition is a requirement for the convergence in FDTD, while solving certain partial differential equations by imposing an upper threshold for an explicit time-marching solution [36]:

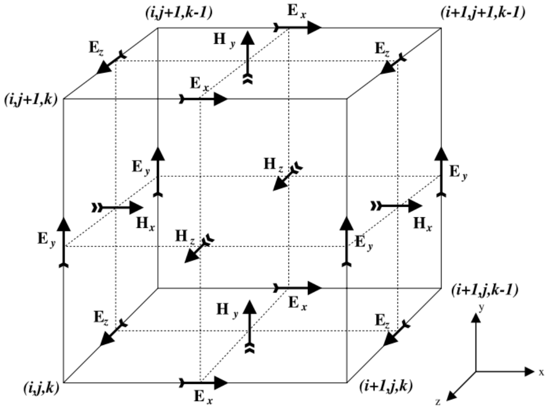

Figure 2.2: The Yee cell adopted from Giannopoulos [52].

$$\Delta t \leq \frac{1}{c\sqrt{\frac{1}{\Delta x^2} + \frac{1}{\Delta y^2} + \frac{1}{\Delta z^2}}}. \tag{2.12}$$

In the equation (2.12), c is the speed of light and the value of t is bounded by the values of Δx, Δy and Δz. The stability condition for the 2D case is simply obtained by introduce a $\Delta z \to \infty$. For more information about CFL please refer to Hagness and Taflove [60].

2.2.2.2 Perfectly matched layer

One of the most challenging issues of numerical modelling is to limit the computational domain. This issue is even more important for simulating the open-boundary nature of the GPR. There are several truncation methods including "Mur" absorbing boundary condition (ABC) , "Lio" ABC and various perfectly matched layer (PML). However, PML can provide orders-of-magnitude lower reflections from the surrounding boundaries. The PML is introduced by Berenger [14] and since then various formulation of it is produced and implemented. The PML (which is actually an absorbing region) is absorbing any waves impinging on its, hence simulating an unbounded space [123] and prevent multiple reflection from bounding box. For more information, please refer to Johnson [74].

2.3 Inversion and ill-posed problem

2.3.1 Inverse problem

In order to discuss the inversion, it is necessary to define the inverse problem. The pioneer of modern inversion, Tarantola [152] defines the inverse problem as *In the so called 'inverse problems', values of the parameters describing physical systems are estimated, using data that obtained with indirect measurements*. In the most general form, the inverse problem requires extensive use of random sampling (Monte Carlo methods), while some prior assumption about the data and distribution of the uncertainties can reduce the complexity and pave the way for analytical solutions [151, 152]. Inverse problem theory is originally introduced to deal with large under-deterministic geophysical problems. The solution for undetermined problems needs to full-fill a list of minimal constrains to be able to answer an inverse problem. The answer must be valid for both **linear** and **non-linear** problems. The formulation must be valid for both **over-determined** and **under-determined** problems. The formulation must be **consistent with respect to a change of variables**. The formulation must be general enough to allow **general error distribution** in data. The formulation must be general enough to allow for the formal incorporating of **any a priori assumption**. The formulation of must be general enough to **incorporate theoretical errors** in a natural way [7, 172, 137]. Tarantola and Valette [153] in their ground breaking work, demonstrated that inverse problem could be re-formulate by using a simple extension of the probability theory and information theory for a *finite sets of parameters*. Observation data and attached uncertainties, (a possibly vague) a prior information on model parameters, and a physical theory relating the model parameters to the observations are the fundamental elements of any inverse problem [152].

One of the matters that make the inverse problem different than the classical problem is the ill-posed nature of the inversion. In a well-posed problem, a solution exists, the solution is unique, and the solution behaviour changes continuously with the initial conditions. Therefore, a system outcome can be predicted at any given Spatio-temporal vicinity of the system. The forward or direct problem consists of this system model that can predict the outcome of possible experiments. The 'inverse problem' appears when we do not have a reliable model of the system, but we have a set of observation to infer a model system. It is under-determined (the solution is not unique) nature of the inverse problem that allows different models to predict the same outcome and all be *acceptable* [8, 152].

2.3.1.1 State of information

State of information is a complete description of a system and its defining parameters. In the most general format, it is defined as probability density over the parameter space. For a system, this information could be categorised as observed data (observable parameters), prior information on model parameters and theoretical information that physically correlate the observable parameters and the model parameters and can all be described by probability densities. The general inverse problem can then be set a problem of *"combining"* all this information. In following, the fundamental building block of the state of information is discussed. Any attempt to study any arbitrary system can be divided into the three steps; **parametrisation**, **forward modelling** and **inverse modelling** [153].

2.3.1.2 Parametrisation and prior information

Parameterisation: Any arbitrary physical system consists of a physical system in a narrow sense and a family of the measuring instruments and their outputs. A parameterisation is a particular choice of sets of parameters that define a system. When a group of specific parameters can describe the system, we may say the system is *parametrisable* [153]. These sets of parameters can be categorised as follows:

(i) **Model space**: Independently of any particular parameterisation, abstract space of point can be introduced that accommodate all conceivable model of the system that called *model space* and the parameters that needed to define a model space called *model parameters*.

(ii) **Data space**: We can thus arrive at the abstract idea of a data space, which can be defined as the space of all conceivable instrumental responses as a result of the measurements and these sets of parameters called *data parameters*

(iii) **Joint Manifold**: it is joint space of the model space parameters and Data space parameters and all possible other parameters and arguments that we can call *physical parameters* or simply *parameters*.

A prior information and measurements: We can divide the state of the information based on the dependency on the measurement itself. *Prior information (a priori information)* is the information obtained independently of the results of the measurements. The probability density representing this a priori information will be denoted by $\rho_M(m)$. In the other hand, there is some information that is obtained by the measurement, and as they are subject to uncertainties, they are not merely an "observed value" but rather a "state of information" acquired on some observable parameter. $\rho_D(d)$ denotes the observable parameters over the data space. The information that we have in both model parameters and observable parameters can then be described in the manifold of the joint manifold by the joint probability density. As it defined, prior information model parameters and observations are independent and therefore, joint possibility density will be [151, 152],

$$\rho(d, m) = \rho_D(d)\rho_M(m). \tag{2.13}$$

2.3.1.3 Forward problem

As Popper [132] stated, there is a cycle of physical theories suggested by experiments and physical theories predict the outcome of the experiments. The comparison between the expected outcomes and observed outcome allows us to examine the fundamental physical theories and unacceptably enormous disagreement could lead to refuting the theory. To solve a *forward problem*, means to map the outcome of the observable parameters d which corresponding to to a given model m. For a (usually non-linear) operator $g_m(.)$ that called *forward operator*, the theoretical predication can be noted as following [151]:

$$m \mapsto d = g(m), \tag{2.14}$$

where $d = g(m)$ is a short notation for the sets of equations that express our understanding of the physical system under study. For every model m, a different predicted associated value d can be assumed that we can denote with $\theta(d \mid m)$. Therefore, a *theoretical probability density* can be defined as a product of the conditional probability and probability density for model m as [152, 75]:

$$\theta(d, m) = \theta(d \mid m)\mu_M(m). \tag{2.15}$$

2.3.1.4 Defining the solution of the inverse problem

As the "physical theory" that we included in the physical parameters is describing the system under study, the "inverse problem theory" is about defining a quantitative rules for comparison between the predictions and observations. As it discussed before, joint prior probability density (equation 2.13) is representing both information obtained on the observable parameters (data) d and priori information on the model parameters m, while the theoretical probability density (equation 2.15) represents the information on the physical correlations between d and m based on the physical law. A combination of the two state of information produces the *a posteriori state of information*,

$$\sigma(d, m) = k\frac{\rho(d, m)\Theta(d, m)}{\mu(d, m)}, \tag{2.16}$$

where $\mu(d, m)$ represents the homogeneous state of information and where k is normalisation constant.

When the modelling system uncertainty is negligible compared to observational uncertainty and the data space is a linear space (the homogeneous probability density over data space is constant, $\mu_D(d) = const.$), the a posteriori state of information (equation 2.16) can be simplified.

$$\sigma_M(m) = k\rho_M(m)\rho_D(g(m)), \tag{2.17}$$

where k is normalisation constant. As equation (2.17) can be written as a conditional probability density as :

$$\sigma_M(m) = k\rho_M(m)L(m), \tag{2.18}$$

where $L(m)$ is the *likelihood function*

$$L(m) = \rho_D(g(m)), \tag{2.19}$$

which is a parameters to measures of *"how good a model m is in explaining the data"* [151, 152].

2.4 GPR ray-based inversion

The computational effort required to the solution of the equation (2.17) is strongly related to the joint manifold's degree of freedom. As the system is more flexible, and more data is presented to the system; it requires more non-linearity to accommodate all the information. The crosshole FWI RBI is imposing substantial restriction to the system data space and therefore; it is a common starting point to invert the GPR data without requiring significant computational resources. The standard RBI uses the **first-arrival travel times inversion** and the **first-cycle amplitude inversion** of the measured traces to determine the EM wave velocity and attenuation of the target medium. There are two most common ways to determine the possible pathways for travelling waves, straight travel paths (that consider the direct line connecting the Tx and Rx) and the curved travel path that considers the possible changes in the velocities along the way. The curved travel path method is based on Snell's law (equation 2.11) and it provides more realistic velocity distribution [92]. As stated in section (2.3.1.3); inversion uses a forward kernel that maps the the model parameters to observable parameters. A ray-tracing techniques is less computational intensive but its application is limited to homogeneous medium. A homogeneous medium can be parameterised effectively with piece-wise analytical functions [27, 28]. In contrast, the finite-difference Eikonal solver uses a regular grid points where each has an assigned velocity. The Eikonal solver requires the travel times of the all Tx and Rx pairs, which needs more memory and computational resources [164]. In this dissertation, whenever we refer to RBI; we used the curved ray-path, and the Eikonal solver as forward kernel. The travel time for the EM wave that travel through the 2D isotropic medium along the a ray-path S from a Tx to a Rx can be described by:

$$t = \int_S u(r(x,z))dr, \tag{2.20}$$

where $u(r)$ represents the slowness field ($u = \frac{1}{v}$) and $r(x,z)$ indicates the position vector. We can simplify the equation (2.20) by considering the constant slowness in each model cell u_k when the entire model space is divided to m cells $u_k \rightarrow k = 1...m$. Thus the travel time for arbitrary i-th travel time could be expressed as linear relationship as:

$$t_i = \sum_{k=1}^{m} l_{ik} u_k = \boldsymbol{L}_i \boldsymbol{u}, \tag{2.21}$$

where l_{ik} stands for the i-th portion of the ray path in the k-th cell of the model space.

The **first-arrival travel times inversion** is using the first-arrival travel times in the data to determine the velocity of the EM wave in the target medium where the velocity in the medium is inversely proportional to the ε_r [4]. The travel times RBI can be divided to following steps [92, 135]:

(i) To define an initial subsurface model (that we call model.);

(ii) Use the model to simulate the travel times for the subsurface model with the forward kernel;

(iii) Calculate the differences between the observed travel times and the simulated travel times;

(iv) Identify the possible changes in the model that will reduce the differences between the observed and simulated travel times;

(v) and update the model.

The steps 2 to 5 are repeated iterative until the difference between the simulated data and measured data is small enough. In order to quantify the difference a misfit function is calculated as :

$$C_{TT} = \sum_s \sum_r \frac{(t_{sr}^{obs} - t_{sr}^{syn})^2}{n}, \tag{2.22}$$

where t_{sr}^{obs} and t_{sr}^{syn} are the observed and synthetic travel times for the Tx positions x_s and Rx positions x_r. The number of data points is given by n, where s and r are the Tx and Rx numbers, respectively. To solve the equation (2.21) and determine the $\boldsymbol{L}$; the fine difference Eikonal solver divides the subsurface to a 2D rectangular grid. For each cell; a length of the ray-path can be determined by the assigned slowness (as Snell's law determine the refraction or reflection) in the manner that the EM wave travel time is matching the measured travel times. In most cases for heterogeneous medium; it is not possible to converge the modelled slowness field $\boldsymbol{u}$ without additional regularisation and damping. As the $\boldsymbol{L}$ in equation (2.21) depends on unknown slowness field u; the inversion tries to minimise the non-linear objective function C_{TT} in an iterative manner. For more information about the RBI for a curved-path with an Eikonal solver please refer to Lanz, Maurer, and Green [92] and Rabbel [135].

The **first-cycle amplitude inversion** uses the amplitudes from the first arrival picks to estimate the attenuation of the EM waves, where the attenuation is associated with the σ of the medium [67, 66]. The first-cycle amplitude RBI requires additional information such as radiation pattern in addition to travel times. The method has been further developed by including the antenna-borehole coupling effect, or other systematic errors. For more information, take a look at Holliger, Musil, and Maurer [67].

Despite the wide-spread application and minimal computational effort requirement for RBI; some critical shortcomings associated with the method. The resolution of the RBI tomogram is scaled by the first Fresnel zone $\sqrt{\lambda L}$, where λ is the wavelength and $\boldsymbol{L}$ is the total path. Therefore, RBI is mostly reliable for models that have a small variation of medium properties relative to the wavelength, and struggles with presence of high contrast layers [146, 173, 136, 22]. Moreover, due to inconsistency in travel time RBI for crosshole GPR; it is a common practice to limit the angular aperture [128] that affects the resolution of the tomograms. This specific issue is discussed in detailed in chapter (5). The RBI is less computationally intensive. But it only includes the first arrival times of the waves and corresponding first cycle amplitudes, which are relativity small fractions of the information contained in the recorded traces. By discarding this valuable information in favour of straight forward procedure; the non-linear Eikonal solver requires significant regularisation, smoothing, and damping to stabilise and constrain the inversion [67, 66]. Despite all of these challenges mentioned above, RBI provides a valuable first look into the target medium; especially ε_r. The information obtained by RBI about the ε_r ic commonly used as prior information for FWI.

2.5 GPR full-wavefrom inversion

2.5.1 Linear regression

The idea of linear regression and back-propagation as learning method was firstly introduced by Rumelhart, Hinton, and Williams [139], where an iterative weight adjustment network of connection suggested to minimise the the difference between the actual output vector of the net and the desired output vector. The logistic regression tries to estimate the probability of desired output $\hat{y} = P(y = 1 \mid x))$ for any given x. A linear regression output of this system will be $\hat{y} = w^T + b$. In order to compare the performance of the $\hat{y}^(i)$ for any given $\{x^(1), y^(1), ..., x^(m), y^(m)\}$ with the $y^(i)$ a loss (error) function is defined :

$$\boldsymbol{L} = 0.5 \ \times (\hat{y} - y)^2, \tag{2.23}$$

where y and $\hat{y}$ are observed data and the linear function output, respectively. This loss function aims to reduce the difference between the output and the observed data. As loss function is defined for a single sample, we can defined the an accumulative function that calculate the cost function for m sample as :

$$\boldsymbol{J}(w, b) = \frac{1}{m} \sum_{i=1}^{m} 0.5 \times (\hat{y} - y)^2. \tag{2.24}$$

Therefore, the terminology that we will use is that loss function is applied to a single example, while cost function is the cost of parameters for all examples of data-set. The gradient descent method tries to find the w and b that minimise the equation (2.24) in an iterative approach. The above mentioned logistic regression equation (2.23) could lead to non-convex cost function. A non-convex function has multiple maximum/minimum (local), and the optimisation could be trapped in these local maximum/minimum and failing to converge to global maximum/minimum. Therefore; it is important to start the search from a known state (according to the prior information), in order to avoid the local maximum/minimum traps. It should be noted that a better-defined loss function could avoid this pitfall, for more information, please refer to Menard [112]. The idea behind the gradients descant is imitate the search from a known state and in every iteration and to take a step towards the global minimum. Thus, a derivative for the cost function in respect to parameters w and b are calculated and used to update these parameters.

$$w_{new} = w - \alpha \frac{d\boldsymbol{J}(w)}{dw}, b_{new} = b - \alpha \frac{d\boldsymbol{J}(b)}{db}, \tag{2.25}$$

where α is a learning-rate or step-size that refer to the amount that weights are updated. Figure (2.3) shows three different approach towards the global optimum (that is noted by +) with different values for α. The learning-rate is one of the most important hyperparameters to optimise as it solely can define the convergence or failure of the system [57, 124].

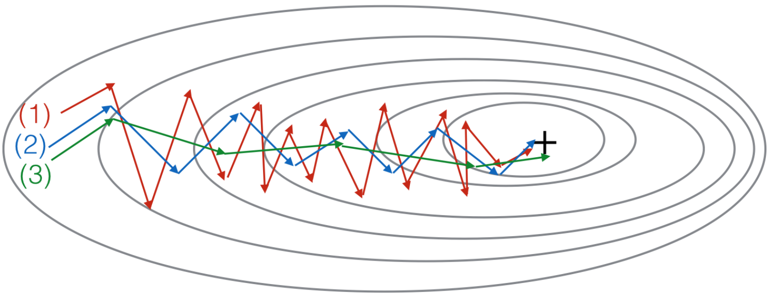

Figure 2.3: Gradient descent optimisation with three different learning rates, adopted from Ng, Katanforoosh, and Mourri [124]

The backpropagation procedure is utilising the chain rule to compute the derivative of the cost function for all parameters. The backpropagation process requires to have access to the previously calculated derivative as the values are used in optimisation for each iteration. As this process is I/O intensive to the point that writing down the calculated derivation will hinder the computation; thus standard method to compute the backpropagation is to keep the all derivative values in the memory while the weights are calculated as an on-air process. As on-air gradient calculation help to speed up the computing; introduce an obstacle with the memory restriction as a complicated model can easily overflow the memory.

2.5.2 Linear regression coupled with physics-based forward model

The linear regression optimisation techniques use weight-adjustment of its parameters in the forward propagation of the system. We can improve the forward model by including prior information into the system. We can formulate the prior information about the system as a physics-based forward model. By integrating a physics-based model into the linear regression; we can reduce the joint manifold space to make the system converge with fewer challenges and faster. Thus, it means to replace the $\hat{y}$ in equation (2.23) with a forward kernel that can simulate the response of the initialled values (input models). Tarantola and Valette [153] was one of the first who coupled a physics-based seismic forward kernel with linear regression to introduce the high-fidelity data fitting technique for seismic data known as full-waveform inversion (FWI). The new FWI improved the performance of the inversion by leaps and bounds as in contrast to RBI, FWI could include the entire waveform (or at least the first few cycles) of the signal. Thus, the resolution of the tomograms produced by FWI approached half of the dominant wavelength or better as more measured data could be integrated into inversion procedure. As a rule of thumb, by moving from RBI to FWI, the spatial resolution can improve by up to one order of magnitude for and for borehole applications, it can reach to one of borehole logging methods [177, 40, 133, 39, 12, 165, 167]. Since the pioneering work by Tarantola and Valette [153], a large number of FWI approaches for acoustic and elastic waves have been proposed using time-domain, frequency-domain, and hybrid methods [141, 26, 95, 167, 1].

2.5.3 Crosshole GPR FWI

The system of the information that we are trying to solve is based on the travel times and energy of the EM that passed through the target medium; where these parameters are transformed to velocity (equation 2.9) and attenuation (equation 2.10).

The ground breaking work of Tarantola and Valette [153] paved the way for probability methods to answer the inverse problem in geophysics. As it mentioned in section (2.5.2), FWI was initially developed for seismic data. Since finite-difference solutions of Maxwell's equations are computationally comparable to those of the viscoacoustic-wave equations in seismic, they were independently adopted to to crosshole GPR by Ernst et al. [47] and Kuroda, Takeuchi, and Kim [89], where both were using the 2D FDTD as their kernel. Ernst et al. [47, 46] developed a 2D FWI that utilise a gradient-based method to obtain high resolution ε_r and σ tomograms, and applied it to synthetic and experimental data. Later,Meles et al. [111] extended the approach of Ernst et al. [47] by incorporating the vector-based properties of the EM fields.

As it was mentioned in section (2.5.2), a FWI utilise a forward model and a inversion scheme. We have adopt the implementation of the FWI that was introduced by Meles et al. [111], while enhancing the forward model along the way that is explained in chapter (3). The Meles et al. [111] scheme uses a simultaneous update of the permittivity and conductivity models. In following we will discuss the general pre-processing steps, forward problem, source wavelet estimation/ extraction and inversion algorithm.

2.5.3.1 FWI Pre-Processing

(i) **Noise removal + Dewow**

(ii) **Starting models**: As it explained in section (2.3.1.2), prior information plays a crucial role in a successful inversion. As it explained in more details in section (2.3), FWI is an ill-posed problem that can have many possible valid answer. In crosshole GPR FWI, most of this information presented as ε_r and σ models. The method requires ε_r and σ starting models with adequate initial information. As it is discussed in section (2.5.1); a simple means square cost function is a non-convex operator. Thus, it is important to avoid local maximum/minimum by using the prior information as it is necessary to start the gradient search as close as possible to the global maximum/minimum. The synthetic data based on these starting models need to yield results that are within half a wavelength $\left(\frac{\lambda}{2}\right)$ of the measured data throughout the entire domain. If the synthetic response has more than half a wavelength misfit from the measured data, the synthetic pulse could fit an earlier or later measured pulse or even skip the whole pulse. This phenomenon is called "cycle skipping", where the inversion is trapped in a local minimum and is not able to converge to the global minima. Therefore, reasonably accurate starting models are a necessity for successful inversion [150, 32, 165, 49, 85, 167]. Moreover, detailed starting models reduce the computational effort required to converge the FWI. A more detailed discussion about the starting models importance and application for successful FWI strategies are presented in section (3.3.2).

(iii) **3D to 2D transformation**: As it previously mention in chapter (1.3), almost all of the applications of crosshole GPR FWI to experimental data were carried out with a computationally attractive 2D forward model. FWI using a complete 3D model with realistic model size requires significantly higher computational resources and large memory requirements. Wave propagation in 2D and 3D media have differences in its geometrical spreading, phase, and frequency scaling characteristics. It is necessary to take these differences into account before using a 2D forward model to invert measured data obtained in a 3D environment [46, 23, 28, 170]. The normally applied 2D assumptions are valid as long as there is no out-plane arrival in the data and in the far-field regime. Any numerical or analytical solution for the 2D wave equation inherently carries the assumption that any source is a line source, i.e., that it extends infinitely out-of-plane, causing a cylindrical wave front expanding from the centre line. In a 3D homogeneous medium a realistic point source generates a spherical wave front. The difference in the geometrical spreading of the wave in 2D and 3D media leads to a different amplitude decay with distance r and time. In the 3D medium, the energy is spread over the surface of a sphere. Hence the amplitude is scaled with $\frac{1}{r}$. Whereas in the 2D environment, the energy is distributed over the surface of a cylinder, so the amplitude is scaled with $\frac{1}{\sqrt{r}}$. Therefore, an identical pulse will decay faster in the 3D medium. These differences in geometrical spreading also create phase differences between the 2D and 3D Green's functions. In 2D, the Green's function is scaled with $\frac{1}{\sqrt{\omega}}$ compared to 3D, which results in a $\frac{\pi}{4}$ phase shift between the wave solutions for the 3D and 2D environments [174, 27, 114, 28]. The differences in geometrical spreading in the 2D and 3D environments and the effects on the associated amplitudes and phases should be accounted for prior to the inversion. The most common practice to address this issue is to apply a 3D to 2D transformation to the field data, referred to as a "geometrical spreading correction" [37, 27, 17, 121]. The crosshole configurations restrict a Tx and a Rx to a single plane, with the implicit assumption that there is negligible variation in the properties of the embedding medium in the direction normal to this plane [144]. Bleistein [18] calculated out-of-plane spreading factors using asymptotic theory and approximate asymptotic transformation for converting recorded seismic wave fields in a restricted 3D environment to two dimensions. [18] assumed that acoustic waves propagate in the far-field regime and that the medium properties of the host change smoothly. It is formulated in the frequency domain (where ω is the angular frequency) as:

$$\bar{\boldsymbol{G}}^{2D}(\omega) = \bar{\boldsymbol{G}}^{3D}(\omega)\ exp\left[\omega\left(\frac{i\pi}{4}\right)\right]\sqrt{\frac{2\pi L}{|\omega|}}, \tag{2.26}$$

where $\bar{G}$ is the Green's function of the 2D and 3D media. L denotes the integral of the velocity with respect to the arc-length of the ray trajectory that, in the homogeneous medium, is equal to the velocity v multiplied by the distance r between the Tx and a Rx $L = vr$. This asymptotic transformation of restricted 3D to 2D is often termed the *"Bleistein filter"* and is commonly applied in seismic data processing. Ernst et al. [46] adapted this transformation to electromagnetic wave propagation in the frequency domain as follows:

$$\hat{\boldsymbol{E}}^{2D}(x_s, x_r, \omega) = \hat{\boldsymbol{E}}^{obs}(x_s, x_r, \omega)\sqrt{\frac{2\pi T(x_s, x_r)}{-i\omega\varepsilon_r^{mean}\mu_0}}, \tag{2.27}$$

where $\hat{E}^{3D}$ are the observed 3D field data and $\hat{E}^{2D}$ the transformed 2D data for each Tx x_s and Rx x_r location, respectively. T is the travel time between the Tx and a Rx positions, $i^2 = -1$, ε_r^{mean} is the mean of the relative permittivity of the media, and μ_0 is the magnetic permeability of free space. Despite the benefits of the asymptotic 3D to 2D transformation in avoiding the requirement for computationally intensive 3D modelling, it still has some shortcomings. The transformation only uses the first-arrival times T and may perform poorly for multiple later arrivals. Auer et al. [6] study the performance of the asymptotic transformations for seismic crosshole data and show that substantial errors are observed in data from overlapping arrivals and curved paths. These errors translate into poor model reconstruction using FWI. Ernst et al. [46] claimed a satisfactory performance of the asymptotic 3D to 2D transformation for experimental data in a far-field regime, but did not provide a quantitative analysis of the accuracy. Van Vorst et al. [163] state a good performance of the asymptotic 3D to 2D transformation for GPR data for travel times, but observed high inaccuracy in the amplitude transformation that critically influenced the associated σ. In chapter (3), we have carried out series of studies to quantify the effects of the asymptotic 3D to 2D transformation on 2D GPR FWI, and specifically investigate the electrical conductivity results in the presences of high contrast zones.

2.5.3.2 Forward Problem

FWI utilise a forward model to simulate the system response and compare it with obtained data. The numerical modelling (section 2.2) is most common tool for simulating the earth response for source -wavelet estimation (section 2.5.3.3) and FWI scheme.In this thesis, we only utilised the FDTD forward model in both 2D and 3D domain. The differences and implication of these 2D and 3D FDTD are discussed it in chapters (3.2) and (4.2).

2.5.3.3 Source wavelet estimation and correction

Except for the synthetic cases (where the emitted wavelet is well-known), effective source wavelet is mostly unknown or has significant ambiguity. Clarifying this uncertainty through effective source-wavelet estimation is a crucial step in successful FWI. The effective source-wavelet extraction could match the theoretical wavelet (mostly provided by the manufacturer) to the measured waveform, including any small nuances that may be presented in the waveform. The extracted effective source-wavelet reflects the actual radiation pattern of the GPR finite-length antenna (FLA) and the influence of water- or air-filled boreholes as the borehole-filling [46, 110].

To estimate the effective source-wavelet, an initial source-wavelet needed to be calculated where the shape of the source-wavelet is determined without any amplitude information. Thus, all traces from a vertical ZOP (that only including horizontal travelling waves) are normalised and aligned and averaged to determine an average pulse. Possible error in the shape of the wavelet is eliminated by cross-correlating the ZOP traces. Simultaneously, the measurement noise is removed by taking the upper and lower neighbouring Tx into the account and averaging the traces.

The EM in equation (2.3) can as a Green function convolution by $\mathbf{E}^s = \mathbf{G}\mathbf{J}^s$, where $\mathbf{G}$ represents the Greens operator that describes the propagation of the EM through the medium. The explicit formulation of this Equations for a specific time and space point $(\mathbf{x}, t)$ is given by

$$\boldsymbol{E}^s(\boldsymbol{x}, t) = \int_V dV(\boldsymbol{x}') \int_0^{T_{max}} dt' \boldsymbol{G}(\boldsymbol{x}, t, \boldsymbol{x}', t') \mathbf{J}^s(\boldsymbol{x}', t'), \tag{2.28}$$

where $\mathbf{E}^s(\mathbf{x}, t)$ is the electrical field at point $(\mathbf{x}, t)$ generated by $\mathbf{J}^s(\mathbf{x}', t')$,and T_{max} is the maximum observation time. Here, the Greens tensor $\mathbf{G}(\mathbf{x}, t, \mathbf{x}', t')$ acts on the source term $\mathbf{J}^s(\mathbf{x}', t')$, which is defined as $\mathbf{J}^s = \delta(\mathbf{x} - \mathbf{x}_s) \cdot b \cdot \mathbf{S}(\omega)$, where $\mathbf{S}$ is the source wavelet, b identifies the antenna orientation and the delta function describes the position. The general form of the electrical field in the frequency domain is given by

$$\hat{\boldsymbol{E}}^s = \hat{\boldsymbol{G}}\hat{\boldsymbol{J}}^s, \tag{2.29}$$

where $\hat{}$ indicates the frequency domain. For far-field and high frequency approximation $\hat{\mathbf{G}}$ can be described by

$$\hat{\boldsymbol{G}}(\mathbf{x}, \omega) = \frac{j\omega}{|\boldsymbol{x}|}\boldsymbol{A}e^{-\alpha|\boldsymbol{x}|}e^{-j\frac{\omega}{v}|\boldsymbol{x}|}, \tag{2.30}$$

where $\mathbf{A}$ is the amplitude, α the attenuation, $|\mathbf{x}|$ the travel distance and v the velocity of the medium [162]. The term $j\omega$ is applied due to the solution in homogeneous 3D medium or to a halfspace [160].

The electric field is proportional to the time derivative of the current density source wavelet multiplied $j\omega$ in the frequency domain as equation (2.30). The shape of the initial source wavelet is extracted by dividing the average Fourier transformed selected electric field pulse by $j\omega$ in the frequency domain.

In the second part, we calculate the detailed wavelet, including the amplitude and phase characteristics. FDTD forward model (2D, or 3D) is deployed to simulate the earth response by using ε_r and σ starting models (section 2.5.3.1) and the initial source-wavelet for every Tx-Rx pairs. Any radar trace can be mathematically seen as the convolution of the source wavelet with the impulse response of the earth (Green's function) in the time-domain, or, as the multiplication of the source spectrum with the Fourier-transformed Green's function (as it is shown in equations 2.28 and 2.29). Thus, the effective source wavelet can be obtained by deconvolution of the measured data $\hat{\mathbf{E}}^s_{obs}$ with a proper Green's function $\hat{\mathbf{G}}$ using the traveltime RBI results [46, 147]. The proper Green function $\hat{\mathbf{G}}$ is calculated by spectral division of simulated electric fields in the frequency domain with the initial wavelet spectrum for each separate trace. The source wavelet is estimated by dividing the actual observed data with the Green function $\hat{\mathbf{G}}$, using all traces in a least-squares optimisation. The iterative convergence continues until the source wavelet converged. The source wavelet extraction can be repeated after several iterations of the FWI. It is important to note that inherently source wavelet extraction reduces the information embedded as it averaged the data. As it mentioned in the section (2.3.1.4), a system of the inversion needs to handle the system's inaccuracy. As our model system is well-defined by the FDTD; we need to include all the aspects of the simulation that we could not cover and the imperfection in the measured data via a term. We use the source wavelet as an inaccuracy term that can be calibrated to be realistic and closer to the measured data. The effective source wavelet is crucial to match the measured waveforms with synthetic data, including any small nuances that may be present.

Moreover, certain shortcomings imposed by the FDTD limitations, such as the effect of the GPR FLA, water or air-filled borehole (that is discussed in detail in chapter (4)) that is compensated by including the coupling effect by effective source wavelet. The effective source wavelet estimation accommodates the errors that were not accounted for in the model. It reduces the system restrictions and converges even with a tolerable degree of inaccuracy. The effective source wavelet estimation requires knowing the excitation source which is normally not known for experimental data [133]. As we improve the model's accuracy, less inaccuracy remains to be accounted for by source-wavelet extraction. This will reduce the system's inconsistency and eventually drive to more accurate outcomes. This issue is the main focus of the chapters (3) and (4). For more details about the importance of the source wavelet in FWI, see Ernst et al. [46] and Klotzsche et al. [81].

2.5.3.4 Inversion algorithm

As it mentioned in equation (2.23), loss function over all the samples (GPR traces) provides the cost function (equation 2.24). The FWI method that suggested by Tarantola [150] uses a conjugate gradient type method. The adaptation of this method for GPR traces means to reduce the cost function C_{FW} in an iterative approach that reflects the difference between the modelled $\mathbf{E}^s_{syn}$ and measured $\mathbf{E}^s_{obs}$ for traces of the all Tx-Rx pairs by finding the best fitting spatial distribution of ε_r and σ. The vector-based cost function (equation 2.31) is described as :

$$C_{FW}(\varepsilon,\sigma) = \frac{1}{2}\sum_s\sum_r\sum_\tau \left[\boldsymbol{E}^s_{syn}(\varepsilon,\sigma) - \boldsymbol{E}^s_{obs}\right]^T_{r,\tau} \delta(\mathbf{x}-\mathbf{x}_r, t-\tau) \left[\boldsymbol{E}^s_{syn}(\varepsilon,\sigma) - \boldsymbol{E}^s_{obs}\right]_{r,\tau}, \tag{2.31}$$

where $\mathbf{E}^s$ stands for the electric field of a particular source and contains the entire space-time domain, superscript T indicates the transposed operator, and s, r, and τ indicate sums over sources, receivers, and observation times, respectively. The gradient of $\mathbf{C}_{FW}$ is calculated to indicate the update direction of ε_r and σ models. Moreover, the step-length (a.k.a learning rate) indicates the magnitude of the model updates which are used together with the gradients to simultaneously update the ε_r and σ models.

To calculate the gradient ∇C, the forward propagated wave field $\mathbf{E}^s_{syn}$ is computed using the estimated source wavelet and the previously known models (such as starting models or results of the previous iteration).The generated fields are stored in the memory (as it necessary to efficiently calculate the derivative with sparse matrix operation) for each Tx-Rx pairs and for each time-steps. As we will use an incremental changes in the system, the Maxwell equations can be written for perturbed system that described the changes in the fields as function of the ε_r and σ as follows :

$$\boldsymbol{E}^s(\varepsilon+\delta\varepsilon,\sigma+\delta\sigma) - \boldsymbol{E}^s(\varepsilon,\sigma) = \hat{\boldsymbol{G}}(\partial_t\boldsymbol{E}^s\delta\varepsilon + \boldsymbol{E}^s\delta\sigma) = \begin{bmatrix} \boldsymbol{L}^s_\varepsilon & \boldsymbol{L}^s_\sigma \end{bmatrix}\begin{bmatrix} \delta\varepsilon \\ \delta\sigma \end{bmatrix}. \tag{2.32}$$

Here, the sensitivity operator $\mathbf{L}^s$ is defined for the individual contributions of the ε_r and σ perturbations with

$$\boldsymbol{L}^s_\varepsilon(\boldsymbol{x}') = \hat{\boldsymbol{G}}\delta(\boldsymbol{x} - \boldsymbol{x}')\partial_t \boldsymbol{E}^s_{syn}, \tag{2.33}$$

$$\boldsymbol{L}^s_\sigma(\boldsymbol{x}') = \hat{\boldsymbol{G}}\delta(\boldsymbol{x} - \boldsymbol{x}')\boldsymbol{E}^s_{syn}. \tag{2.34}$$

The first order approximation of the equation (2.31) estimates the gradient cost function as:

$$C_{FW}(\varepsilon + d\varepsilon, \sigma + d\sigma) = C_{FW}(\varepsilon, \sigma) + \nabla C^T_{FW} \begin{bmatrix} \delta\varepsilon \\ \delta\sigma \end{bmatrix} + O(\delta\varepsilon^2, \delta\sigma^2). \tag{2.35}$$

The total gradient ∇C_{FW} is calculated by summing up the contributions of the each Tx, Rx and observation time in equation (2.35). The residual wave field is calculated by subtracting the modelled $\mathbf{E}^s_{syn}$ and measured $\mathbf{E}^s_{obs}$ for each Tx. The summation of the misfit function over all Tx, $\mathbf{S}$ can be written as :

$$\begin{bmatrix} \nabla C_\varepsilon(\boldsymbol{x}') \\ \nabla C_\sigma(\boldsymbol{x}') \end{bmatrix} = \sum_s \begin{matrix} (\delta(\boldsymbol{x} - \boldsymbol{x}')\partial_t \boldsymbol{E}^s_{syn})^T \hat{\boldsymbol{G}}^T \boldsymbol{R}^s \\ (\delta(\boldsymbol{x} - \boldsymbol{x}')\boldsymbol{E}^s_{syn})^T \hat{\boldsymbol{G}}^T \boldsymbol{R}^s \end{matrix}, \tag{2.36}$$

with $\mathbf{R}^s$, which is a summation over all receiver and observation times, as the generalised residual wave field

$$\boldsymbol{R}^s = \sum_r \sum_\tau [\Delta \boldsymbol{E}^s]_{r,\tau}. \tag{2.37}$$

where $\hat{\mathbf{G}}^T\mathbf{R}^s$ can be interpreted as the back-propagated residual wave field in the same medium as $\mathbf{E}^s$. The spatial delta function $\delta(\mathbf{x} - \mathbf{x}')$ corresponds to the spatial components of the gradients and reduces the inner product to a zero-lag cross-correlation in time. $\mathbf{E}^s_{syn}$ is the electrical field for the actual model for a Tx at x^s that is stored in the memory for each Tx and time-steps. The residual wave field $\hat{\mathbf{G}}^T\mathbf{R}^s$ is back-propagated from all Rxs to the corresponding Txs through the model, simultaneously. Finally, the gradient at each point x is obtained by a zero-lag cross-correlation of the stored values of $\mathbf{E}^s_{syn}$ with the back-propagated residual wave field and by summing over all Txs and times-steps.

As it mentioned in previous sections, FWI requires step-length to identify the magnitude of the ε_r and σ models update that is necessary for each iteration. The updated ε_r and σ models can be formulated as:

$$\begin{bmatrix} \varepsilon_{upd} \end{bmatrix} = \begin{bmatrix} \varepsilon \end{bmatrix} - \zeta \cdot \begin{bmatrix} \nabla C_\varepsilon \end{bmatrix}, \tag{2.38}$$

$$\begin{bmatrix} \sigma_{upd} \end{bmatrix} = \begin{bmatrix} \sigma \end{bmatrix} - \zeta \cdot \begin{bmatrix} \nabla C_\sigma \end{bmatrix}. \tag{2.39}$$

The step length ζ determines how far we will move alongside the direction indicated by object function C, too small ζ leads to slow convergence while too big ζ causes overshooting of the FWI. For this purpose the appropriate perturbation factors κ_ε and κ_σ are introduced and the step lengths are obtained as:

$$\zeta_\varepsilon = \kappa_\varepsilon \frac{\sum_s \sum_r \sum_\tau \left[\boldsymbol{E}^s_{syn}(\varepsilon + \kappa_\varepsilon \nabla S_\varepsilon, \sigma) - \boldsymbol{E}^s_{syn}(\varepsilon, \sigma)\right]^T_{r,\tau} \delta(\mathbf{x} - \mathbf{x}_r, t - \tau) \left[\boldsymbol{E}^s_{syn}(\varepsilon, \sigma) - \boldsymbol{E}^s_{obs})\right]_{r,\tau}}{\sum_s \sum_r \sum_\tau \left[\boldsymbol{E}^s_{syn}((\varepsilon + \kappa_\varepsilon \nabla S_\varepsilon, \sigma) - \boldsymbol{E}^s_{syn}(\varepsilon, \sigma)\right]^T_{r,\tau} \delta(\mathbf{x} - \mathbf{x}_r, t - \tau) \left[\boldsymbol{E}^s_{syn}((\varepsilon + \kappa_\varepsilon \nabla S_\varepsilon, \sigma) - \boldsymbol{E}^s_{syn}(\varepsilon, \sigma)\right]_{r,\tau}}, \tag{2.40}$$

and

$$\zeta_\sigma = \kappa_\sigma \frac{\sum_s \sum_r \sum_\tau \left[\boldsymbol{E}^s_{syn}(\varepsilon, \sigma + \kappa_\sigma \nabla S_\sigma) - \boldsymbol{E}^s_{syn}(\varepsilon, \sigma)\right]^T_{r,\tau} \delta(\mathbf{x} - \mathbf{x}_r, t - \tau) \left[\boldsymbol{E}^s_{syn}(\varepsilon, \sigma) - \boldsymbol{E}^s_{obs})\right]_{r,\tau}}{\sum_s \sum_r \sum_\tau \left[\boldsymbol{E}^s_{syn}((\varepsilon, \sigma + \kappa_\sigma \nabla S_\sigma) - \boldsymbol{E}^s_{syn}(\varepsilon, \sigma)\right]^T_{r,\tau} \delta(\mathbf{x} - \mathbf{x}_r, t - \tau) \left[\boldsymbol{E}^s_{syn}(\varepsilon, \sigma + \kappa_\sigma \nabla S_\sigma) - \boldsymbol{E}^s_{syn}(\varepsilon, \sigma)\right]_{r,\tau}}. \tag{2.41}$$

The ε_r and σ models at each iteration are updated with the obtained gradient and step-length in an iterative process as long as the root mean square (RMS) between the modelled and measured data is below a certain threshold in subsequent iterations of the FWI. Details of the calculation of the misfit function, the gradient, and the step-length can be found in Meles et al. [111]. In this work, the stopping criteria' default value is 1.0% of the RMS in two consecutive iterations, except it is clearly expressed otherwise. Figure (2.4) shows, a summary scheme of the FWI workflow that uses the simultaneous update of the ε_r and σ and was explained in this chapter.

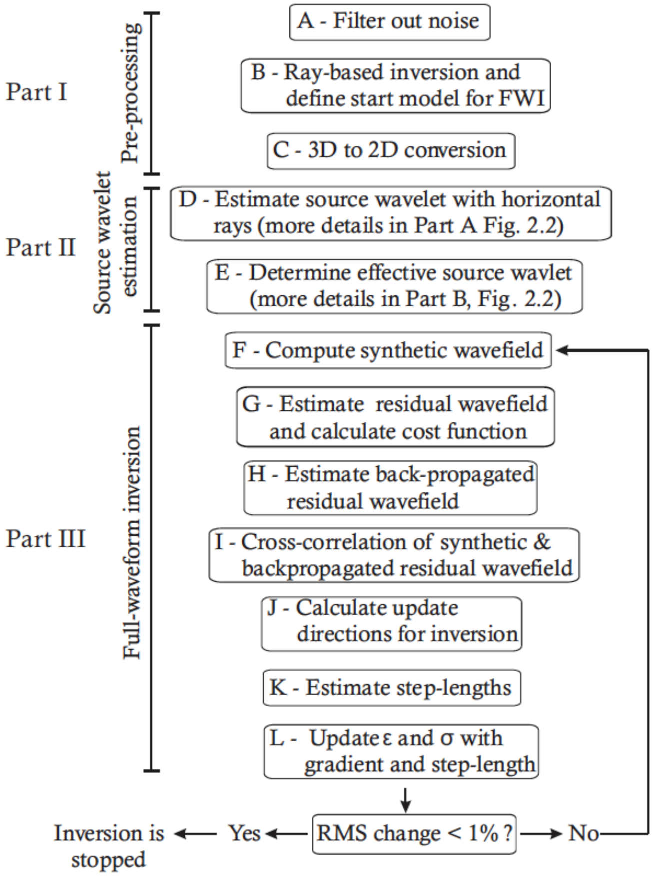

Figure 2.4: FWI workflow including the main parts: preprocessing, source wavelet estimation and inversion. The arrow indicates that these steps should be repeated until the misfit between the observed and synthetic data between sequenced iterative steps is below 1%. A more detailed version of this graph is provided by Klotzsche, Vereecken, and van der Kruk [79].

Chapter 3

2.5D crosshole GPR FWI with synthetic and measured data[1] [2]

In this chapter, we explore the necessity and advantages of the 3D FDTD as a forward model in a FWI. First, we study the performance of the common pre-processing method of 3D to 2D asymptotic transformation in multiple scenarios. Then, we introduced a 3D FDTD forward model and coupled it with existing FWI scheme that we called 2.5D FWI. The newly introduced 2.5D FWI is verified and compared with 2D FWI for a realistic synthetic data that showed improvements in inversion results. Besides, as new 2.5DFWI requires a significant increase in computational resources, multiple optimisation strategies are examined to reduce the computational intensity. Finally, the application of the new 2.5D FWI is verified for measured data.

3.1 Effects of the geometric spreading correction

As it mentioned in section (2.5.3.1), the effects of the asymptotic 3D to 2D transformation on 2D GPR and FWI is not completely clear to the GPR community. To quantify the influence of the asymptotic 3D to 2D transformation on the experimental data and hence the crosshole GPR FWI results, we first performed a numerical study to estimate possible errors introduced by this transformation. Previous studies Auer et al. [6] and Van Vorst et al. [163] indicated that the functionality of this transformation is sensitive to the degree of complexity of subsurface structures. Therefore, we designed a typical aquifer model including an unsaturated and saturated domain to study the effect of overlapping arrivals caused by the significant difference in velocity of the electromagnetic waves in unsaturated and saturated zones. Greenhalgh et al. [58] showed that the change of acoustic wave velocity influences the performance of the asymptotic transformation more than the change in the amplitude through the interface. Because of analogous relations between

[1]Mozaffari, A., Klotzsche, A., He, G., Warren, C., Giannopoulos, A., Vereecken, H., & van der Kruk, J. (2016). *Towards 3D full-waveform inversion of crosshole GPR data.* GPR Conference 2016, 5–8. `https://doi.org/10.1109/ICGPR.2016.7572687`

[2]Mozaffari, A., Klotzsche, A., Warren, C., He, G., Giannopoulos, A., Vereecken, & H., van der Kruk, J. (2020). *2.5D crosshole GPR full-waveform inversion with synthetic and measured data* . Geophysics, 85(4), H71–H82. `https://doi.org/10.1190/geo2019-0600.1`

visco-acoustic and electromagnetic wave propagation, the translation of this statement for electromagnetic waves is that the contrast of the ε_r values before and after the interface is more important than a change of the σ. Therefore, we limited our studies to models with variations in the ε_r and constant σ. In this study we have used 2D and 3D FDTD solver due to the necessity of each studies. As for 2D simulation,we have used the 2D FDTD that developed by Ernst et al. [48] and later has been advanced by Meles et al. [110] to incorporate the vector nature of the EM waves.We have used the gprMax as our 3D FDTD that is developed by Giannopoulos [52] as native GPR FDTD solver. It has been further developed in next years and we have used the version introduced by Warren, Giannopoulos, and Giannakis [169]. Both these codes, are automatically impose the CFL stability condition (look at section 2.2.2.1), by relating the temporal and spatial discretisation of the computational domain. Both codes also use the PML (look at section 2.2.2.2) boundaries to truncated the computational domain efficiently and prevent multiple reflection from boundaries. We apply equation (2.27) to transform the 3D data to 2D (which we term 'semi-2D'). The 2D model has the size 11 m x 6 m with boreholes 5 m apart located at 0.5 m and 5.5 m. The 3D model used the same dimensions as the 2D model and was extended by 1.2 m in the transverse direction with the same model parameters as the 2D plane. The numerical setup contains 11 Txs and 65 Rxs that are placed in the two opposite boreholes, from which one specific pair is located in a high contrast zone. Both models used a uniform grid with a 3 cm spatial discretisation in all dimensions. Figure 3.1, highlights a single Tx (no. 4) and Rx (no. 21) pair (red crosses) in four different media configurations. Models (a), (b) and (c) present water saturated scenarios, while model (d) illustrates the interaction between the unsaturated and saturated zone. Models (a) and (b) are chosen to be homogeneous with ε_r values of 12 and 18, respectively. Model (c) is homogeneous with a ε_r of 12 including a lateral structure with a thickness of 1 m and a ε_r of 18 located in the middle of the domain. This lateral layer acts as a low velocity waveguide that traps the emitted EM wave in this layer and causes multiple late arrival high amplitudes in the data [84]. Model (d) is extended from model (c) considering the unsaturated zone with a ε_r = 5. All four models have a homogeneous σ with a constant value of 9.5 $\frac{mS}{m}$. As source wavelet we used a predefined wavelet similar to the studies of [83] with a centre frequency of 92 MHz for all the models.

The left column of figure (3.1) shows the simplest possible ray-paths for each model, and the corresponding received waveforms are marked with the same number in the centre column. The shape of the semi-2D waveform is produced by equation 2.27. To compare the amplitudes of the true 2D and the semi-2D waveforms, we scaled the semi-2D waveform to the maximum amplitude of 2D A^{2D}_{max} in the homogeneous cases (a) and (b), and, we use the same scaling factor for the models (c) and (d). Note the amplitude of the 3D waveforms have also been scaled for visualisation purposes. It is clear that there is a good fit between the true 2D and semi-2D waveforms for the simple homogeneous cases (a) and (b). The ratio of $A^{2D}_{max}/\ A^{semi-2D}_{max}$ is almost identical for models (a) and (b), despite the fact that there is a 50% difference in ε_r values of the two models. This result confirms the previous studies of Ernst et al. [46] and

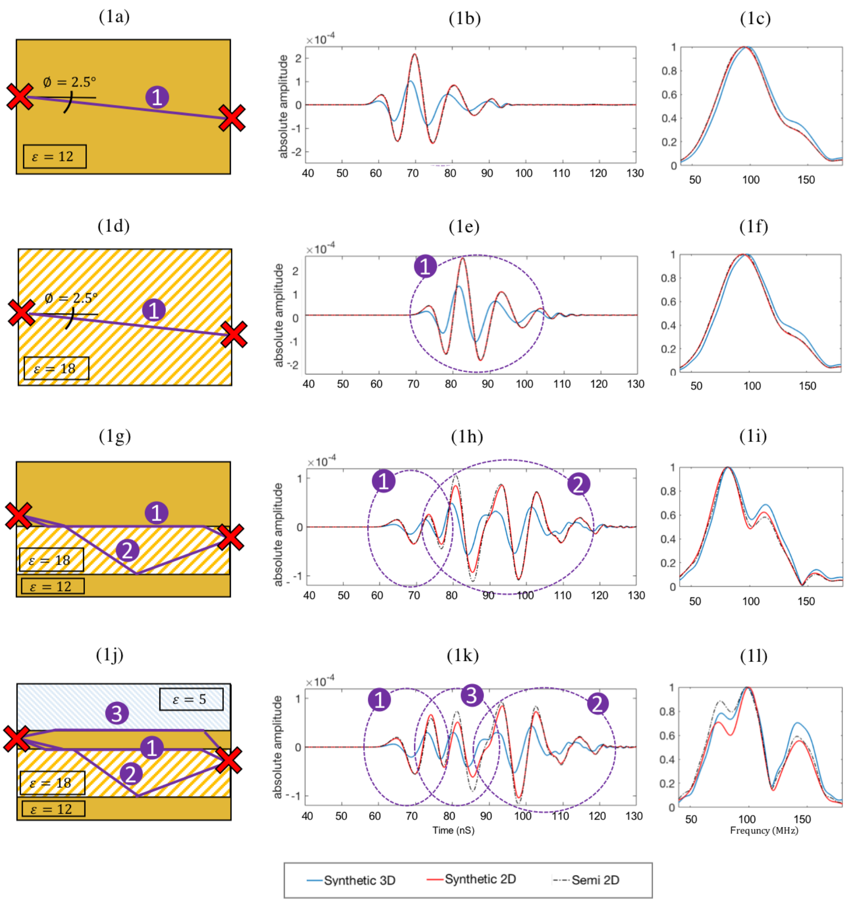

Figure 3.1: Synthetic subsurface crosshole GPR setup with: model a) homogeneous medium (ε_r = 12) (1a); model b) homogeneous medium (ε_r = 18) (1d); model c) homogeneous medium (ε_r = 12) with a waveguide structure (ε_r = 18) in the centre (1g); and model d) homogeneous medium (ε_r = 12) with a waveguide structure (ε_r = 18) in the centre with an unsaturated zone (ε_r = 5) on top (1j). The Tx-Rx pairs are marked by red crosses. The corresponding simulated 2D, calculated semi-2D, and 3D traces are in the centre column, where the major events are assigned to possible ray paths by number and dashed purple circles. The frequency spectra are presented in the right column. Note that the amplitude of the semi-2D and 3D traces are scaled by the ratio of $A_{max}^{2D}/\ A_{max}^{semi-2D}$.

Van Vorst et al. [163], where they claimed the good performance of the asymptotic 3D to 2D transformation for simple cases. In contrast, a significant misfit is observed between the 2D and semi-2D traces for the models (c) and (d) with a higher degree of complexity. In the model (c) multiple reflections in the waveguide structure cause later arrivals of the waves (6 ns to 12 ns). The energy distribution is also changed because the first arrival wave has less energy, and the trapped late arrival waves carry most of the energy. The misfit between the waveforms for 2D and semi-2D models (c) reaches up to 17% when waves travelling on path 1 and 2 interfere. In model (d) the misfit rises to 20% of the recorded amplitudes for waves travelling along the curved ray path that is labelled as 3 in figure (3.1). The maximum misfit occurs for the waves travelling along ray path 3 which overlaps with the wave travelling along ray path 2. This results in an amplitude error of 31%. For both model (c) and model (d), the error increases when the arrival of the different events overlap. It is important to note that the asymptotic 3D to 2D transformation does not provide the absolute semi-2D amplitude and therefore requires a scaling factor for homogeneous media. The misfit in the frequency spectra increases with increasing degree of complexity of the models. These results confirm the findings of Auer et al. [6] and Van Vorst et al. [163], who outlined that the 3D to 2D transformation performs poorly in complex structures, where overlapping events occur, and that the transformation has a substantial influence on the amplitude of the semi-2D waveform. This problem is caused by the nature of the asymptotic 3D to 2D transformation approach that relies on the transformation of the first arrival waves and the assumption that the highest amplitude of the data is associated with this first arrival event. Therefore, the performance of the transformation for overlapping or late arrival, high amplitude events is not reliable [85]. Moreover, the Bleistein [18] asymptotic transformation is based on the assumption of gradually varying medium properties. Therefore, sudden changes in medium properties, like the waveguide structure in model (c) and the transition from unsaturated to saturated zones in model (d), violate this assumption and consequently the asymptotic 3D to 2D transformation exhibits poor performance in these scenarios. It is important to point out that the asymptotic 3D to 2D transformation was initially developed to transform the acoustic waves in seismic analyses where far-field conditions almost always exist. The far-field assumption is potentially valid for the GPR crosshole setup when there is sufficient distance between the Tx and Rx boreholes, but it is not valid for closely spaced boreholes and on-ground GPR [147]. By comparing the 2D, semi-2D, and 3D frequency spectra, we observe a small downshift in the centre frequency for the semi-2D and 2D compared to the 3D. Cerveny and Psencik [28] observed this phenomenon in seismic data, and they claimed it occurs because of differences between point and line sources. This shift is an important consideration concerning spatial resolution since the high-frequency data are necessary for detailed imaging of structures.

Summarising, we observed poor performance of the asymptotic 3D to 2D transformation in complex structures, with amplitude mismatch errors of more than 30%. Additionally, applying the asymptotic transformation caused a loss of high-frequency content in the data, which subsequently affected the resolution of the

FWI tomogram. Furthermore, Watson [170] stated that even with the geometry of the crosshole setup limiting the Tx and Rx to a single plane, the out-of-plane scattering is not zero. Therefore, the 2D modeling approach may not be able to resolve the data thoroughly and can lead to artefacts in the reconstruction. These shortcomings of the 3D to 2D transformation make it necessary to move towards 3D modeling for more accurate FWI. Moreover, 3D modeling makes the detailed finite-length antenna and borehole modeling possible, which could increase the accuracy of the FWI for experimental data.

3.2 Novel 2.5D crosshole GPR FWI

To reduce problems caused by the 3D to 2D transformation, we coupled our existing 2D crosshole GPRFWI with a 3D FDTD forward modeling kernel. There are several reliable FDTD kernel available, and we have picked the gprMax 3D [169] as our kernel. The gprMax is a well-developed open-source software for simulating EM wave propagation with active community user. gprMax is supporting advance PML (look at section 2.2.2.2) that reduce the necessity of using a large model space and actively enforce the CFL stability condition (look at section 2.2.2.1). To create a 3D cube with 3D data, requires a 3D measurements. As we do not have the 3D measured data for such a setup, we used the 2D data as our input. The 2D setup is extended to a 3D model , by keeping the medium properties invariant in the direction perpendicular to the plane containing the boreholes [144], which are cylindrical objects, producing a 2.5D model [149].

3.3 Case study 1: Realistic synthetic model

3.3.1 Model description and generating synthetic data

Our first case study investigates the performance of our new 2.5D FWI approach and compare the results with the standard 2D FWI. As realistic input models for the 3D forward model, we used the final 2D crosshole GPR FWI results of Klotzsche et al. [83] that includes a high ε_r zone between 5 m to 6 m depth acting as a low-velocity waveguide (figure 3.2). As discussed above, such small-scale zones cause problems in the 3D to 2D transformation by introducing possible errors especially in the full-waveform σ results. We used these models in the 3D FDTD forward solver with a known effective source wavelet to produce 3D realistic synthetic GPR data. For the model dimensions we choose a similar setup as Klotzsche et al. [83] with 7.62 m $\times$ 11.67 m dimensions using a cell size of 3 cm for the forward modeling and 9 cm for the inversion. We built the 3D computational grid by extending the transverse direction to 0.9 m (inversion plane in the centre) and truncated the domain with 10 cells of PML at each boundary. A Hertzian dipole point source was used, and all materials were modelled as loss dielectrics, i.e. with no frequency dispersive properties. We transformed these 3D synthetic GPR data into 2D GPR data using the standard 3D to 2D transformation. The source wavelet for the 2D FWI is updated using the deconvolution approach as proposed by Klotzsche et al. [85]. Note that this step is necessary to also account for the different radiation patters of the 3D and 2D environment. 2D FWI using the transformed data is prone to exhibit poor performance in determining ε_r and σ with a subsurface model that contains thin layers and high contrasts in medium properties. Hence, two inversions are performed: (1) 2.5 FWI using the 3D data and the known input source wavelet, and (2) 2D FWI using the asymptotic 3D to 2D data transformation and an updated source wavelet.

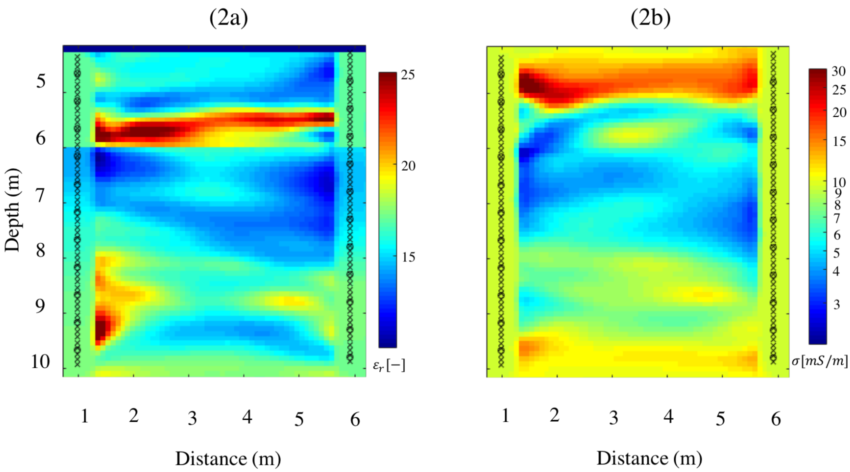

Figure 3.2: (a) ε_r and (b) σ starting models based on Klotzsche et al. [83] as the simulated reality for synthetic analysis. Note the logarithmic scale for the σ tomogram. Tx and Rx positions are indicated by circle and crosses, respectively

3.3.1.1 Starting models

Ray-based inversion can usually provide sufficient information as starting models, by using first-arrival times and first-cycle amplitudes of the data [67, 107]. However, Klotzsche et al. [83] show that ray-based inversion can fail to identify the major changes in the ε_r close to high contrast regions like the water table or small-scale high contrast layers. Hence, they propose updating the starting model for the ε_r by including a homogeneous zone near the water table and water table itself. Similar to [83], we used the starting models based on the ray-based inversion results with an updated zone between 5 – 6 m depth. For the σ starting model we used a homogeneous model similar to [83] that represents the mean of the first cycle amplitude inversion with a value of $\sigma = 9.5$ mS/m. We observed that the 2.5D FWI did not converge using the same starting models as for the 2D inversion of the synthetic data, while the 2D FWI could successfully reproduce the synthetic models as it presented in Mozaffari et al. [120]. We believe there were simultaneous effects from the 3D to 2D transformation that caused this issue:

(i) The 3D to 2D transformation shifts the data on average by 1.5 ns in time (look at figure 3.1). Using the 2D ray-based starting models produced data within half a wavelength for the 2D inversion. However, due to this shift, the 3D measured data are more than a half-wavelength away from the modelled data and therefore could not converge successfully due to cycle skipping.

(ii) Because the centre frequency of the transformed data using the 3D to 2D transformation is slightly lower than the original 3D data. This shift indicts that the high-frequency content in the transformed data is reduced and the transformed data have a lower spatial resolution compared to the original data. Therefore, it is easier to fit the modelled data to the transformed data with lower complexity compared to the original measured data with higher resolution. Thus, synthetic traces produced by the 2D forward model could fit the transformed data while synthetic traces from the 3D forward model could not match the original data due to the additional detail present in the 3D model.

Therefore, to guarantee an overlap within half a wavelength of the starting model based synthetic data and the measured data in the entire domain, we updated the ε_r starting model with a single homogeneous upper layer with a constant value of $\varepsilon_r = 18$ in the depth range 4 m to 6 m (before in average $\varepsilon_r = 16$). This update guaranteed an overlap of half a wavelength in the entire domain and allowed successful convergence for both 2D and 2.5D FWI.

3.3.2 Inversion strategies

2.5D FWI requires almost 300 times more computational CPU-hours than 2D FWI due to the computationally intensive 3D modeling. As we have seen the 2.5D FWI is also more sensitive to the ε_r starting model. Hence, there is a higher chance of the inversion becoming trapped in local minima instead of converging to the global minimum. Therefore, alongside the conventional FWI (direct method), we studied possible inversion strategies that could reduce the required computational effort and increase the chance of a successful convergence (cascade method). These cascade methods require the 2D inversion to be stopped in a particular stage, and the output is used as a priori information for a new start of the inversion with more detailed starting models. Since we knew the expected output from our synthetic study, we were able to compare the performance of the 2D FWI (with asymptotic 3D to 2D transformation applied) and 2.5D FWI schemes. We quantified the evaluation by calculating the relative model error for the ε_r and σ independently as follows:

$$\xi\left(m_{cal}\right)_{\sigma,\varepsilon} = 100 \times \left(\frac{m_{cal} - m_{true}}{m_{true}}\right)_{\sigma,\varepsilon}, \tag{3.1}$$

3.3.2.1 Direct 2.5D FWI

The ε_r and σ tomograms obtained from 2D and direct 2.5D FWI strategy for identical starting model are shown in figure (3.3). Comparing the results with the reference models (figure 3.2) shows that both 2D and 2.5D FWI were able to qualitatively resolve the main features of the ε_r and the σ tomograms. For the ε_r tomograms, both FWI reconstructed the three main layers successfully, while the results of the 2D FWI appear to be smoother than those from the 2.5D FWI. The σ tomograms are well-reconstructed for both approaches as both results shows main features of the synthetic input model. Despite the fact that the tomograms look similar from a qualitative perspective, a quantitative comparison shows differences in accuracy. The 2D FWI overestimates ε_r between 4.2 m - 5.7 m, where the lateral average error (LAE) reaches 26%. The obtained ε_r for the 2.5D FWI fits better the reference model with a maximum LAE of 7% at the interface between the upper high-velocity zone and the low-velocity waveguide. The average error (AE) in estimated ε_r in the whole domain is 2.5% for 2D FWI, while this value is 0.18% for 2.5D FWI. The *lae* for σ reached 32% and then dropped to -21% in the transition from high to low σ layers at depths of 5 m to 6 m. The LAE for the 2.5D FWI σ has maximum values of +6.5% and -21%. The AE for σ in the whole domain is 2.8% for 2D FWI, while this value is 0.5% for 2.5D FWI.

To evaluate the performance of the two FWI approaches with the reference model, we compare two cross-sections (A-A) and (B-B) in each model (indicated in figure 3.3). The ε_r values in A-A show a better fit to the reference values for the 2.5D FWI compared to the 2D FWI (figure 3.4). While both 2D and 2.5D FWI underestimate the ε_r at depths of 8 m to 10 m. The values of σ in A-A reveal a more accurate 2.5D FWI result. In the B-B cross-section, ε_r of the 2D FWI shows significant error in first 1.5 m depth and slightly misplaces the maximum peak. The ε_r values for the 2.5D FWI better fit the reference model all along cross-section B-B. The 2D FWI overestimates the σ in the upper layer and underestimates it continuously in the middle and lower areas, whereas the 2.5D FWI result was closer to the reference model. Moreover, the ε_r and σ model produced with the 2.5D FWI shows higher resolution in comparison to the results of the 2D FWI while it revealed smaller spatial variation for both ε_r and σ. This observation agrees with our hypothesis previously mentioned that the 2.5D FWI better reconstructs the 3D input models especially the electrical conductivity results by eliminating the effect of the asymptotic 3D to 2D data transformation. The normalized root mean square (RMS) error for the 2D FWI is reduced to 22% of the initial value, while this value is reduced to 12% for 2.5D FWI results. Both 2D and 2.5D FWI had termination criteria to stop the inversion when the change of the RMS error value in two consecutive iterations was less than 0.5%. The 2D FWI stopped after 21 iterations, while the 2.5D FWI met this criterion after

23 iterations. Note that a good data fit and no remaining gradient was present for all inversion results. Our new 2.5D FWI approach exhibits better performance over the 2D FWI in reconstructing the ε_r and σ models, regarding both correct positioning and accuracy of the assigned values. Furthermore, the ε_r and σ models of the 2.5D FWI have lower AE than the 2D FWI, and structures are slightly better resolved in the 2.5D FWI. Despite this superior performance, it is necessary to consider the higher computational demands of the 3D modeling used in our 2.5D FWI. Computational times for the simulations mentioned above are given in table (3.1).

Table 3.1: Results of the synthetic study using different inversion strategies and different starting models SM. Maximum lateral average error (LAE) and average error (AE) for the entire domain between the boreholes for ε_r and σ, Computation time (CT) for 20 consecutive iterations , reduction of the computational time in compare to 2.5D FWI, and RMS reduction normalised to the starting models

FWI strategy	Max ε_r LAE %	ε_r AE %	Max. σ LAE %	σ AE %	CT (min)	CT reduction %	RMS reduction %
2D	25	2.5	35	2.8	4.5	-	78
2.5D	6	0.18	19	0.5	1196.7	-	88
2.5D with 1st. itr. 2D FWI as SM	8	0.21	19	1.0	1136.4	5	84
2.5D with 4th. itr. 2D FWI as SM	19	1.55	28	1.6	957.7	20	82
2.5D with 7th. itr. 2D FWI as SM	23	1.9	33	2.2	778.9	35	81
2.5D with updated SM	8	0.16	11	0.45	664.8	44	88

3.3.2.2 Cascade 2.5D FWI

As it is shown in Mozaffari et al. [120], the results of the 2D FWI with a limited number of iterations can be used to improve the starting models for the 2.5D FWI, which allows a faster convergence and hence reduces the computational effort. Therefore, we applied 2D FWI to create ε_r starting models at iterations 1, 4 and 7, and then we used them for the 2.5D FWI. These ε_r models were used as starting models and were inverted with the 2.5D FWI (homogeneous σ starting model) until change of the misfit between two subsequent iterations is less than 0.5% (look at figure 3.5). All three models successfully show the key features and structures of both ε_r and σ. Furthermore, the comparison of the ε_r and σ results show that AE and LAE are increased by using the starting models that developed for a more extended time by the 2D FWI (look at table 3.1), indicating an increase in inaccuracies of the tomograms. All these results show that the percentage of the AE increases proportionally with increasing number of iterations of the 2D FWI used as starting models. Nevertheless, using this method could have a significant effect on the required computational effort. The computational time for the total inversion reduced by 5%, 20%, and 35% for the three models respectively, as shown in table (3.1). All computations were carried out

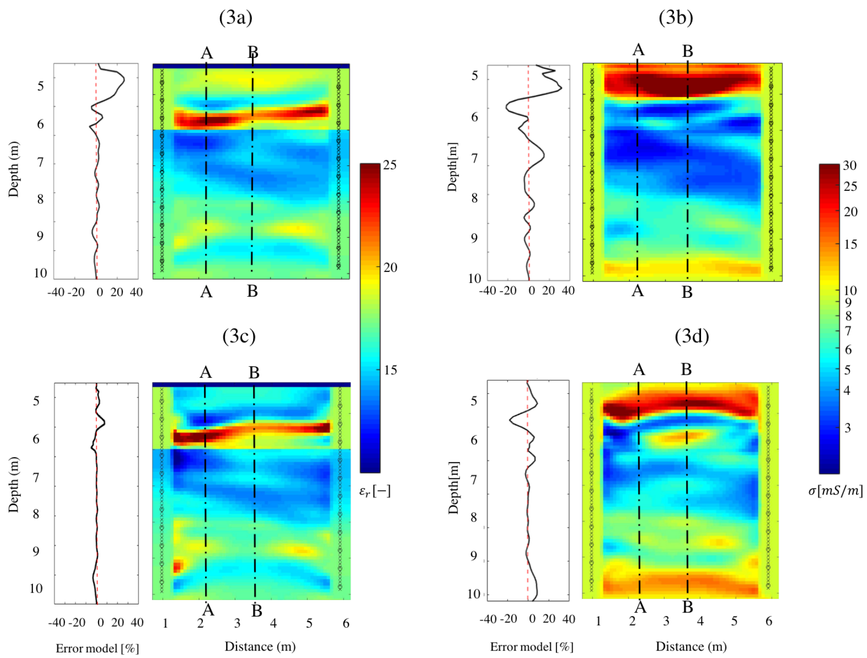

Figure 3.3: The (a),(c) are ε_r models and are (b),(d) σ models for 2D and 2.5D FWI respectively, while corresponding lateral average errors plotted on the left side of the tomograms. A-A and B-B show the positions of the cross-sections presented in figure (3.4). Note the logarithmic scale for σ tomograms. Tx and Rx positions are indicated by circle and crosses, respectively.

on JURECA cluster [88], which is part of the Jülich Supercomputing Centre (JSC). It is equipped with 1872 computing nodes with two Intel Xeon (E5-2680) with 2x12 cores at 2.5 GHz, simultaneous multi threading, and DDR4 (2133 MHz) memory with various capacities from 128 to 512 GB.

3.3.2.3 2.5D FWI with updated ε_r starting model

We propose a second strategy, where we combine the methods of Klotzsche et al. [83] and Mozaffari et al. [120]. Thereby, we update only the ε_r starting model with essential features revealed in the 2D FWI. Note that we checked for each starting model update if the half-wavelength criterion is still valid by performing forward modeling using these models and the 3D forward solver, and compared the input and the modelled data. The most significant missing attribute in the ε_r starting model

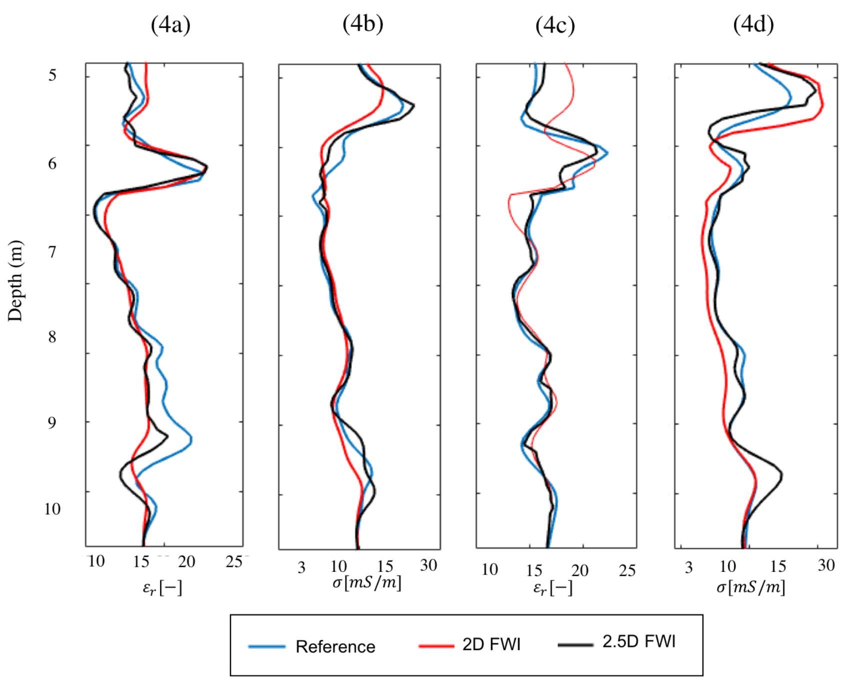

Figure 3.4: ε_r and σ values of the cross-sections A-A (a and b) and B-B (c and d) (position shown by dotted line in figure 3.3) for the reference values (blue), and models produced with 2D (red) and 2.5D FWI (black).

that we used so far is the high ε_r layer at a depth of 5.5 m to 6.0 m. This feature is revealed after a limited number of iterations in both the 2D and 2.5D FWI, while the σ does not show significant changes. Hence, our new updated ε_r starting model consists of two-horizontal layers, where the lower and upper layer have ε_r values of 22 and 18, respectively (figure 3.6a).

The 2.5D FWI with the updated ε_r starting model produced ε_r and σ tomograms with maximum LAE of 8% and 9%, respectively. These maximums occurred at the interface of the high ε_r layers. The AE for ε_r and σ errors were 0.16% and 0.45%, respectively, which is slightly better than the 2.5D FWI using the direct approach (compare to figure 3.6). Using this updated ε_r starting model, the 2.5D FWI required 44% less computational time to converge using the same number of CPUs. A summary of the 2D FWI and 2.5D FWI using different strategies with required computational demand is presented in Table 1. Furthermore, by comparing the convergence of the inversion and the RMS distributions over number of iterations for the different strategies (figure 3.7), it can be noticed that both strategies for the 2.5D FWI result in

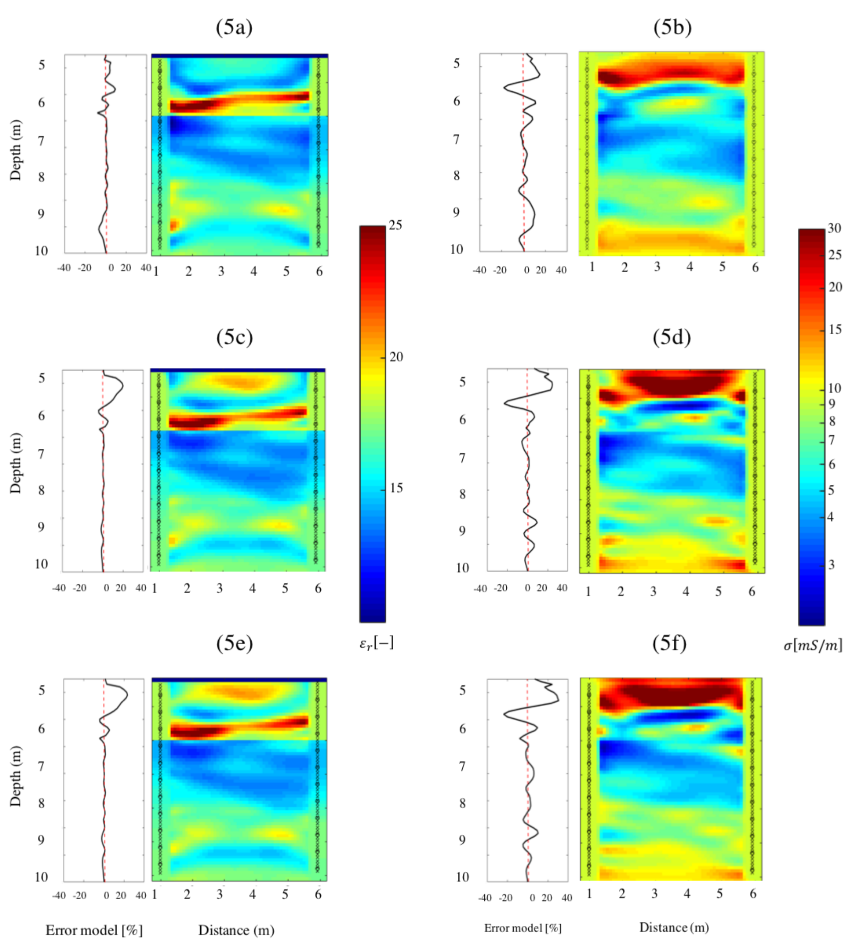

Figure 3.5: ε_r and σ and tomograms produced by 2.5D FWI for different starting models created from the 1st (a and b), 4th (c and d) and 7th (e and f) iteration of 2D FWI. Corresponding lateral average errors are plotted on the right side of each tomogram. Note the logarithmic scale for σ tomograms. Tx and Rx positions are indicated by circle and crosses, respectively.

the same final RMS value, while updating the ε_r starting model helped to reduce the RMS in earlier iterations of inversion. In summary, despite the fact of the reduction in computational effort by using the cascaded 2.5D FWI, the final 2.5D FWI results are

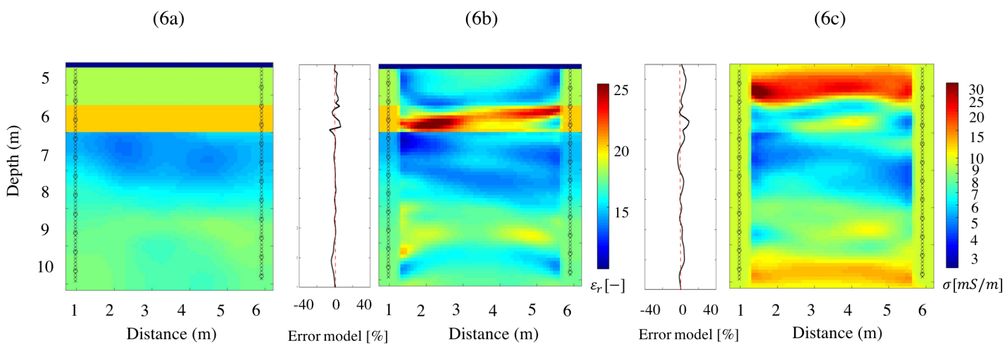

Figure 3.6: ε_r and σ Updated ε_r starting model (a), ε_r (b) and σ (c) resulting tomograms of the 2.5D FWI and the corresponding lateral average model errors on the left side. Note the logarithmic scale for σ tomogram. Tx and Rx positions are indicated by circle and crosses, respectively.

significantly affected by the 2D FWI drawbacks. This is because the AE is directly linked to the level of development of the starting model from the 2D FWI. Hence, choosing an adequate starting model based on the 2D FWI results is a compromise between the computational effort and accuracy of the results. Therefore, we do not suggest using early-stage results from the 2D FWI as an input for the 2.5D FWI. In contrast, the proposed method using a ε_r starting model for the 2.5D FWI with updates based on the results of the 2D FWI can significantly reduce the computational effort, while the accuracy of the models is not affected. We further apply this approach to invert experimental GPR data from the Widen test site.

3.4 Case study 2: Experimental data

3.4.1 Test site description

To validate the findings of the synthetic tests, we applied the 2.5D FWI approach to the experimental data of the Widen site (Switzerland). Several geophysical and hydrological studies have been performed at this site characterising the aquifer in detail [41, 43, 35]. The aquifer compromises a glaciofluvial deposit that includes a 3 m alluvial loam (silty sand) at the top, a 7 m thick gravel layer, and a low permeability clay aquitard below 10 m depths [33]. Multiple monitoring wells with 11.4 cm diameter are installed near to the river Thur. The GPR data were measured with a RAMAC Ground Vision system from Mala Geoscience with 250 MHz antennae. The data-set was acquired in neighbouring boreholes on the south-west plane, where

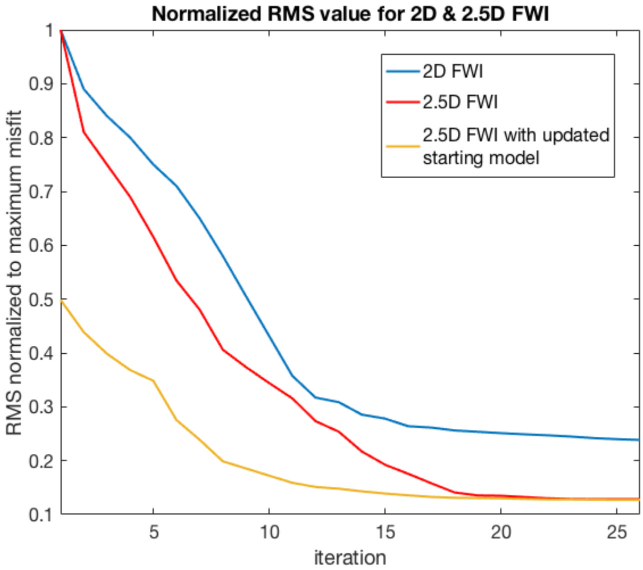

Figure 3.7: RMS misfit curves for 2D FWI (blue) and 2.5D FWI (red) using the same starting models, and, the 2.5D FWI using the updated ε_r starting model. RMS curves are normalised to the starting model value (0 iteration) used for the 2D and 2.5D FWI.

the water table was at approximately 4.2 m depth [43]. As shown in Klotzsche et al. [83] a high ε_r (high porosity) zone that could be linked to zones of preferential flow is located between 5 m - 6 m depth.

3.4.2 FWI results

We applied 2.5D FWI to the same dataset as Klotzsche et al. [83] and used the same data pre-processing steps, except that the 3D to 2D conversion is not necessary anymore for the 2.5D FWI. The effective source wavelet was updated using the deconvolution approach for the 3D GPR data and compared to the 2D FWI effective source wavelet (figure 3.8). Based on the finding of the synthetic studies, we chose as a starting model for the ε_r the updated model based on the 2D features (figure 3.6a). A homogeneous σ starting model of 9.5 mS/m is used. The inversion converged and the 16th iteration was estimated as an optimal solution (figure 3.9), where the change of the RMS error compared to the previous iteration was less than 0.5% and no remaining gradient was present. Unfortunately, we do not have any logging data from the same boreholes. Therefore, we tried to validate the experimental based on previous studies. The ε_r and σ tomograms produced by 2.5D FWI are in a good

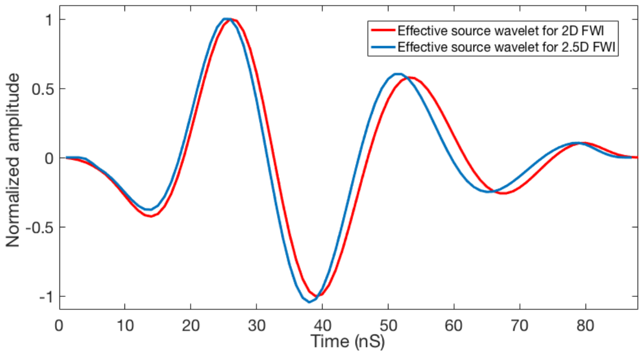

Figure 3.8: Comparison of the 2D effective source wavelet based on Klotzsche et al. [83] in red and the 2.5D effective source wavelet in blue using the deconvolution approach. Note both wavelets are normalised to their maximum amplitude.

agreement with the 2D FWI results from Klotzsche et al. [83]. The slightly upward dipping high ε_r structure between 5.3 m to 6.1 m was identified as low-velocity. We also observed the same structure using our new 2.5D FWI approach. The average σ values for 2.5D FWI results are around 1.4% lower than the average values from the 2D FWI. These differences in σ values are higher in zones with higher ε_r between 5.2 m – 6 m and 9.2 m – 10 m. The RMS misfit error between the measured and 2.5D modelled data was reduced to 50% from the starting model values. In comparison, the 2D RMS errors for the same starting model only reduced by 48%. The lower average σ in the entire domain for 2.5D FWI is the main reason for the 2% improvement in the RMS misfit compared to the 2D FWI.

3.5 Conclusion

In this chapter, we have investigated the performance of the asymptotic 3D to 2D transformation. Despite the usefulness of the asymptotic data transformation to avoid computationally expensive 3D modeling, it assumes that the highest wave amplitudes are associated with the first arrival. We demonstrated that this asymptotic transformation function only works accurately in such simple subsurface cases, while it fails with complex structures such as high contrast layers that produce overlapping arrivals from several different features. Moreover, the amplitudes assigned to waves after the 3D to 2D transformation are only valid for simple homogeneous media and are therefore not suitable for non-uniform media. We also observed that applying the 3D to 2D transformation to measured data lowers the resolution of the data by reducing the high-frequency content. Therefore, to overcome the restrictions of the 3D to 2D conversion assumptions and to minimise the associated errors in the crosshole

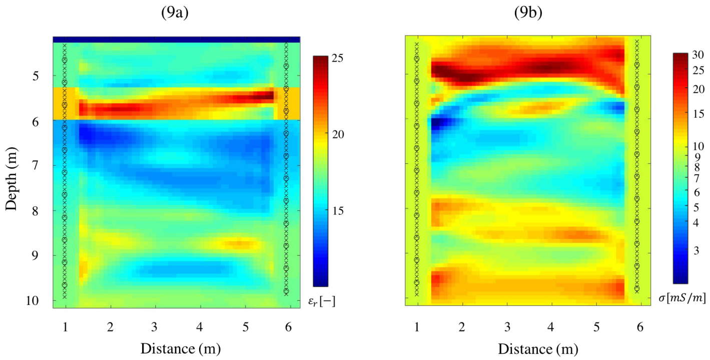

Figure 3.9: 2.5D FWI tomograms for ε_r (a) and σ (b) for the experimental data of the Widen test site using the updated starting model (look at figure 3.6a) and effective source wavelet (look at figure 3.8, blue). Note the logarithmic scale for σ tomogram. Tx and Rx locations are indicated by circles and crosses, respectively.

GPR FWI results, we extended the existing 2D FWI with a 3D forward model. Our new 2.5D FWI uses gprMax as a complete 3D FDTD modeling engine which makes the 3D to 2D transformation unnecessary. We compared the performance of 2D FWI (with 3D to 2D transformation) and the 2.5D FWI for realistic synthetic data. The results for 2.5D FWI showed higher accuracy in estimated ε_r and σ and provided lower AE in tomograms. Thereby, we observed that the ε_r starting model of the 2.5D FWI needed some modifications in comparison to the 2D starting model to still fit the requirements to provide modelled data within half of the wavelength of the measured data. The time shifts caused by the asymptotic 3D to 2D transformation placed the transformed 2D data less than the half-wavelength distance from modelled data while the original 3D data were too far from modelled data to converge. Moreover, a slight decrease in the dominant frequency of the transformed data was observed, which caused a loss of high-frequency content. Despite the lower AE and higher resolution of the 2.5D FWI, the trade-off is a significant increase in computational resources. Therefore, we examined multiple strategies to improve the starting model by using results from the less computationally intensive 2D FWI directly. We have studied the possibility of using the 2D FWI intermediate results as input for 2.5D FWI to reduce the required computational effort. But we found out that this method will introduce inaccuracies and we have abandoned this idea. Alternatively, we found that by updating the starting model based on the main features obtained by 2D FWI, we can reduce the computational costs by more than 40% while maintaining accuracy and resolution. Finally, we applied the novel 2.5D FWI to previously studied experimental GPR data from the Widen test site (Switzerland) to investigate changes achieved in the final tomograms. The results showed agreement with previous 2D works, and all the expected structures were identified. As expected, the main improvement was that the σ tomogram shows higher values in zones of higher ε_r and high contrast layers. For both synthetic and experimental data, we have seen that using the ray-based results as starting models for the 2.5D FWI causes the inversion to be trapped in a local minimum and an update of the permittivity model was required to successfully perform the inversion. Overall, we demonstrated that our new 2.5D FWI with 3D forward modeling is a valuable tool for an improved and more quantitative modeling of the subsurface. In particular, the use of a 3D forward model allows us to reduce assumptions that mainly affect the quantitative σ results, and, furthermore allows us to simulate important details including borehole structure, borehole filling, and finite length antennas.

Chapter 4

3D GPR antenna model and enhanced FWI with borehole fluid integration[1]

In this chapter, we explore possibilities of a 3D FDTD for more accurate modleing of the GPR system and subsurface. First, we developed a FLA and borehole-fluid models and validated their performance versus theoretical antenna models. Then, we used these newly developed models to simulate the effect of the borehole-fluids and FLA on travel-time and shape of the emitted wavelet for GPR data. Then, these models are combined to build a 3D crosshole GPR model that includes FLA and borehole-fluids model that each Tx-Rx is simulated independently. Lastly, the borehole-fluid model is integrated into 2.5D FWI (that is introduced in the chapter (3)), and performance of it is verified for synthetic data and compared to vanilla 2.5D and 2D FWI.

4.1 Introduction

In last years, application of the GPR has been widened in geophysics and civil engineering due to advances in GPR devices design, size and functions. In parallel, massive improvement in modelling tools and availability of computational resources helped to increase the application of the GPR as a go-to tool for researcher and engineers. An accurate GPR forward model is a handy tool for better understanding the subsurface and data acquired from measurements. GPR reliability and performance are highly depending on the user skills, and an accurate forward model helps user to compare the measured data with a reliable simulated data and verify the plausibility of the data; which is very valuable especially for new GPR users. Moreover, it helps the more skilled GPR users to investigate the test site prior to the measurement campaign with s simple simulation to arrange the most cost-effective measurement setup. A GPR setup, includes GPR system, subsurface and any potential targets. All these components need to be included and modelled as

[1]Mozaffari, A., Klotzsche, Zhou, Z., A., Vereecken, H., & van der Kruk, J. (2021). *3D electromagnetic modelling explains the apparent velocity increase in crosshole GPR data - borehole fluid effect correction method enables the incorporation of high-angle travel time data* . IEEE Transactions on Geoscience and Remote Sensing, 1–10. `https://doi.org/10.1109/TGRS.2021.3107451`.

accurately as possible to have an accurate forward model, as the real measured data is going to be compared with the simulation data. Even though the more realistic description of the subsurface is finding their way to the GPR forward model, most of these tools are limited to theoretical sources such as an infinitesimal dipole. Despite the usefulness of this type of source for far-field regimes and low computational overhead; they are far from a realistic representation of the real antenna models. To accurately model the phase and amplitude information of the GPR system in near-filed, which is most of the GPR applications; it is necessary to incorporate realistic antenna models [168].

In early 2000s series of attempt started to integrate more realistic antennas design into 2D's and 3D's forward models that entirely restricted to costume-made surface GPR; where all were 3D antenna used FDTD method, and loaded with discrete resistors with an infinitesimal dipole source model [68, 116, 96, 91, 159, 101]. In more recent studies, detailed 3D model of commercial surface GPR system is characterised or developed and verified which some of them are publicly available, including: 3D FDTD model of Geophysical Survey Systems, Inc. (GSSI) 1.5-GHz antenna by Klysz et al. [87], MALA 100-MHz antenna by Streich and van der Kruk [148], GSSI 900-MHZ by Lambot et al. [90], GSSI 1.5 GHz and MALA 1.2 GHz by Warren and Giannopoulos [168] ,GSSI 1.5 GHz by Giannakis, Giannopoulos, and Warren [50]. Except from work by Stadler and Igel [145] that is a generic 400 MHz FDTD surface GPR model for borehole sounding; all above mentioned models are developed solely for surface GPR purposes. The main reason for it, is that surface GPR is more widely common and has varied engineering application that motivates researcher and industry to develop more detailed models. Moreover, the setup of the crosshole GPR is normally bigger than more common surface GPR, which means required a bigger modelling domain. In addition to the domain size, the dimension of the borehole antenna and borehole-filling are much smaller than the medium, and the target in crosshole GPR that requires very fine discretisation to be accurately modelled. All these challenges made the infinitesimal dipole source and no borehole integration a common standard for crosshole GPR modelling.

As it was discussed in the section (2.3.1.3), inversion requires a forward operator that encapsulates the understanding of the physical system. One of our fundamental assumptions was that the system *modellisation uncertainty is negligible*; any simplification or shortcoming in the modelling of the system increases the uncertainty of the inversion itself. Therefore, naturally, any attempt to improve in the forward model directly increases the performance of the inversion itself. As it mentioned in chapter (2.5), source wavelet correction is a buffer that accounts for all of the uncertainty of the system that is also take care of the FWI forward modelling shortcomings. By improving the antenna representation and borehole-fluid in the FDTD model, the source wavelet correction contribution to inversion can be reduced and be limited only to the unknown and unaccounted parameters. In this chapter, we introduced a simple 3D model of crosshole GPR system and a 3D borehole-filling that is used to study the effect of the realistic antenna model and borehole-fluid in finely meshed 3D FDTD. In later part of this chapter, we integrated the 3D borehole-filling model into the 2.5D FWI that was introduced in chapter (3) and we show that it can improve the performance of the FWI as it reduce the uncertainty in the forward modelling.

4.2 Finite-length antenna and borehole fluid models

As it briefly mentioned in section (4.1); crosshole GPR is almost entirely rely on infinitesimal dipole source to represent the Tx and Rx in both RBI and FWI. This is because, the infinitesimal dipole source is very easy to implement, do not require fine discretisation of the modelling domain that itself demands high computational intensity. Despite, usefulness of point sources in straight forward modelling, the point source radiation pattern is different from real GPR antennas [148]. This issue is even more prononuced in the near-field regime, where there is no significant distance between the Tx and Rx; which is the case for crosshole setup with small offset. In addition, a near-field regime causes more complex coupling between the medium and the EM wave emitted from Tx, that is the case in the borehole-filling that is usually located in less than few centimetre from the feeding point GPR. These differences in reality and the simulated EM propagation cause the differences in travel time and attenuation of the emitted signals that in the end translate in inaccurate ε_r , and σ. In contrast to simplistic infinitesimal dipole source, a FLA could represent the interaction of the antenna and the surrounding medium more realistic, as the antenna has dimension and material that can be assigned based on the material analysis. A broadband crosshole GPR system is made of the resistively loaded antenna, which could be fabricated by resistive material or it can be loaded by the end of the antenna legs. The antenna could be fabricated from highly conductive material which called perfect electric conductor (PEC) antenna or the resistive materials. This resistive loading materials gradually diminishes the EM wave as it is travelling across the antenna rod and therefore, decreases the reflections that cause at the end of the antenna. The resistive loaded antennas (RLA) are broadband, and a signal can be transmitted with less distortion and ringing in compare to simple PEC [76, 91, 157]. As RLA is more favourable due to broadband, less distortion and smaller physical volume; almost all crosshole GPR antenna is made resistively-loaded. As we are using a FLA with a RLA design, from now; we use the term resistive loaded finite-length antennas (RLFLA) to emphasise the design and type of the antenna.

As it was previously used in chapter (3.2); we have utilised the gprMax 3D introduced by Warren, Giannopoulos, and Giannakis [169] as our FDTD kernel. The gprMAX have been used to model detailed FLA GPR systems [168, 50, 145]. In order to include the borehole-filling and the detailed RLFLA, we developed a complimentary script for gprMax that compile the subsurface model, borehole-filling and antenna components with very-fine meshed medium and generating an automatic meshed material grid based on any given Tx and Rx positions. This code is available publicly on GitHub. The generated 3D cube including the materials and model is used by gprMax to simulate the EM wave propagation.

In order to include the antenna, borehole-filling model into the FDTD, we used much finer discretisation as borehole diameter is usually around few centimetre. This issue impose a heavy computational cost to simulation as dimensions of the simulation domain could vary from meters to tens of meters that easily make crosshole GPR detailed modeling impossible for a user without access to high performance computing (HPC) resources. All computations in this study were carried out on JURECA cluster [88], which is part of the Jülich Supercomputing Centre (JSC). It is equipped with 1872 computing nodes with two Intel Xeon (E5-2680) central processing unit (CPU) with 2x12 cores, 2.5 GHz with simultaneous multi threading and DDR4 (2133 MHz) memory with various capacity from 128 to 512 GiB memory.

4.2.1 3D Crosshole GPR antenna model

We build a 3D model of RLFLA from Sensors and Software crosshole 200 MHz PulseEKKO based on the information that the manufacturer supplied us. The antennas have a 2 cm radius and a total length of 121 cm. We used a ricker waveform excitation with specified centre frequency of 92 MHz. This centre frequency was chosen to be similar to previously performed EM modeling considering the PulseEKKO antennea and water filled boreholes [84, 59]. At each side of the 1-cm vacuum feeding point that is present at 26 cm from the bottom of the antenna, resistively loaded arms with a length of 24 cm are present. A PEC material is used as transmission wire that contained 10 resistor segments with constant σ of 0.1 mS/m for each of the two antenna arms. As indicated by the manufacturer (personal communication), this PEC is surrounded by an insulation having $\varepsilon_r = 4$ and $\sigma = 10^{-7}$ mS/m as reported by Lampe and Holliger [91].

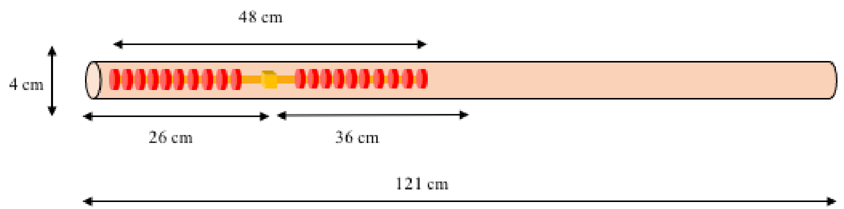

Figure 4.1: 3D borehole antenna design parameter based on Sensors and Software borehole 200 MHz PulseEKKO

4.2.2 Antenna Validation

To verify simple RLFLA antenna design, we have verified the performance of it versus antenna theories and showed that it could deliver reliable synthetic data. Even though, the dimension and design of the borehole antenna significantly reduce the staircase effect of the sparse discretisation in FDTD forward model; we have simulated several finer discretisations to ensure that the results with 0.01 m mesh are stable.

Resonant frequency for antenna

We validate the performance of the antenna model by cross correlating the injection voltage frequency and the length of antenna arms. The maximum amplitude will be transmitted, when the wavelength of the emitted signal match the half length of the antenna. We used the PEC antenna, where the effective length of antenna is equal to the length of the one arm. The antenna model has two arms, each 0.24 m and the angle between them is 180 degrees. Wavelength λ of the emitted signal is calculated by following formula:

$$\lambda = \frac{C}{f\sqrt{\varepsilon_r}}, \tag{4.1}$$

where c is the velocity of the EM waves in the vacuum that we use the value of 0.3 (m/ns), f is the centre frequency of the antenna voltage. For example, the PEC antenna with f of 362.5 MHz yields a wavelength equal to the length of the one antenna arm (0.24 m). It worth to note, the equation (4.1) in it simple form is only valid for PEC as calculating the effective antenna arm for the FLA is very complicated. Therefore, we assume it for equivalent PEC antenna as we are only interested in the governing physics. Several different frequencies are used, and the maximum of primary amplitudes are presented in figure (4.2) and centre frequency is indicated with purple line. Our antenna model is validated by this numerical simulation as maximum amplitude difference was recorded for the antenna with f equal to 365.2 MHz. where the wavelet has most symmetrical shape and its equal to antenna resonance frequency.

Coupling with surrounding medium

In order to verify the coupling of the RLFLA with surrounding medium, we have simulated the Tx and Rx in a homogeneous medium with a realistic range of $\varepsilon_r = 6-16$. As mentioned in equation (4.1), by increasing the value of ε_r, and a fixed centre frequency for input signal; we expect to see decrease in a the effective centre frequency and the wavelength of the received signal as we have observed (look at figure 4.3). This phenomena is due to the fact that antennas being electrically longer. This is an important matter for us, as we want to include the borehole-fluid in to the FDTD, and we could ensure that these effect is fully captured in the simulation.

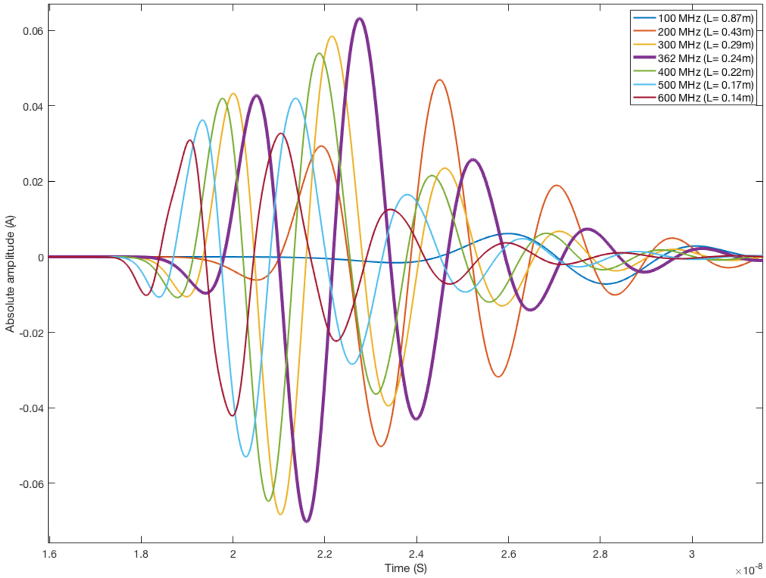

Figure 4.2: Absolute amplitudes for simple PEC antenna with different centre frequencies, an antenna with 362 MHz centre frequency (purple line) that produces the wave-length matches the half wave-length (24 cm) has the highest amplitude difference, and most symmetrical waveform that verifies the antenna reacts according to antenna theory.

Verification with multiple discretisation

We studied the effect of the discretisation size on the performance of the models for 0.7 – 1.0 cm mesh size, and as it showed in figure (4.4) the normalised waveform to the the square of the mesh and the maximum amplitude are similar regardless of the mesh size. Thus, the geometry of the crosshole setup, eliminate the possible staircase effect of the coarse meshing because boreholes and the Tx and Rx antennas are in the same plane and located in parallel to each other. Note that finer discretisation would have increased significantly the computational cost and could not have been performed [170].

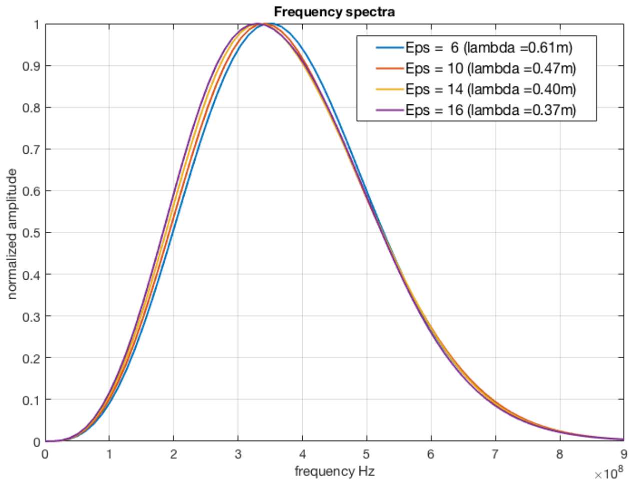

Figure 4.3: On-sided frequency spectrum (and associated wavelength) for the received signal for an identical input wavelet with a fixed centre frequency that travelled through the different mediums with ε_r ranging from 6 to 16

4.3 Borehole fluid effect (on travel-time and frequency spectrum)

Our RLFLA model successfully coupled with the surrounding medium (look at sections 4.2.2). We use this ability to investigate the effect of the borehole fluid on travel-time and wave propagation. Therefore, we placed the RLFLA in three different settings of the embedded in soil ($\varepsilon_r = 12$), in the 4 cm diameter air-filled and water-filled borehole in the soil ($\varepsilon_r = 12$) (figure 4.5). The air-filled borehole causes a more symmetrical wave frontier leaving the voltage gap, while the wave frontier has a convex shape due to higher velocity of the EM waves in the air in comparison to the surrounding soil. The presence of the water-filled borehole stretches the wave frontier, while the wave frontier in the borehole itself became concave because of the lower velocity of the EM waves in the water in comparison to the neighbouring medium. The borehole-fluid effect is observed in both RLFLA and infinitesimal dipole source.

The signal emitted from the RLFLA located in air-filled borehole arrived first, then from embedded RLFLA and last signal from the RLFLA placed in water-filled borehole arrived (figure 4.6). Comparing the absolute amplitudes of the models show that the presence of the boreholes causes deprivation of the transferred energy level. As the water has the highest conductivity in compare to other boreholes; it is experiencing the highest reduction of the recorded amplitudes. Moreover, the presence of the borehole structure acts as a wave-guide that traps the energy, and it prevents

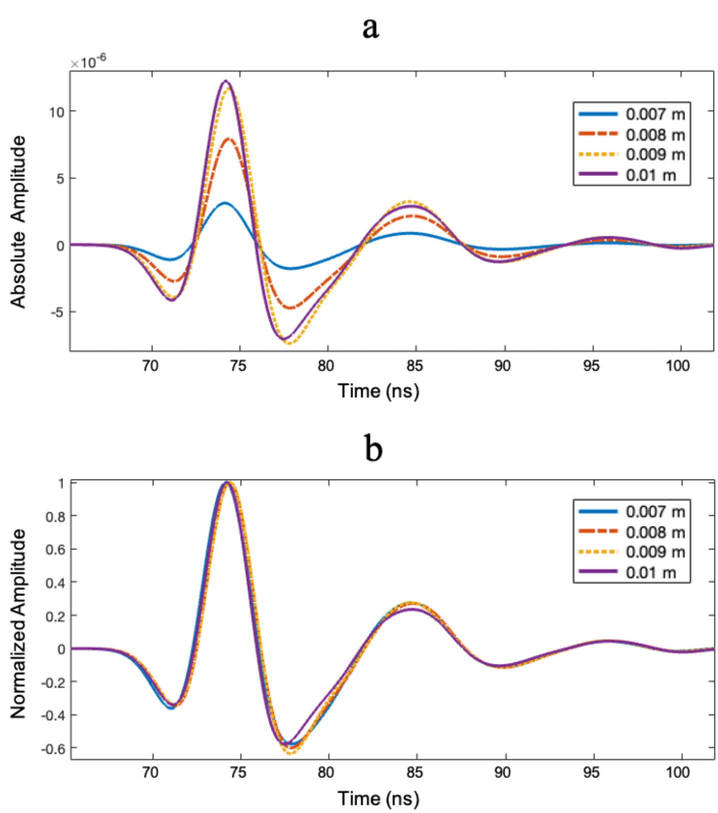

Figure 4.4: a) An absolute GPR traces for a pair of Tx, Rx with a RLFLA is simulated with mesh size of 9 - 1.0 mm and b) same traces normalised to the maximum amplitudes and squared mesh size

the maximum transmission of the energy o the Rx antenna.

Moreover, the effective centre frequency of the received signals reacts as expected in agreement with equation (4.1). The water-filled borehole has the lowest effective centre frequency, while the highest effective centre frequency belongs to the air-filled borehole. These simulations are in agreement with a previous study carried out by Tronicke and Holliger [154].

4.4 FLA effect in wavelet angular-dependency

4.4.1 Synthetic study

An effect of the RLFLA is that the radiation pattern of the emitting wave is different than the simplistic infinitesimal dipole source. An infinitesimal dipole source emits a symmetrical wavefront in a homogeneous medium; in contrast, a RLFLA propagates an unsymmetrical EM. Therefore, attenuation of the EM waves will have non-uniform effect on attenuation [147]. Therefore, the shape of the wavelet is independent of ray-path angle for infinitesimal dipole source while it is dependent on the ray-path angle for RLFLA.

We have designed a simulation where an infinitesimal dipole source and a RLFLA were located in a homogeneous medium ($\varepsilon_r = 12$). Both antennas are embedded in the 3D cube with dimensions of 6m x 1m x 12m and no borehole is presented. The horizontal distance of the Tx and Rx are 5 m and setup included a Tx in 6 m depth and in total 45 Rx antenna are located in depth of 1.5m to 10.3m (every 0.2m). We have used the in infinitesimal dipole source and RLFLA as Tx and Rx.

Figure (4.7) shows the maximum and minimum of the normalised mean wavelet for infinitesimal dipole source and RLFLA versus the transmission angle. As it clear in the top left figure, infinitesimal dipole source minimums and maximums have changed insignificantly for normalised wavelet. In contrast, first and second maximums and minimums (indicated with yellow, purple, green and till respectively) of RLFLA show a systematic shift with increase/ decrease in transmission angle.

4.4.2 Measured data study

We have previously observed the same phenom in studies carried out in Selhausen and Krauthausen test sites of Forschungszentrum Jülich GmbH. that are located in the southern part of the Lower Rhine in Germany. The Selhausen test site is consists of Eolian sediments of Pleistocene and Eocene ages, with a thickness of up to 1 m, cover Quaternary sediments. The groundwater depth shows seasonal fluctuations between 3 and 5 m below the surface. A distinct gradient in soil texture is present with a considerably higher stone content at the upper part of the field [171, 24]. The experiments boreholes are 4 m apart, with maximum offset of 9.3 m and the maximum ray-path distance is 11.2 m that covers ray-path range of $-60 - +60$ degrees. The Krauthausen test site is containing an aquifer structure that made of alluvial terrace sediments, deposited by the Rur river, a local braided river system, on top of older Rhine and Maas sediments. The groundwater level fluctuates between 2 and 4 m seasonally [45]. The experiments boreholes are 0.7 m apart with maximum offset of 2.8 m and the maximum ray-path distance is 4.3 m. The data was acquired from test sites that partially published in [125] and [79] with 200 MHz.sensor and software pulseEKKO GPR crosshole antenna.The recorded traces have been pre-processed with "Dewow" filter and traces are sorted into Common angle gather and then aligned by cross-correlation with the trace in the gather having the highest signal-to-noise ratio (S/N). The figure (4.8) shows the maximum and minimum of the normalised mean wavelet for the Selhausen (above) and Krauthausen (below) test sites versus the transmission angle. The Selhausen data shows the same trends as the RLFLA in the figure (4.7), where increases in transmission angle shift the maximums/minimum right before and after the maximum amplitude. These phenomena are observable in Krauthausen data as well to lower extend.

The agreement between the data measured from two test sites with relatively homogeneous medium and absence of main structure with the results of the FDTD simulation with homogeneous medium with a RLFLA, while the result of infinitesimal dipole source simulation shows no the effect of angular dependency; indicates that the presence of the antenna itself causes this phenomenon.

4.5 3D Crosshole GPR modeling with FLA and borehole fluid

4.5.1 Synthetic simple subsurface model

The results of the borehole fluid effect on travel-time (look at section 4.3) and wavelet angular-dependency (look at section 4.4) emphasis that it is necessary to use a detailed FDTD that include realistic borehole-filling, subsurface medium and RLFLA in order to ensure to capture the behaviour of the crosshole GPR system. Therefore, we have used the gprMax 3D to develop crosshole GPR with integrated borehole-filling and RLFLA. This tool well help up to study the simultaneous effect of the borehole-fluid effect and RLFLA, which can overshadow or maybe even acts against each other in a experiment measurements.

As a proof of concept, we have developed two models with 3D gprMax with integrated borehole and RLFLA. In first model, we built a synthetic subsurface model with $5x2x10$m dimensions, where four layers of medium with ($\varepsilon_r = 5, 21, 10, 18$) and a layer of air ($\varepsilon_r = 1$) from bottom to top are placed, respectively. The setup includes, two boreholes that are 3m apart and each include lower saturated part ($\varepsilon_r = 80$) and unsaturated zone ($\varepsilon_r = 1$) that housed Tx and Rx. In order to examine the EM wave propagation, fields snapshots were captured for every $5e^{-10}$ intervals in three dimensions and all fields components. These snapshots were used by a Matlab scripts to combine the different EM fields and a 3D cube was built to illustrate the propagation of the fields in two perpendicular plane. Figure 4.9 shows an snapshot of the propagation of the EM waves. The video is available on youtube via https://youtu.be/2cBGEtvxcv0.

4.5.2 Synthetic Widen test site model

In the second model, we have modelled the subsurface of the Widen test site, that was studied before in sections (3.3) and (3.4) with three scenarios of the no-borehole presence, air-filled and water-filled boreholes to investigate the effect of the borehole-filing on a realistic subsurface model. The Widen test site is located in Switzerland and was the subject of multiple geophysical and hydrological studies [41, 43, 35]. The aquifer is made of a glaciofluvial deposit with 3 m alluvial loam (silty sand) at top and a 7 m gravel layer with low permeability [33]. The boreholes have an 11.4 cm diameter, and the data is measured with a RAMAC Ground Vision system from Mala Geoscience GPR system with 250 MHz. antennas [83]. The dataset that we used in this study were obtained by 11 Tx with 1 m offset each and 57 Rx position with 0.5 m offset eac, where positioned in reciprocal manner (in total 22 Tx and 114 Rx we recorded). The boreholes are 5 m apart, and all antennas are placed in a saturated zone and depth of 4.6 m to 9.78 m. We used the results of the [83] as ε_r and σ ground truth. We used the original data acquisition setup, boreholes and antennas locations and we used gprMax [169] as a FDTD simulation tool. To include the possible borehole-effect, we built three subsurface models where there a no borehole, two air-filled boreholes and two water-filled boreholes are placed into the ground truth models. We used the 3D GPR RLFLA model (look at section 4.2.1) to reproduced the data to include the possible angular-dependency of the RLFLA. In total, 2508 (22×114) traces are produced for each model that are compared in shot-gathers. As it can seen on figure (4.10) shows a shot-gather of Tx number 5 and Rx 0 -10, where normalised traces are plotted together. As it clear, traces for an air-filled borehole (green) is first to arrive, followed up with no-borehole (red) and latest to arrive is water-filled borehole (blue). These observations are in agreement with our previous experiment for a simple borehole-filling (look at section 4.3); while this effect is not as linear as it was previously observed in a homogeneous medium. Another observation is that water-filled boreholes traces have a longer tail as more secondary events are involved with a strong contrast of the water-filled borehole in compare to the other two scenarios. To have a better view of the simultaneous effect of the borehole -filing on the apparent velocity and the angular dependency of the waveform on the traces, we presented the results as a scatter plot (figure 4.11). We used an automatic picking by identifying the maximum 10% amplitude as an arrival time. As it showed in figure (4.11), there is a visible correlation between the arrival time of the traces in a homogeneous medium and the borehole -filling. Almost always the air-filled borehole- filling (green) cluster has the highest apparent velocity. In contrast, the no borehole-filling has the medium apparent velocity, and the water-filled borehole has the lowest apparent velocity. Despite the easy to spot differences, it is clear that this relationship is not as linear as it was previously observed in section (4.3) as heterogeneity in the medium has an asymmetrical effect on the waveform.

4.6 2.5D crosshole GPR FWI with integrated borehole fluid

As it discussed in section (4.5); the borehole-fluid effect and the angular-dependency of the waveform for RLFLA can have a simultaneous and subtle effect on the measured data. Thus, it is important to include these parameters in any FDTD simulation to represent the data as realistically as possible. This matter is only possible with high-resolution discretisation and access to HPC as these simulations are computationally intensive as RLFLA structure is minimal in comparison to the simulations domain size. Therefore, to include the RLFLA in the simulations, it is necessary to use a very fine mesh for the whole domain that exponentially increase the required computational resources (especially the memory). This issue can be changed drastically, with the implementation of the sub-mesh discretisation that benefits from fine mesh in point of interests (such as RLFLA) and coarser mesh in the main medium body; that unfortunately is not widely available for 3D FDTD right now. Even though we have shown that it is possible to simulate all these effects with an acceptable level of details for a forward model, it is drastically more expensive for FWI as each iteration of the inversion requires four times reconstruction of the subsurface. Therefore, a simple FWI with an average of 20 iterations, requires 80 times high-resolution mesh reconstruction of the entire medium that is simply out of reach at the moment. Therefore, with consideration of the available computing resources and importance; we only integrated the borehole-fluid effect into the 2.5D FWI that was introduced in the section (3.2)[119]. We expect that a borehole-fluid integration will increase the accuracy of the FWI results while keeping the required computational resources at a reasonable level. Despite the clear impact of the FLA in emitted wavelet-shape; integration of the FLA introduce a significant computational intensity to the FWI that will hinder its application. As the FWI requires a backpropagation for calculating the gradient of the cost function (equation 2.31), which is in the current scheme of the FWI done through a single simultaneous shot from the all Rx to the corresponding Tx. As the offset between the Rx is shorter than the half-length of the FLA, it will lead to superpositions of the antenna when the FDTD builds the subsurface model. The FWI is implemented by utilising the message passing interface (MPI), where the number of the Tx is used as the concurrency of the distribution system. Therefore, there is no direct control over which, Rx is built individually. We came up with the idea of grouping the Rx in the subgroups to ensure a sufficient distance between two neighbouring Tx that can be simulated in one single FDTD model. For our RLFLA and the average offset of 0.1 m in the dataset, every 11th Rx can be simulated together without interfering in the subsurface built. It means simply we need to run every single forward model 11 times more, for each time that model is run. On the other hand, to model the RLFLA; it requires using a 0.01 m mesh size to ensure that the smallest component of the system is accommodated by one single cell. The smallest uniform mesh that is previously used by the GPR FWI is 0.03 m. It means accommodating the RLFLA will increase the mesh number in the system 27 times. The compound effect of the exponential increase in the cell size and 11 times increase in the number of the required forward model lead to theoretical almost 300 times more computing resources in both aspects of memory and computing time. Therefore, implementation of the RLFLA is out of the reach until sub-meshing and graphics processing unit (GPU) accelerator is introduced an utilised in FDTD.

As it was discussed in the chapter (3.2); 2.5D FWI is utilising a gprMax as 3D

FDTD and a 3D cube is built by keeping the 2D medium properties invariant in the direction perpendicular to the plane containing the boreholes [144], a method that produces a 2.5D model [149]. To include the borehole models, after building up the 3D properties cube; a search function over-write the properties of the medium in the borehole locations. Thus, small overhead imposed to the FDTD in compare to the simple 2.5D FWI algorithm. The implementation of the borehole filling was verified by comparing the results of the 2.5D FWI with borehole integration and a simple 2.5D FWI with a starting model including the boreholes. The results were in agreement for first arrival waveform as both models expose to the same borehole-filling and as later events arrive differences becomes more significant as borehole integration has a realistic cylindrical shape; while the simple 2.5D FWI simulate the borehole in the starting model as a cube (as it is extended to the 3rd dimension for the whole width of the simulation domain).

4.6.1 Synthetic data produced with water-filled borehole

We have reproduced the data measured in the Widen test site by Klotzsche et al. [83] that was presented in section (4.5.2) by using the gprMax [169], including the borehole-filling models and infinitesimal dipole antennas. We choose a similar model dimension as Klotzsche et al. [83] with 7.62 m $\times$ 11.67 m dimensions using a cell size of 3 cm for the forward modeling and 9 cm for the inversion. The subsurface ε_r and σ models that are used as ground truth are presented in the figure (4.12). We have used the starting model that was used by Mozaffari et al. [119] as 2.5D FWI shows that it is more sensitive to the accuracy of the starting models than 2D FWI (please look at section 3.3.1.1 for more information). As we want to purely study the effect of the borehole-fluid integration in FWI; we refrained to deploy any inversion optimisation scheme that is discussed in section (3.3.2) and we only used direct 2.5D FWI. As it was pointed out before, detailed FWI requires extensive computational resources. Thus, all computations were carried out on JURECA cluster [88], which is part of the Jülich Supercomputing Centre (JSC). The 2D FWI was carried out on 128 GB memory node with average wall-time of $\approx$ 0.3 c-h per iterations ; while the 2.5D variations of FWI were executed on nodes with 512 GB with average wall-time of $\approx$ 96 c-h per iterations.

In order to compare the performance of the borehole-filling integration in FWI, we invert the synthetic data with 2.5D FWI with borehole-integration, simple 2.5D FWI and 2D FWI (that both were extensively discussed in chapter 3) with an identical starting models as it showed in figure (4.13). As the data is synthetically produced; the original source wavelet is known to us, therefore there is no need for source-wavelet estimation.

By skipping the source wavelet estimation; we used the known source wavelet (that was used to produced the synthetic data) with corresponding forward models to estimate the effective source wavelet (section 2.5.3.3). As it is explained in (2.5.3), each source wavelet is corrected to accommodate all uncertainty every forward model inherits by nature (please look at 2.3.1.3). Figure (4.14) shows the effective source wavelet for 2D FWI, 2.5D FWI and 2.5D FWI with integrated borehole-fluid after multiple corrections steps. We believe as the forward model is more detailed and complete; it carries less uncertainty, and therefore it could produce more accurate results.

4.6.2 Results

We used the same termination criteria to stop all three inversion, where the change of the RMS error value in two consecutive iterations was less than 0.5%. The 2D FWI was stopped after 23 iterations, while the vanilla 2.5D FWI and FWI with boreheole-fluid integration were stopped after 21 iterations. Note that also a good data fit and no remaining gradient was present for all inversion results. The normalised RMS misfit to the starting models for all three variation of the FWI is presented in figure (4.15).

The ε_r and σ tomograms obtained from 2D, 2.5D and 2.5D FWI with integrated borehole-fluid are shown in figure (4.16). Comparing the results with the reference models (Figure 4.12) shows that 2.5D variation of FWI were more successful to qualitatively resolve the main features of the ε_r and the σ tomograms than 2D FWI. The 2D FWI The ε_r tomogram constructed by the 2D FWI has less distinctive features than 2.5D FWI variations, while the results of the 2D FWI appear to be smoother than those from the 2.5D FWI. The σ tomograms are well-reconstructed for all three FWI as the results shows main features of the synthetic input model.

Despite the fact that the tomograms look similar from a qualitative perspective, a quantitative comparison shows differences in accuracy. In order to localize error for each of these three sets of results, a model error based on equation (3.1) is calculated for each cells in compare to the value in reference model. Figure (4.17) shows the model for all there variation o the FWI. The 2D FWI overestimates ε_r between 4.2 m - 5.7 m, where the model error reaches 45%. The obtained ε_r results for the 2.5D FWI variations fit better the reference model at the interface between the upper high-velocity zone and the low-velocity waveguide. Even though, there is a visible trapped gradient next to the borehole in 6m distance for 2.5D FWI with borehole-fluid integration; the model error shows improvement in comparison with vanilla 2.5D FWI. These observations are in agreement with our findings in chapter (4.3) as borehole-fluid integration has a significant effect on the travel time of the EM wave in the medium. The traveltime differences in 2.5DFWI variations leads to better reconstruction of the ε_r model. The AE for ε_r and σ, average computing time for 21 iterations and the RMS reduction for normalised starting models are presented in table (4.1).

It worth to mention that the results of the FWI show that model error increases next to the borehole location. Presence of these artefacts could be explained by exploding gradient near-distance from the Tx. The pheromone was previously observed and addressed using preconditioning of gradient [82]. The preconditioning of gradient was not available by the time of the coupling with the FWI with gprMax. We expect that the gradient preconditioning reduces the artefacts, and blank area near to boreholes.

Table 4.1: using 2D FWI, 2.5D FWI vanilla and 2.5D FWI with boreheole-fluid integration using same starting models SM. Maximum lateral average error (LAE) and average error (AE) for the entire domain between the boreholes for ε_r and σ, Computation time (CT) for 20 consecutive iterations and RMS reduction normalised to the starting models

FWI strategy	ε_r AE %	σ AE %	CT (min)	RMS reduction %
2D	2.6	5.13	4.5	34
2.5D vanilla	1.1	- 0.18	1196.7	52
2.5D with borehole-fluid integration	0.45	-0.81	2836.4	63

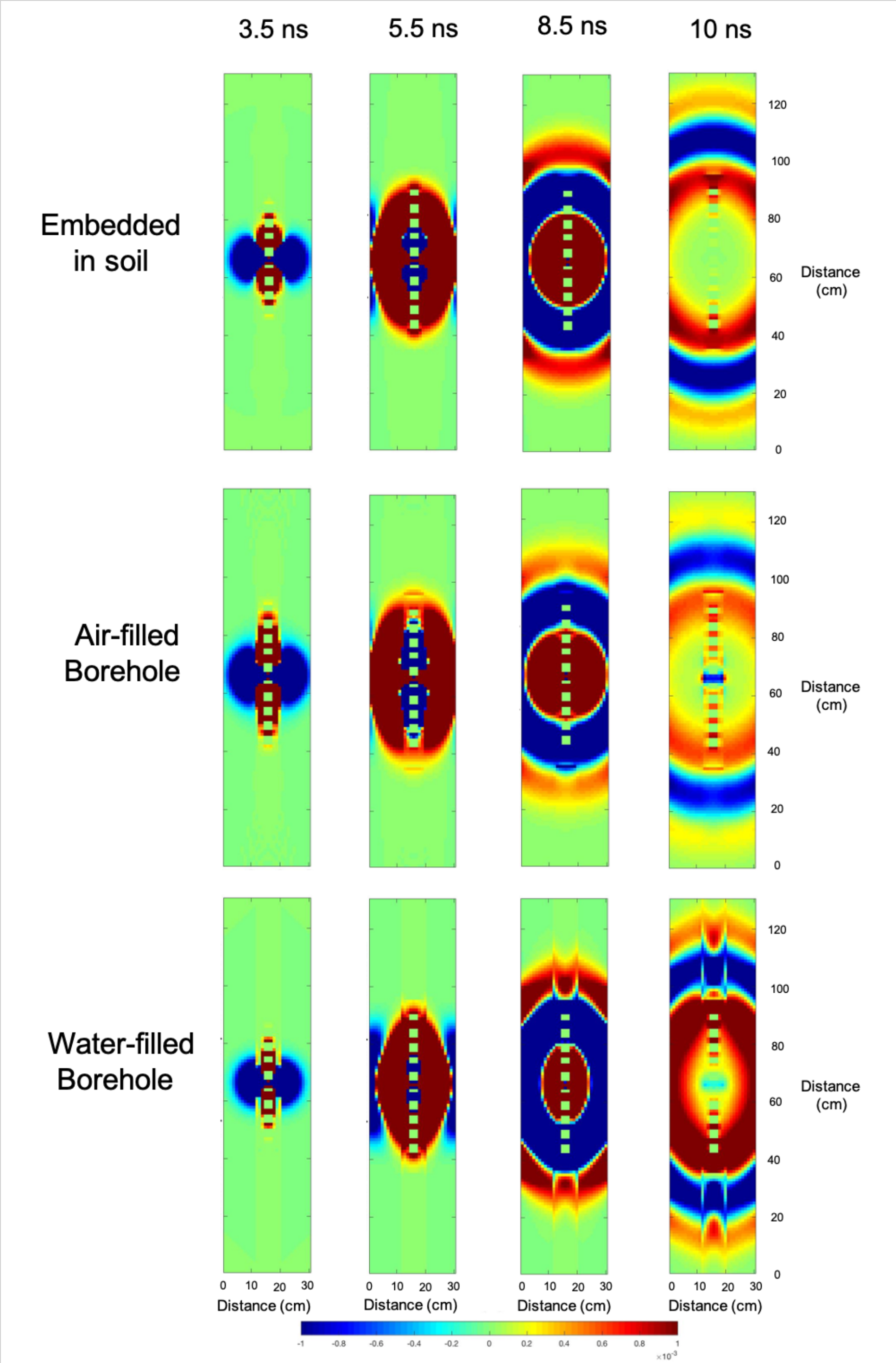

Figure 4.5: The EM wave propagation for the RLFLA embedded (top), located in air-filled borehole ($\varepsilon_r = 1$) (middle), and located in water-filled borehole (bottom) ($\varepsilon_r = 80$) all in homogeneous soil ($\varepsilon_r = 12$) for several time-steps

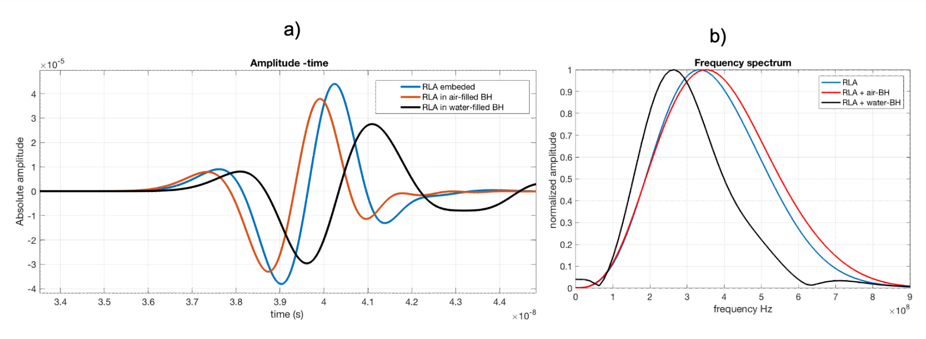

Figure 4.6: Left) Absolute amplitude of the RLFLA antenna embedded in the soil and placed in the air-filled and water-filled boreholes; right) the frequency spectrum of the normalised signals for RLFLA embedded and located in air and water-filled boreholes

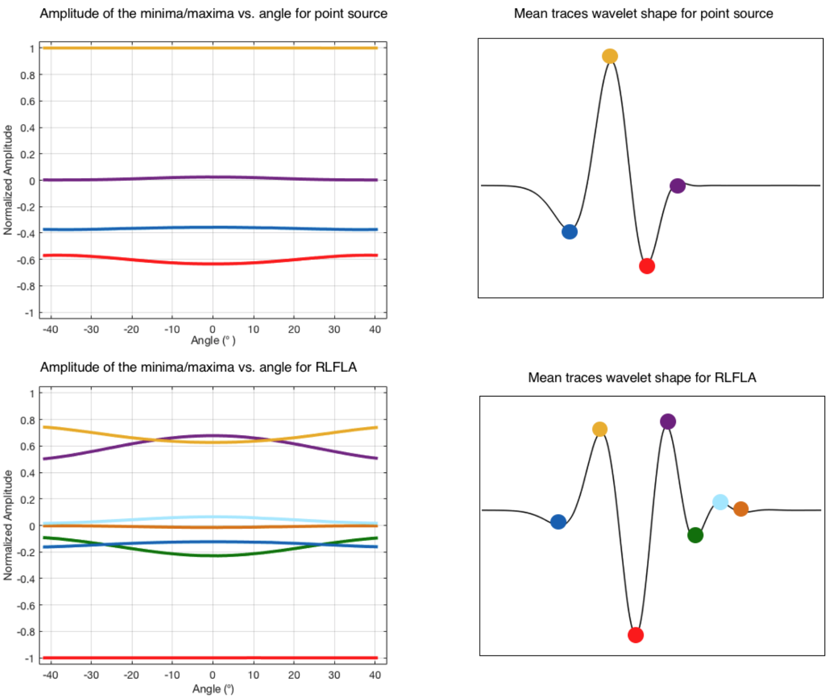

Figure 4.7: Mean wavelet minimums and maximums for infinitesimal dipole source and RLFLA for transmission angle -40 to +40 degree

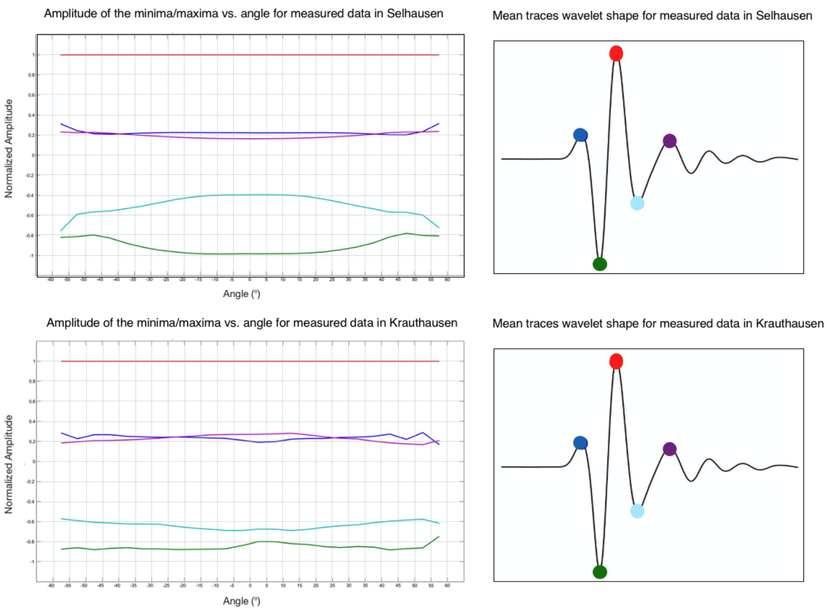

Figure 4.8: Mean wavelet minimums and maximums for Selhausen (above) and Krauthausen (below) test sites for transmission angle -60 to +60 degree

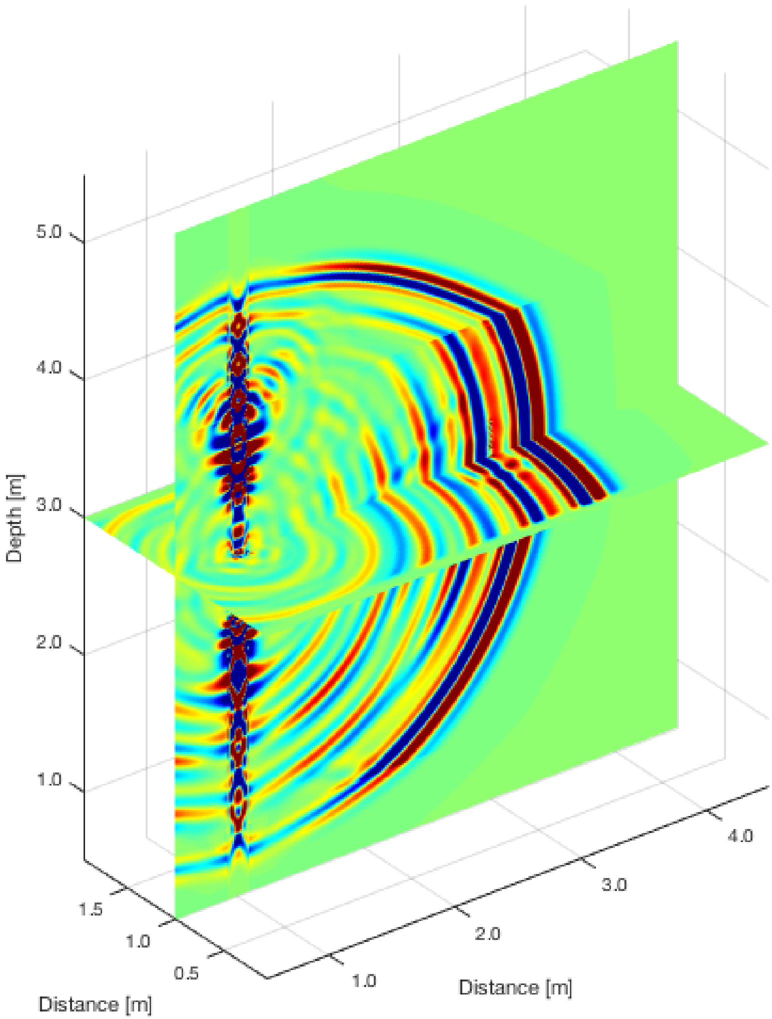

Figure 4.9: Cross-section of a 3D model of subsurface with using gprMax with integrated borehole-fluid and RLFLA models

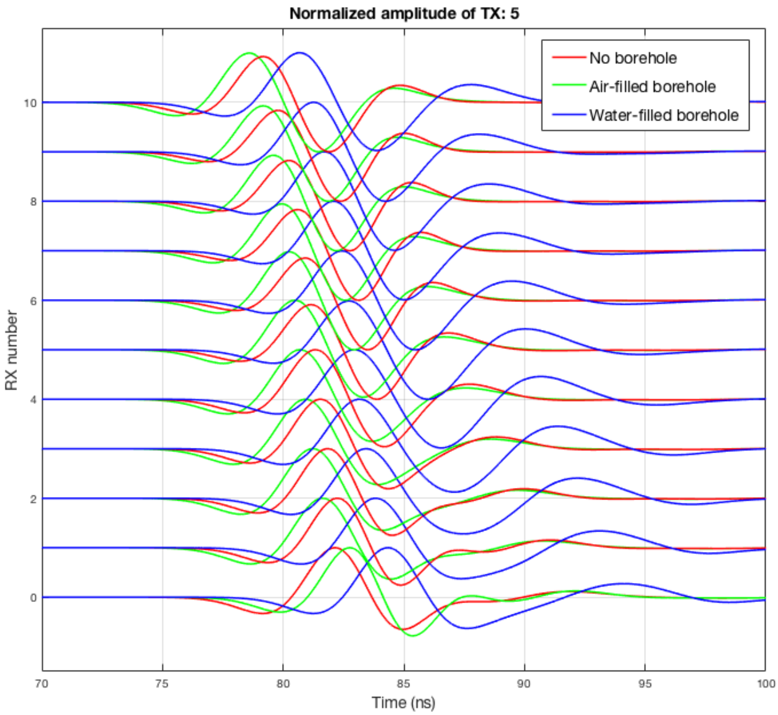

Figure 4.10: Shot-gather for Tx:5 and 10 Rx for No Borehole (red), air-filled borehole (green) and water-filled borehole (blue)

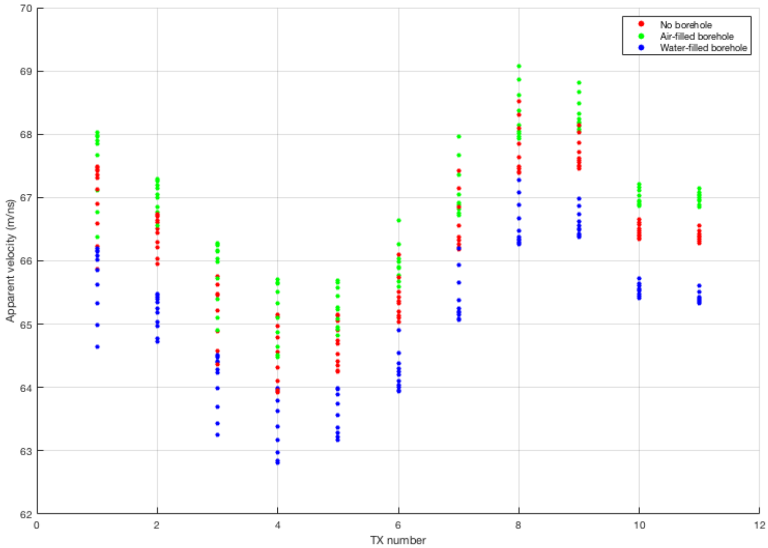

Figure 4.11: A cluster of travel-time for 1 - 11 Tx and 57 Rx that for 3D subsurface model for three cases of no borehole (red), air-filled borehole (green) and water-filled borehole with RLFLA (blue)

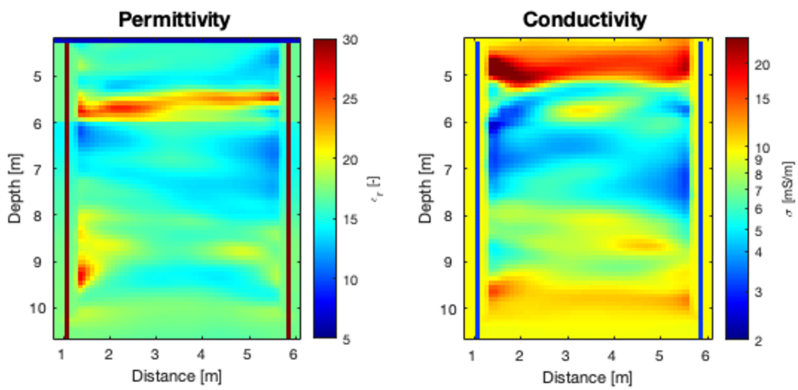

Figure 4.12: The ground -truth left) ε_r right) σ models that are used to produce the synthetic data with a air-filled borehole filling in unsaturated area and water-filled borehole in saturated area

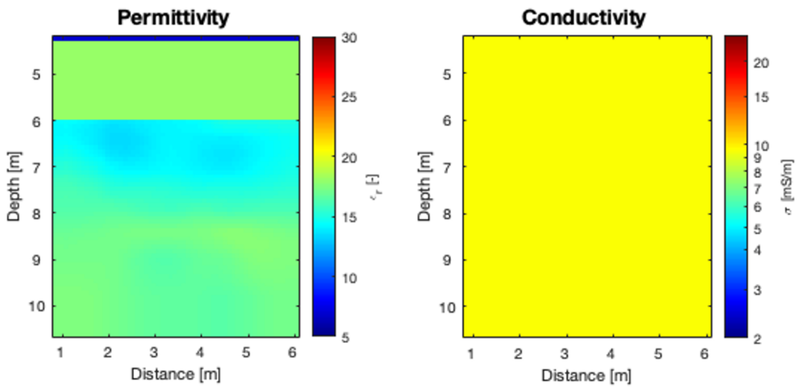

Figure 4.13: Left) ε_r right) σ starting models that are used for 2D, 2.5D vanilla and borehole-integrated FWI

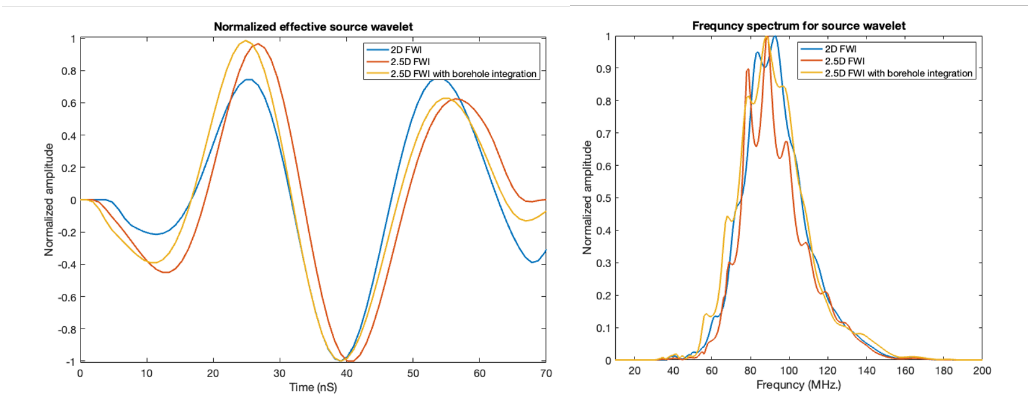

Figure 4.14: Left) Effective source wavelet for 2D FWI (blue), 2.5D FWI (red) and 2.5D FWI with borehole integration (gold) after source-wavelet correction, right) corresponding one-sided frequency spectrum

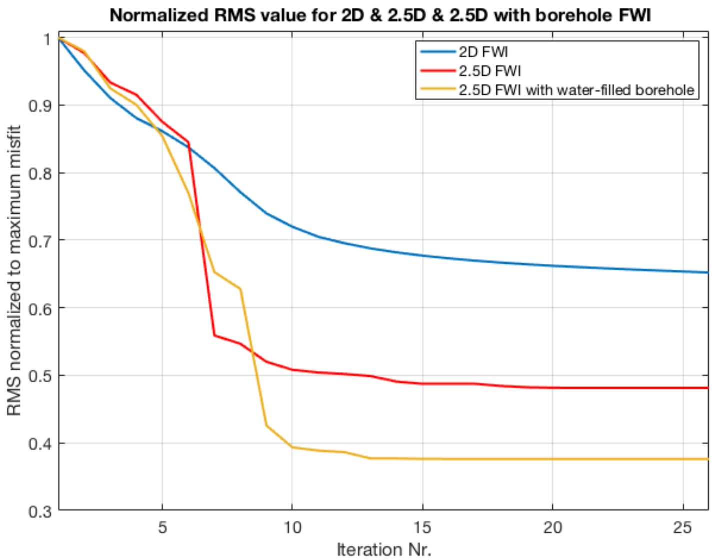

Figure 4.15: RMS misfit curves for 2D FWI (blue), 2.5D FWI (red) and 2.5D FWI with borehole-fluid integration (gold) using the same starting models. RMS curves are normalised to the starting model value (iteration 0).

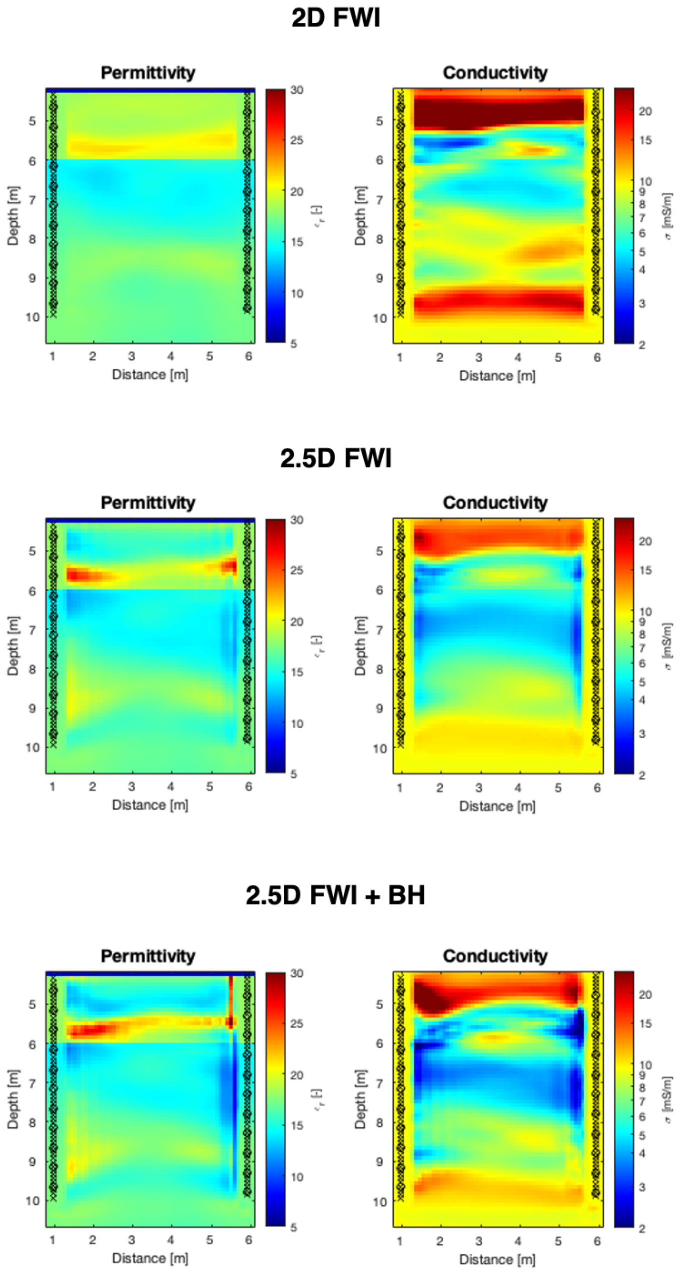

Figure 4.16: Left)ε_r and right)σ models for 2D (above), 2.5D FWI (middle), 2.5D FWI with borehole-fluid integration (bottom) Note the logarithmic scale for σ tomograms. Tx and Rx positions are indicated by circle and crosses, respectively.

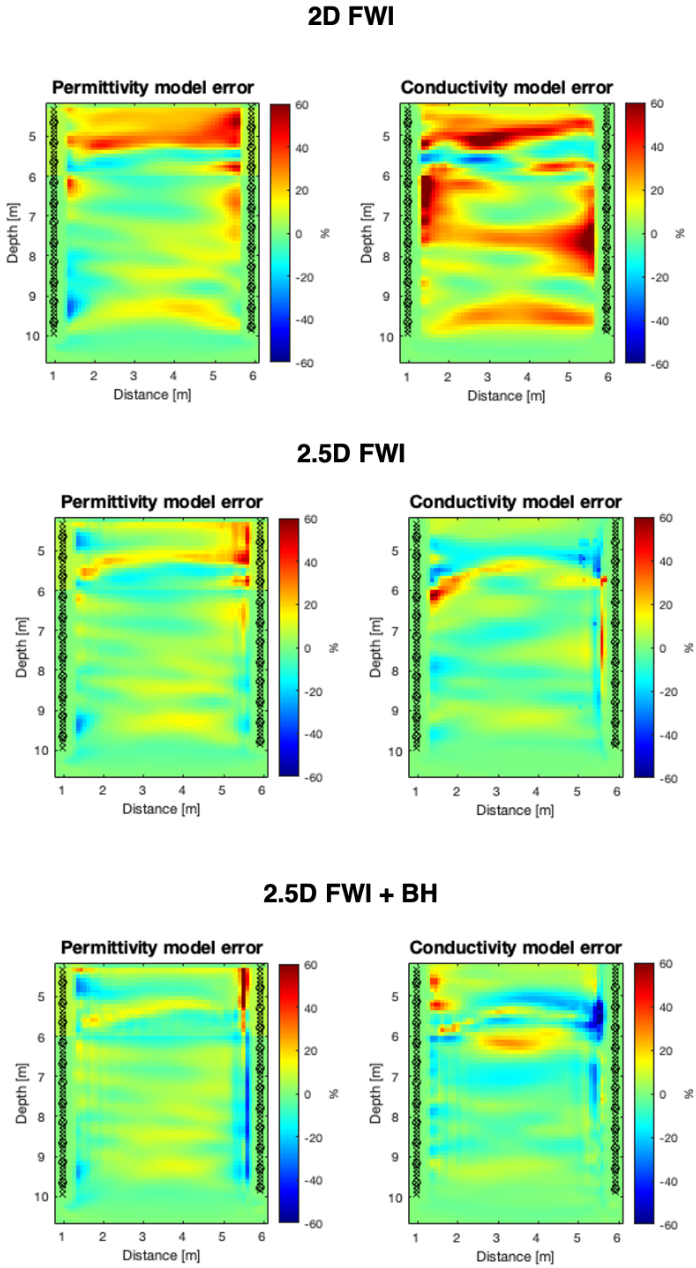

Figure 4.17: Left) model error percentage of ε_r and right) of σ models for 2D (above), 2.5D FWI (middle), 2.5D FWI with borehole-fluid integration (bottom). Transmitter and receiver positions are indicated by circle and crosses, respectively.

4.7 Conclusion

In this chapter, we have investigated the effect of the borehole-fluid and RLFLA on EM wave travel time and angular-dependency of the emitted wavelet. Even though, impact of the borehole-fluid on crosshole GPR data was known in previous studies, due to computational intensity required for the fine discretisation of the computing domain; it is rarely included in forward modelling tools. The challenge of computational intensity for crosshole GPR is even more amplified for modelling of the realistic antenna models as dimensions of the crosshole antennas are much smaller than the target domain. Despite the usefulness of the theoretical infinitesimal dipole source to avoid computationally expensive realistic 3D antenna modelling, it assumes that the radiation pattern for the antenna is symmetrical. We have verified this assumption with historical data obtained from fairly homogeneous test sites. We demonstrated that borehole-fluid effect and RLFLA angular-dependency have a complex and intertwine effect on travel times, wavelet-shape and the amplitude assigned to the EM waves. Therefore, to improve the outcomes of the 3D forward model, to overcome the restrictions of the infinitesimal dipole source assumption and to minimise the associated errors in the crosshole GPR, we developed a borehole-fluid and RLFLA models that we have verified in series of bench-marking efforts. Moreover, we have extend the 3D forward model of our 2.5D crosshole GPR FWI to include the borehole-fluid model.

The 2.5D FWI with integrated borehole-fluid uses gprMax as a complete 3D FDTD modeling kernel that build a 3D cube of target medium and the borehole-fluid model. We compared the performance of conventional 2D FWI, vanilla 2.5D FWI and the 2.5D FWI with the borehole-fluid integrated for realistic synthetic data. The results for 2.5D FWI with borehole-fluid model showed higher accuracy in estimated ε_r and provided lower AE in tomograms. This observation is in agreement with our hypothesis as borehole-fluid significantly contributes to travel time of the EM wave that associated with the ε_r of the target medium. Overall, we demonstrated that improvement in forward modelling tool has a direct impact on the accuracy of the modelled subsurface. As FWI utilise the forward model multiple times; these improvements translate in the improvement of the inversion results. While, integration of the borehole-fluid model in FWI demonstrate enhancement of the results; we believe that advancement in FDTD such as integration of GPU accelerator and subgrid discretisation could be great leap forward to implement the RLFLA into FWI.

Chapter 5

High resolution 3D EM modelling: A new correction to use high-angle crosshole GPR traveltime data[1]

This chapter explores contributing factors to an issue known as inconsistency of travel time data inversion in high-angle crosshole GPR. First, we carried a detailed literature review in the subject of the high-angle inconsistency of travel time inversion. As we have seen, the travel time is influenced by the borehole-fluid in the chapter; we introduced a correction factor that uses a ray-tracing for correcting the errors that it can impose to inversion. Finally, we validate this hypothesis and correction factor for two cases of synthetic studies.

5.1 Crosshole GPR high-angle problem

As it discussed in the section (1.3), GPR has gained popularity as a tool for high-resolution imaging of the near surface [154, 44, 86]. Whereas zero-offset measurements provide low-resolution images by using only horizontally traveling waves, high-resolution tomograms can be obtained from inverting data acquired by using a wide-range of raypath angles including Tx-Rx's pairs that produce high-angle raypaths [113, 21, 136]. However, artefacts have been observed in the inverted GPR tomograms when high-angle data were incorporated in ray-based tomography and inversions [128]. In addition to the increasing noise level that makes the picking of the first-arrival high-angle travel-times more challenging, an increasing apparent velocity for increasing ray-path angles has been observed, where the apparent-velocity was calculated by dividing the direct distance between Tx and Rx over the first-arrival traveltime. Irving, Knoll, and Knight [73] clearly showed a systematically increase in the recorded apparent velocity for increasing ray-path angles as shown in figure (5.1) for data acquired at Boise Hydrological Research Site (BHRS), which was described

[1]Mozaffari, A., Klotzsche, Zhou, Z., A., Vereecken, H., & van der Kruk, J. (2021). *3D electromagnetic modelling explains the apparent velocity increase in crosshole GPR data - borehole fluid effect correction method enables the incorporation of high-angle travel time data* . IEEE Transactions on Geoscience and Remote Sensing, 1–10. `https://doi.org/10.1109/TGRS.2021.3107451`.

as an “incompatibility of high-angle data”. Peterson [128] reduced the artefacts in the inversion results by using only data with angular apertures up to 50° and ignoring high-angle data. Alumbaugh et al. [2] limited the raypath angles to 45° because of similar observations that they explained as a possible short circuit between the Tx and Rx’s communication cables installed in the boreholes. Another possible explanation was given by Irving and Knight [72], who stated that the increasing apparent velocity for increasing ray-path angle is caused by a higher wave velocity in the antennas compared to the wave velocity in the surrounding medium. In this way, waves emitted from the tip of the Tx antenna travelling to the Rx antenna’s tip have a faster ray-path compared to waves directly travelling from the feed point of the Tx antenna to the voltage gap of the Rx antenna. Irving, Knoll, and Knight [73] indicated that the high-angle waveform picks are distorted due to the finite-length antenna (FLA), the borehole-fluid effect, and, difficulties to pick a correct first arrival due to a low signal to noise ratio. They also introduced a heuristic approach to incorporate the high-angle raypaths by using a traveltime correction curve as function of the raypath angle to compensate the increasing apparent-velocity for increasing raypath angle assuming the zero-angle raypath velocities being correct. We should note that this phenomenon has been only observed for GPR crosshole data, a seismic crosshole study carried out by Moret et al. [117] at the BHRS did not show an increasing apparent-velocity with increasing raypath angle. Since Peterson [128] study, limiting the angular aperture to a particular threshold up to 30° to 50° became a standard pre-processing step for ray-based crosshole tomography inversion. Over 30 papers and studies used a limited angular aperture based on the findings of Peterson [128] and Alumbaugh et al. [2], e.g., for ray-based tomography [3, 31, 98, 30, 61, 97, 38], stochastic tomography [103, 62, 102, 179, 131, 71], time-lapse monitoring [109, 29, 93] and FWI [46, 34, 13, 59, 78].

Despite the popularity of the limited angular aperture for reasonable subsurface imaging; it harms the quality of tomograms [11, 73]. Menke [113] observed that resolution of the crosshole seismic is dependent on the angular aperture and for most of the crosshole setup; the horizontal resolution of the seismic crosshole is worse than vertical resolution by a factor of two. Bregman, Bailey, and Chapman [21] found that limiting the angular coverage arises a large-scale ambiguity in crosswell tomograms. They also emphasised that the presence of the vertical ray-path is necessary to identify the presence of the continuous vertical structure between the boreholes. It is assumed the minimum feature size resolvable by ray-tomography is scaled to the first Fresnel zone $\sqrt{\lambda L}$ [175]. Rector and Washbourne [136] found that limiting the angular aperture smear the resolution in the direction of the limited angle. They showed that with intense angular limitation, the angular aperture could be a limiting factor that controls the spatial resolution of the crosswell traveltime tomography. Hardage [63] showed that limited angular aperture means that specific frequencies of the interval 2D spatial spectrum are not illuminated. The issue that Rector and Washbourne [136] termed it as *effect of projection truncation* and said it could be interpreted as smoothing or whiting filter applied to the 2D spectrum that increases the variation of the reconstructed 2D image but does not affect the resolution. Therefore, a limited vertical aperture of crosshole survey introduced a small amount of non-uniqueness and significantly reduced the resolution.

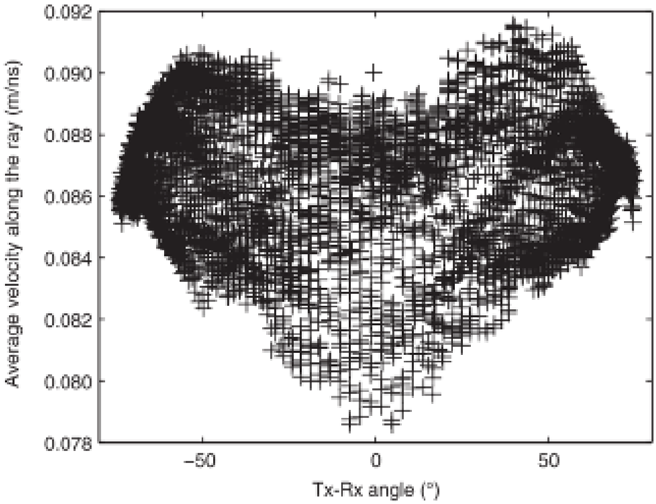

Figure 5.1: Average (apparent) velocity versus raypath angle for crosshole GPR data acquired from BHRS by Irving, Knoll, and Knight [73], which shows an increase of apparent-velocity with increasing Tx – Rx raypath angle

In summary, by including high-angle raypaths having increased apparent-velocities results in tomography inversion artefacts. However, by removing high-angle raypaths one significantly reduces the spatial resolution, so both options have a disadvantage. Several possible explanations for this increasing apparent velocity have been suggested, but no detailed study has been performed to investigate the actual cause of this phenomenon, probably due to the lack of available modelling codes and computer resources that enable including all the possible reasons in the analysis. Here, we investigate in detail the hypothesis that difficulties and inconsistency of high angle issue caused to some extent by refraction occurs in boreholes interface; by using a detailed 3D FDTD model that is able to include the presence of the borehole, borehole fluid and Tx and Rx being RLFLA. In the following, we explain the physics and show a possible reason for the increase in apparent velocity for increasing raypath angle. Furthermore, we introduce a novel borehole-fluid effect correction (BFEC) method that returns improved apparent-velocity values such that also high-angle raypaths can be included in a ray-based tomography to obtain an improved traveltime inversion result.

5.2 Novel pre-processing borehole-fluid effect correction resulting in improve in apparent velocity values

We investigate the wave propagation between the Tx and Rx boreholes by including the refractions that occur on the boundaries between media having different wave velocities under the assumption of the far-field regime and low electrical conductivity. The far-field assumption helps us simplify the setup, even though it is not always valid as boreholes and antennas are located in a near-field regime and possible errors could occur. We use Snell's law (equation 2.11) that describes the refraction at the borehole interface as the ratio of the sinus of the incident angle ϕ_1 divided by the sinus of the transmitted angle ϕ_2 , which equals the ratio of the two velocities or the inverse ratio of the squares of the relative permittivity ε_r in the borehole-fluid ε_1 and subsurface ε_2 [55]:

$$\frac{\sin \varnothing_1}{\sin \varnothing_2} = \frac{v_1}{v_2} \rightarrow \sin \varnothing_2 = \sin \varnothing_1 \times \frac{v_2}{v_1} = \sin \varnothing_1 \times \sqrt{\frac{\varepsilon_1}{\varepsilon_2}}\ , \tag{5.1}$$

where $\sin \phi_1$ and $\sin \phi_2$ are the incident and transmitted angles with EM wave velocities v_1 and v_2 in the borehole and subsurface, respectively. Similarly, we can write for the interface between the subsurface (ε_2) and the Rx borehole with borehole fluid ε_3 and transmitted angle of ϕ_3 as follows:

$$\sin \varnothing_3 = \sin \varnothing_2 \times \frac{v_3}{v_2} \rightarrow \sin \varnothing_3 = \sin \varnothing_1 \times \frac{v_3}{v_1} = \sin \varnothing_1 \times \sqrt{\frac{\varepsilon_1}{\varepsilon_3}}\ . \tag{5.2}$$

Even though the geometrical restriction of the crosshole setup ensures that boreholes are contained in a single perpendicular plain, which will reduce the out-of-plane scattering, it will not be zero. In this study, we only want to correct the first arrivals and not the full wave of the transmitted electromagnetic waves. We can safely assume that waves that travelled in the containing plane arrived earlier than the remaining waveform affected by the borehole's cylindrical geometry. For applying this correction to a full waveform data and to possible full-waveform inversion, more studies are necessary. Another fundamental law, which we are using in our correction method, is total internal reflection which could only occur when EM waves travel from a medium with lower velocity to a medium with higher velocity. Equation (5.2) shows the critical angle for EM waves travel from a first medium with (ε_1) to a second medium with (ε_2) where ($\varepsilon_2 > \varepsilon_1$),

$$\varnothing_{cr.} = Arcsin\left(\frac{v_1}{v_2}\right) = Arcsin\left(\sqrt{\frac{\varepsilon_2}{\varepsilon_1}}\right), \tag{5.3}$$

No refraction occurs when the Tx and Rx are at equal depth and rays are traveling horizontally. In the following, we will introduce three possible raypaths that can be used to describe or approximate this phenomenon as presented in figure (5.2).

When the medium properties in the boreholes and the medium between the boreholes are equal or we ignore any refraction that is occurring, we can assume a straight line between the Tx and Rx. We refer to this raypath model in the following as “no refraction” (N), see also figure (5.2b). For the borehole fluid (e.g., water) and subsurface relative permittivities are $\varepsilon_1 = 80$ a $4 < \varepsilon_1 < 30$ respectively, the equation (5.4) restricts the ϕ_1^S (or ϕ_3^S) and we obtain a small ratio in equation (5.3).

When we approximate this ratio as being zero, the incident angle equals zero ($\phi_1^S = 0$) We refer to this raypath model as “simple refraction” (S). The approximated refraction point (PRS) is located at the same depth of the source or Rx at the interface between the borehole and subsurface. For the two raypath models discussed before, the traveltime can be easily calculated as a function of the vertical distance between the Tx and Rx (h) and the horizontal distance between Tx and Rx that includes the distance between the two boreholes (d_{subs}) and radius of the boreholes (r_b) which we assume to be equal. We introduce a simple borehole-fluid effect correction (simple BFEC), where the traveltimes in the fluid-filled boreholes are subtracted from the total traveltime and the Tx and Rx antennas are relocated at the location of the approximated refraction points (PRS) to calculate the apparent velocity. For the “True refraction” (T) raypath model, we consider all refractions at all interfaces, and the traveltime cannot be analytically determined since it depends on the angle (ϕ_1^S)that is unknown and needs to be estimated first. Therefore, we project all travelpaths to the vertical axis as follows:

$$h = h_1 + h_2 + h_3, \tag{5.4}$$

$$h = d_1 \times \tan \varnothing_1 + d_2 \times \tan \varnothing_2 + d_3 \times \tan \varnothing_3, \tag{5.5}$$

where h, h_1, h_2 and h_3 are vertical projections of the distance traveled in the first borehole, subsurface, and second borehole, respectively (look at figure 5.2).

Then, we transformed equation (5.5) to an equivalent in sin function by using the equations (5.1) and (5.2). Thereby, we replaced the $\sin\phi_2$ and sin $\sin\phi_3$ with equivalent $\sin\phi_1$ as following:

$$h = d_1 \times \frac{(\sin\phi_1)^2}{1-(\sin\phi_1)^2} + d_2 \times \frac{(\sin\phi_2)^2}{1-(\sin\phi_2)^2} + d_3 \times \frac{(\sin\phi_3)^2}{1-(\sin\phi_3)^2}, \tag{5.6}$$

$$h = d_1 \times \frac{(\sin\phi_1)^2}{1-(\sin\phi_1)^2} + d_2 \times \frac{(\sin\phi_1 \times \frac{v_2}{v_1})^2}{1-(\sin\phi_1 \times \frac{v_2}{v_1})^2} + d_3 \times \frac{(\sin\phi_1 \times \frac{v_3}{v_1})^2}{1-(\sin\phi_1 \times \frac{v_3}{v_1})^2}, \tag{5.7}$$

Based on an assumption of high frequency for radar wave, and low loss attenuation and non-magnetic mediums; we substitute ε_1 and ε_3 with ε_{water} and ε_2 with ε_{subs} in equations (5.1) and (5.2), followed by their substitution into equation (5.7), to obtain the following equation:

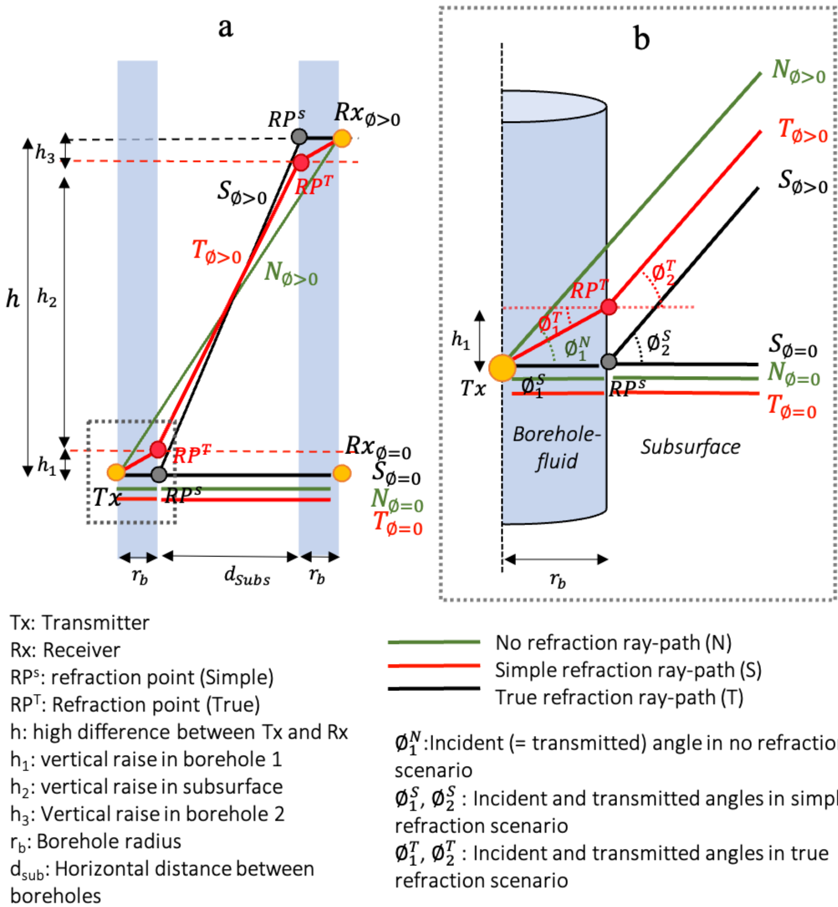

Figure 5.2: a)Ray paths with no refraction (N), true refraction (T), and simple refraction (S) for zero-degree ($\phi = 0$) and arbitrary ($\phi > 0$) ay angle b) Close up view of the ray-paths at the interface between the borehole-fluid and the subsurface where the refraction point for simple refraction and true refraction are indicated by (PRS) and (PRT), respectively.

$$h = 2 \times \left(\frac{r_b \times \sin \varnothing_1}{\sqrt{1 - (\sin \varnothing_1)^2}} \right) + \left(\frac{d_{subs} \times \sin \varnothing_1 \times \sqrt{\varepsilon_{water}}}{\sqrt{\varepsilon_{subs} - \varepsilon_{water} \times (\sin \varnothing_1)^2}} \right), \tag{5.8}$$

from which, combine by the restriction determined by the equation (5.3) ; we can numerically solve (ϕ_1) by assuming a known ε_{subs}. When (ϕ_1) is known, we can calculate the travel distances inside the boreholes and the corresponding traveltimes. When we subtract these from the total travel distances and traveltimes, respectively, and relocate the Tx and Rx positions to the refraction-point locations at the borehole/subsurface interface, corrected apparent velocities of the subsurface can be obtained that are not influenced by the presence of the borehole fluid (look at figure 5.2). It is important to note that we considered freshwater as borehole fluid with a temperature of 25 degree. The presence of soil and mud in the borehole can affect the permittivity, and therefore we focused on cases, where borehole casing is present, and/or the boreholes are sealed. Note, the method presented here can easily be adapted to the considered experimental setup including the fluid temperature and the permittivity of fluid.

While the horizontal distance of the refraction-point from the Tx (or Rx) is constant and equal to the radius of the borehole r_b, the vertical difference h1 (or h3) is depending on the refraction that is depending on the borehole fluid, subsurface velocity and the radius of the borehole r_b. Therefore, for each single Tx-Rx combination, there will be a different refraction point RPT . In principle, all Tx and Rx locations can be updated towards the true refraction points RPT however, this will result in Tx and Rx positions that change depending on which direction the wave is emitted or received. Depending on which Tx-Rx combination is used, the h_1 (or h_3) corrections are varying for different depths between 0 cm to 3 cm for the setup discussed here. To have one fixed position for each Tx and Rx, we averaged the h_1 (or h_3) corrections for each Tx (and Rx) separately and fixed the depth of the refraction points RPT for each Tx (and Rx). Note that the maximum difference between the averaged h_1 (or h_3) and the true refraction point RPT is limited to 1.5 cm for this study. This averaging procedure enables us to use conventional ray-based inversion methods after the correction without unnecessarily complicated bookkeeping of the Tx and Rx positions caused by these small variations in depths. We term the above mention method as true BFEC. It is important to note that, for the borehole fluid (e.g. air) with relative permittivity lower than subsurface, the equation (5.3) restricts the ϕ_2, which means the significant vertical raise in the subsurface should happen inside the boreholes h_1 (or h_3). Therefore, the refraction points RPT , move drastically alongside the borehole interface by increasing the ϕ_1; thereby, our correction method could not be extended to the air-filled boreholes without modification.

5.3 3D FDTD modelling

In this chapter, we have used the gprMax 3D [169] that was introduced in chapter (3) as the FDTD kernel (for more information please look at 2.2). We have utilised the borehole-fluid and RLFLA models that we developed and verified in chapter (4) for the following case studies.

5.4 Case study 1: simple layered subsurface model

We construct a 3D subsurface model similar to the dimensions as investigated by Irving, Knoll, and Knight [73] returning increasing apparent velocities as shown in figure (5.1). These data were measured at the BHRS near Boise, Idaho in the United States where a shallow unconfined aquifer consists of an approximately 18-m-thick layer of coarse, unconsolidated, braided-stream deposits (gravels and cobbles with sand lenses), which is underlain by clay and basalt. Our 3D gprMax3D model has dimensions of $5.5m \times 2.0m \times 22.0m$ and a uniform 1 cm discretisation. It consists of 1 m layer of air with dielectric relative permittivity $\varepsilon_r = 1$ on top, 3 m unsaturated gravel with $\varepsilon_r = 5$, a 15 m layer of saturated gravel with $\varepsilon_r = 12.15$, and at the bottom 3 m layer of clay bedrock with $\varepsilon_r = 18$. Two 18-m-deep boreholes are present with 3.5 m distance and inner radius of 5 cm.

We build a model by considering the inner radius of the borehole filled with water in the saturated area $\varepsilon_r = 80$ and the air-filled area of $\varepsilon_r = 1$. As the radius of the antenna is 0.02m, and the borehole radius is 0.05, only a 0.03 m column of water is surrounding the RLFLA .Because the point source antenna has no dimension, therefore, we used the borehole with 3 cm inner radius for the point source model to be consistent and comparable with the results of the RLFLA. We put a Tx located at a depth of 11 m and placed 12 Rx from 6 m to 17 m depth in the homogeneous saturated gravel layer. This setup geometry provides us an angular coverage of -60 to +60 degree. We carried out separate simulations for each Tx – Rx position pair. Every simulation was carried out once for identical transmitter-receiver pairs as point sources and once as RLFLA.

We have used an automated picking method to locate the first local minimum.To obtain the actual first break of the waves, we defined a constant that indicates the time difference between first break and the first minimum and subtracted it from the first minimum time. The two lower curves in figure (5.3a) show the apparent velocities for the picked minima from the modeled point source (orange line) and RLFLA (purple line) data. The calculated first breaks using the constant were confirmed by manual picking. An increasing apparent velocity for increasing raypath angle is observed similar to Irving, Knoll, and Knight [73] (look at figure 5.1). As shown in figure (5.3), the first minima of the RLFLA arrives slightly earlier than for the point source. This is due to the different effective wavelets that are emitted/received by the point Tx/Rx and the RLFLAs, and the antenna insulation thickness which has lower relative permittivity in compare to the subsurface that causes a constant drift between the two lower curves of figure (5.3a). When we compensate for the first local minima arrival within the waveform and the constant shift caused by the antenna-insulation thickness; we obtain almost overlying apparent-velocity curves (look at figure 5.3). These results show that the increasing apparent velocity with increasing raypath angle is not caused be the RLFLA since both point source/Rx and RLFLAs show very similar results. Comparing the obtained results with the true velocity of the medium, we see that the results are still significantly off. The corrected point source/Rx and RLFLA's results for zero-angle raypaths and "no refraction" ray-based model (N)

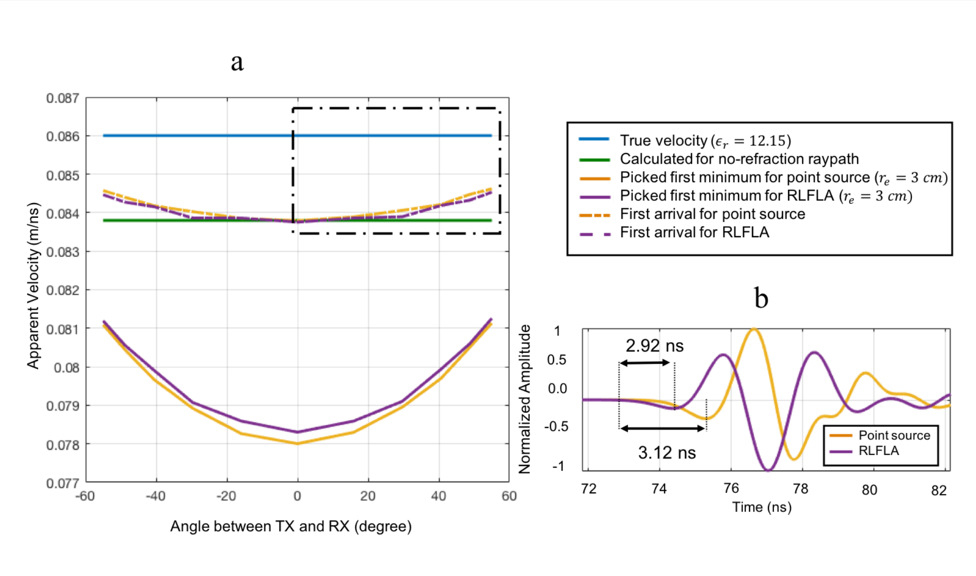

Figure 5.3: a) Average apparent-velocities obtained from picked first minimums for point source (orange) and RLFLA (purple) antennas. The first arrival traveltime for point source and the first arrival traveltime with compensation for antenna thickness for RLFLA are indicated by the orange and purple dashed lines, respectively. Calculated apparent-velocities for raypaths without refraction are shown by the green line, whereas the true velocity of the medium is indicated by the blue line. b) Picked first minimum for point source and RLFLA and compensation for antenna-thickness that causes an earlier arrival for RLFLA due to the lower ε_r of the antenna insulation than borehole-fluid.

are equal since no refraction occurs for horizontally traveling waves. Note that the apparent-velocity values are lower than the true velocity due to the presence of the water in the boreholes. We studied the possible effect of the borehole casing by adding a 1 cm plastic casing of $\varepsilon_r = 4$, resulting in an earlier wave arrival due to the lower permittivity of the casing material compared to the subsurface, but still the same trend of increasing apparent velocity with increasing raypath angle is observed (not shown). When investigating the effect of the borehole radius on the apparent-velocity by increasing the radius from 5 cm to 9 cm, an increasing apparent-velocity range from 3.6% to 7% is observed as presented in figure (5.4). These results are consistent with the observations as described by Tronicke and Holliger [154]. It is important to note that the smaller variation range of the simulation results in comparison to the BHRS inversion results presented in figure (5.3) is because we used a homogeneous subsurface, while the presented data were measured in a natural site including natural heterogeneity and measurement/processing errors.

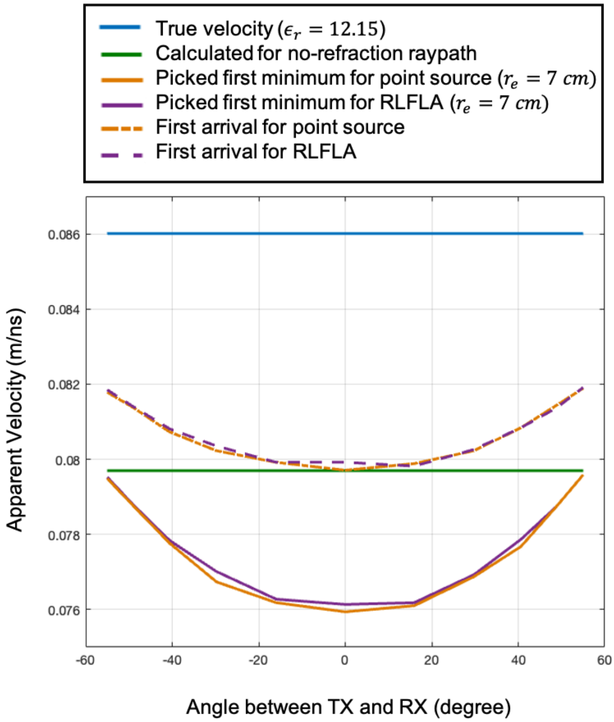

Figure 5.4: Average apparent-velocities obtained from picked first minimums for point source (orange) and RLFLA (purple) antennas in water-filled borehole with effective radius of 0.07 m. The first arrival traveltime for point source and the first arrival traveltime with compensation for antenna thickness for RLFLA are indicated by the orange and purple dashed lines, respectively. Calculated apparent-velocities for ray paths without refraction are shown by the green line, whereas the true velocity of the medium is indicated by the blue line.

Because of symmetry reasons, we show in figure (5.5) zoomed in version of figure (5.3) for positive Tx-Rx raypaths angles. Moreover, we limit our analysis to the point-source arrival due to the results' similarity with the RLFLA.

The simple BFEC angle-dependent apparent-velocities (S, black line) approach the first arrival, whereas the true BFEC apparent velocities (T, red line) are almost overlying the first arrival for point source. These results show that the increase in

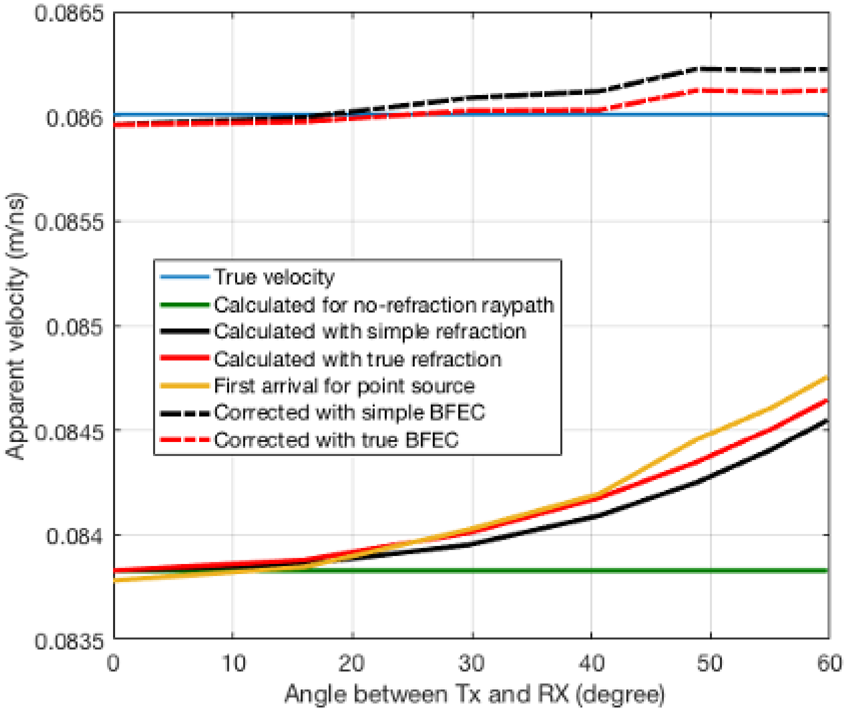

Figure 5.5: Average apparent-velocities of first arrival for point source (orange), assuming no refraction (green) and true velocity (blue) as shown in figure (5.3a) in the dashed rectangle. Calculated simple refraction apparent-velocities (black line) approach the first arrival values, whereas the true refraction apparent-velocities (red line) comes very close to first arrival values of the point source. Applying the simple BFEC and true BFEC returns apparent-velocities indicated by the dashed black and red lines, respectively, that approach the true velocity.

apparent velocity for increasing ray-angle is caused by the wave refraction, when propagating from the water-filled borehole into the subsurface for the Tx antenna and vice versa for the Rx antenna borehole. We apply the BFEC for simplified and true refraction raypaths as discussed in the previous section to obtain the corrected apparent velocity for each Tx- Rx pairs. The simple BFEC results approach the true apparent-velocity values whereas the true BFEC results are almost overlying the true velocity of the medium as indicated by the blue line in figure (5.5). The maximum errors in apparent-velocity reduced from 2.6 % to 0.25 % for the simple BFEC approach for the highest studied raypath angle of 60° whereas the true BFEC has only 0.14% error. These results show that the presence of the water-filled boreholes results in a large decrease in apparent-velocities for zero-angle rays due to a relatively large travelpath through the water-filled borehole, whereas the apparent velocity decrease for high-angle rays is less due to a relatively short travelpath through the water-filled borehole. Note that the increased apparent velocities for increasing ray-angle are closer to the true apparent velocity than the zero-ray apparent velocity. By using the BFEC approach, high-angle raypaths can now reliably be included in ray-based tomography inversion approaches without any artefacts. For seismics, the refraction at the borehole interface is much weaker. Thus, a strong ray-angle dependent apparent-velocity changes are not expected, which was also confirmed by Moret et al. [117].

When solving equation (5.8), we assume to know ε_{subs}. Here, we carry out a sensitivity analysis to study the importance of the assumed ε_{subs} on the performance of the BFEC. We apply the BFEC for a range between -50% to +50% of the true value of ε_{subs}. Figure (5.6) shows the relative error in estimated apparent velocities for the simplified and true BFEC method with different ε_{subs} values. The model errors for the true refraction method is fluctuating between 0.05% to 0.17% depending on ε_{subs}, while the maximum model error is limited to the model error of the simple BFEC which is almost 0.25% for the highest studied angle. A possible solution to better constrain the ε_{subs} ZOP survey could be carried out. ZOPs are easy and straightforward to deploy in crosshole GPR assessment. Thereby obtained averaged 1D permittivity profile is usually in the range required for BFEC and can be used to estimate the permittivity for proposed method.

5.5 Case study 2: realistic synthetic heterogeneous model

To investigate the influence of heterogeneity, we construct a 3D subsurface model of the well-known aquifer system at the test site near the river Thur in Switzerland [42, 35, 80]. This glaciofluvial deposit contains a 7 m gravel layer embedded between 3 m alluvial loam at the top and a low permeable clay aquitard below 10 m depth. At this test site several boreholes with a diameter of 11.4 cm were utilised. The water table is at 4 m depth except during river-flood events. Previous studies by Klotzsche et al. [83, 80] indicated the presence of a high-velocity layer overlying a low-velocity layer between 4 m - 6 m depth, a high velocity layer with low conductivity between 6 m - 8 m, and intermediate values for both parameters below 8 m depth. The boreholes are 5 m apart with 10 m depth and have a diameter of 12 cm. GPR data that were used for the experimental studies were acquired with 11 Tx and 57 Rx antennae using a spatial sampling of 0.5 m and 0.1 m, respectively, in each borehole with a semi-reciprocal approach. All transmitters and receivers were located in the saturated zone. Our subsurface gprMax3D model has dimensions of $7.02m \times 0.9m \times 11.7m$ and a uniform 1cm discretisation including two 6 cm radius water-filled boreholes with

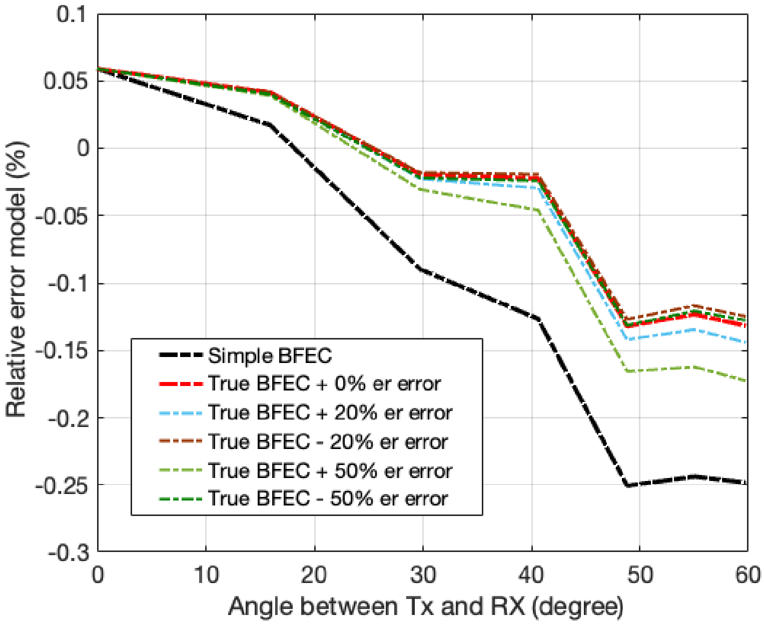

Figure 5.6: Relative model errors in estimated apparent velocity as a function of the raypath angle for the simple BFEC and true BFEC with -50% to 50% error in the ε_{subs}

effective radius of 4cm to be similar as to the Widen setup. Note that many other test sites have smaller diameter boreholes, but we chose this setup to illustrate the efficiencies of the new method. Similar conclusions can be made for smaller diameter boreholes. We use the ε_r and σ values as obtained by Klotzsche et al. [83] as a model to generate 2508 traces using the same Tx and Rx spacing as the experimental studies (look at figure 5.7a). In addition, we build an identical model where there is no borehole present and we the RLFLAs are embedded in the subsurface that which we used to benchmark the performance of the BFEC corrections.

We use a manual picking method to locate the first break of the simulated data (same as for the layered model). We also created a separate subset of the data with a limited maximum angular aperture of 30 degrees. Then, we apply the simple and true BFEC on the data where traveltimes in the boreholes for each Tx and Rx pair are calculated and deducted from the corresponding picked traveltimes. In addition, we relocate the position of each Tx and Rx at the borehole/subsurface interface depending on the simple or true BFEC (look at figure 5.2b). Finally, we invert the picked and corrected picked data using the curved-ray-based traveltime inversion [92, 155] where the domain between the boreholes is discretised to 72×80 cells. We obtain the lowest root-mean-square (RMS) values for a damping and smoothing factor of 1 and a homogeneous starting model with constant ε_r of 18.

ε_r tomograms obtained from the picked data for no borehole presence, water filled boreholes without BFEC, water-filled boreholes with limited angular aperture and without BFEC, water filled boreholes with simple and true BFEC are presented in figure (5.7) where we interpolate the results to the cell-size of the forward model for comparison reasons. As expected, ε_r tomogram of the no borehole data is closest to the reference subsurface model. Almost all ε_r values for the data without BFEC have a larger value than the reference model, whereas the data with the simple and true BFEC approaches the reference model better. The result for the limited angular aperture without BFEC shows a slight deviation from the reference model compared to including all data.This is consistent with the apparent velocity being too low when using uncorrected data.

Figures (5.8a – 5.8e) show the relative model error distributions of the estimated ε_r for no borehole, water-filled boreholes without BFEC, water-filled boreholes with limited angular aperture and without BFEC, water-filled boreholes with simple and true BFEC, respectively. It showed that a better reconstruction when using the simple or true BFEC data, in contrast to the water-filled data without BFEC and the water-filled data with limited angular aperture and without BFEC.

Figures (5.9a and 5.9b) show the mean horizontal and vertical model error, respectively, in estimated ε_r. Both mean vertical and horizontal relative error models are lower for the picked data with simple and true BFEC. The mean relative model error in the entire domain is 4% for no borehole present, 13% for the water-filled borehole without BFEC, 14% for the water-filled borehole with limited angular aperture and without BFEC, 9% for simple BFEC and 8% for true BFEC.

Since the aim of the BFEC is to compensate for the presence of the borehole in the way that results are close to no borehole data, we investigate the effectivity of the BFEC. Therefore, we calculate the model difference percentage of the water-filled boreholes without BFEC, the water-filled boreholes with limited angular aperture and without BFEC, the water-filled boreholes with the simple and true BFEC in comparison to the no borehole present scenario. Note that the relative difference to the no borehole present result is decreased by using the simple and true BFEC (Fig. 5.9b)). The results show that limiting the angular aperture slightly increase the model error, especially in the area that wide-angle paths were discarded such as close to the water-table and in-depth of 10 m (Fig. 5.9b). The mean relative model differences in the entire domain are 5.1%, 5.8%, 3% and 2.4% for water-filled boreholes without BFEC, water-filled boreholes with limited angular aperture and without BFEC, water filled boreholes with simple BFEC and water-filled boreholes with true BFEC, respectively which shows that applying the BFEC compensates for the effect of the borehole presence in the data. Even though applying the BFEC improved the performance of the RBI, to obtain higher resolution images a FWI can be carried out Klotzsche et al. [84]. Note that for applying the FWI to GPR data one critical step is have a good starting model which can be obtained by using our proposed method.

5.6 Conclusion

Detailed 3D EM modelling of crosshole GPR waves including borehole-fluid and RLFLA has been used to investigate the refraction of the EM waves at the borehole interface between water and subsurface as significant contributor to increase of apparent velocities for increasing raypath angles often observed in GPR crosshole data. The performed modelling points out that this phenomenon is majorly influenced by refraction at the borehole interface between water and subsurface. Because of the substantial change in wave velocity in the borehole fluid compared to the wave velocity in the saturated subsurface medium present between the boreholes, the apparent velocity is increasing for increasing ray-angle, whereas the effect is amplified for larger borehole radius and causes larger apparent-velocity differences. Since the velocity changes at the borehole interface are much more substantial for GPR compared to seismic tomograms, the phenomenon is mainly present for GPR and has not been observed for seismic crosshole measurements.

Synthetic studies show that due to the water-filled borehole and the pertaining refraction on the interface between the borehole and the subsurface conventionally obtained velocities are always lower than the real values. We introduce a simple BFEC and a true BFEC method that use an approximated and true refraction at the borehole interfaces between the water and subsurface, respectively. In this way, reliable apparent velocity values are obtained. For a homogeneous model, maximum errors in the apparent velocity of the medium between water-filled boreholes with a radius of 5 cm reduced from 2.6% to 0.25% and 0.14% for the simple BFEC and true BFEC approach, respectively. We verified the performance of the simple BFEC and true BFEC for synthetic heterogeneous crosshole data based on realistic full-waveform inversion results from the river Thur in Switzerland. By applying identical damping and smoothing parameters in curved-ray-based traveltime inversion without BFEC, with the simple BFEC and true BFEC, the subsurface structures were reconstructed with more details for the simple BFEC and true BFEC data and the average relative error model reduced from 13% to 9% and 8% with simple BFEC and true BFEC respectively , despite using an approximation to relocate the Tx and Rx positions at the refraction points. We show that instead of excluding high-angle raypaths from ray-based inversions, commonly used to prevent artefacts, our novel BFEC method enables the use of an increased ray-angle range which results in more-accurate and higher-resolution tomographic inversion results.

The method discussed in this study was validated with two synthetic case studies. Deploying the method to experimental data remains challenging. It requires further investigation as many of the parameters assumed to be known with a high degree of uncertainty are ambiguous and hard to define for experimental data. For example, if in the experimental data mud and/or soil would be present in the borehole, our proposed method would introduce an error to the correction. Possible solutions to address this problem can be to deploy ZOP measurements, perform simple FWI or even taking water samples from boreholes. Besides, the method presented in this study performed sufficiently well as long as the target area's permittivity is significantly lower than borehole fluid. For highly saturated media such as peatlands, further studies are necessary to verify possible applications. Future theoretical development and experimental applications of this method are necessary to understand better this phenomenon and its implication for crosshole GPR inversion.

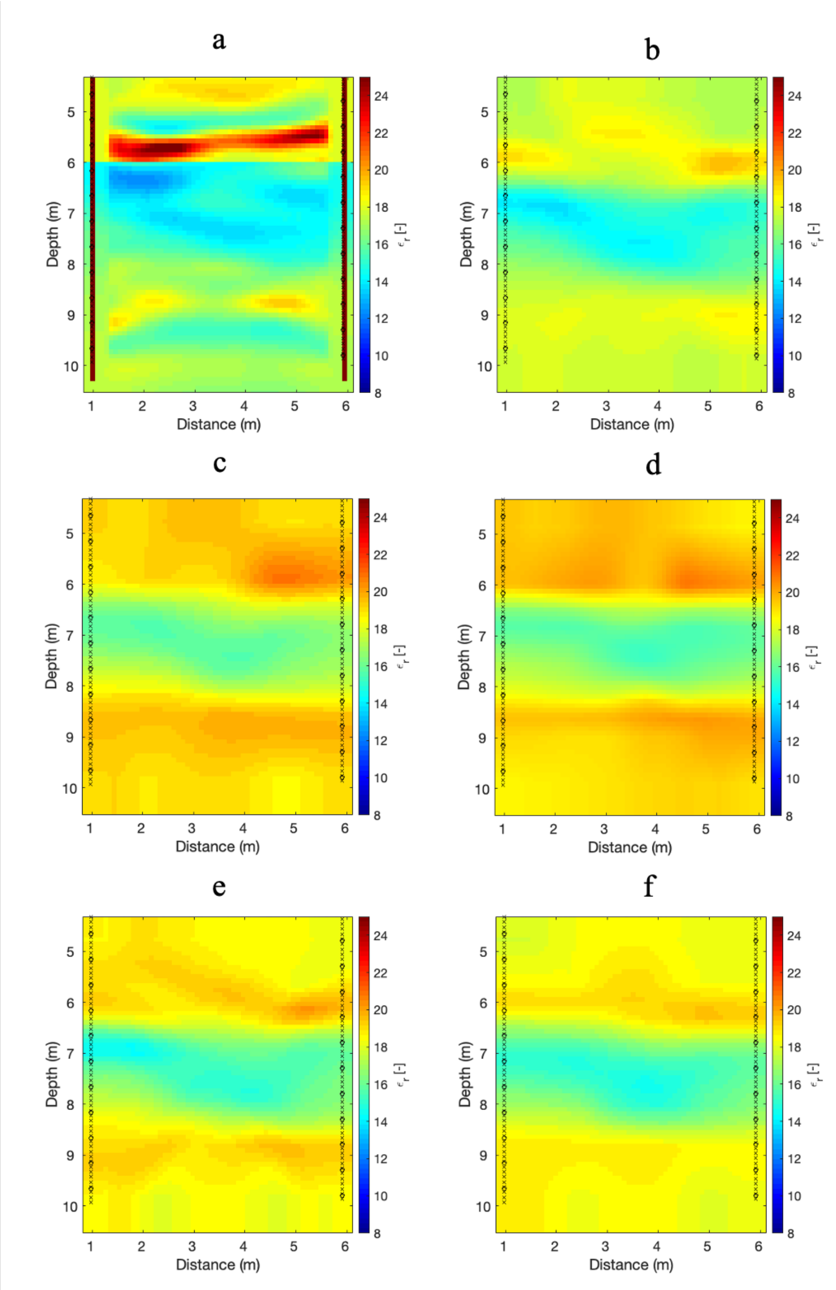

Figure 5.7: ε_r tomogram of a) reference model based on Klotzsche et al. [83] , where the water filled boreholes are indicated by two dark red lines. Tx and Rx positions are indicated by circles and crosses, respectively. Traveltime inversion tomogram for b) no borehole present, c) water-filled borehole without BFEC, d) water-filled borehole without BFEC, and limited aperture, e) water-filled borehole with simple BFEC and f) water-filled borehole with true BFEC. Tx and Rx positions are indicated by circles and crosses, respectively

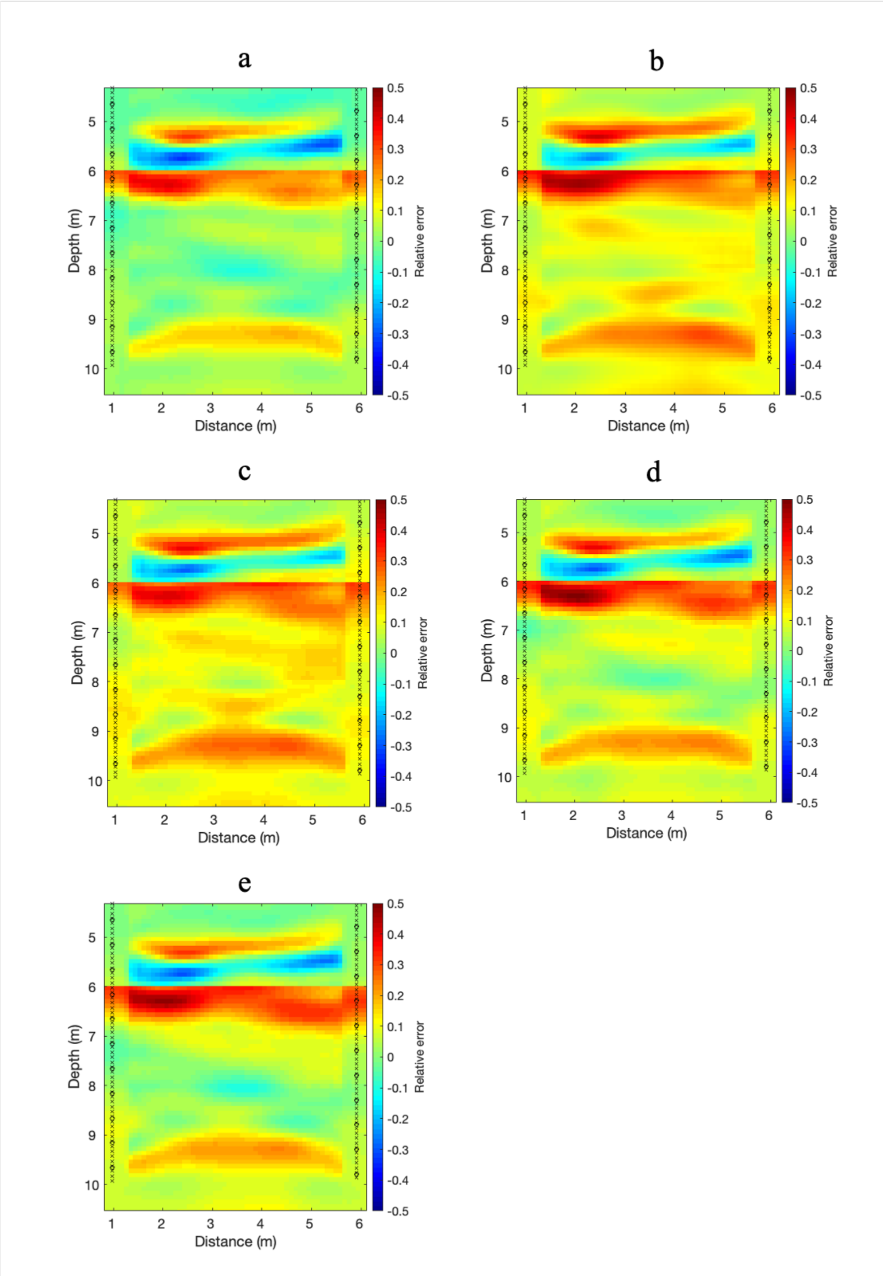

Figure 5.8: Relative model error in estimated ε_r for traveltime inversions for a) no borehole present, b) t water-filled borehole without BFEC c) water-filled borehole without BFEC, and limited aperture, d) water-filled borehole with simple BFEC, and e) water-filled borehole with BFEC. Tx and Rx positions are indicated by circles and crosses, respectively.

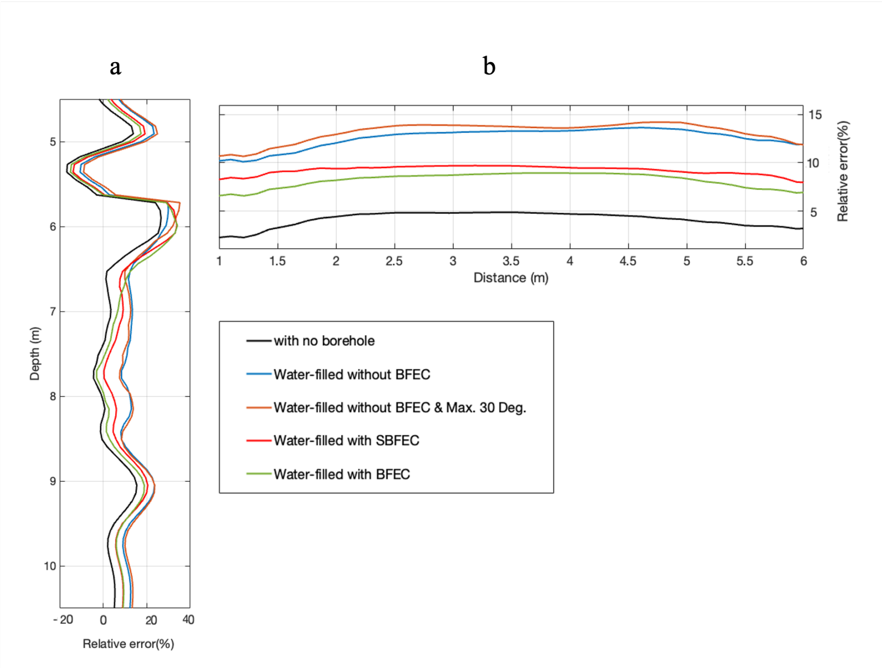

Figure 5.9: a) Mean relative model error in estimated ε_r in vertical cross-section between two boreholes and b) mean relative model error in estimated ε_r in horizontal cross-section between two boreholes (Fig. 5.8a-5.8e).

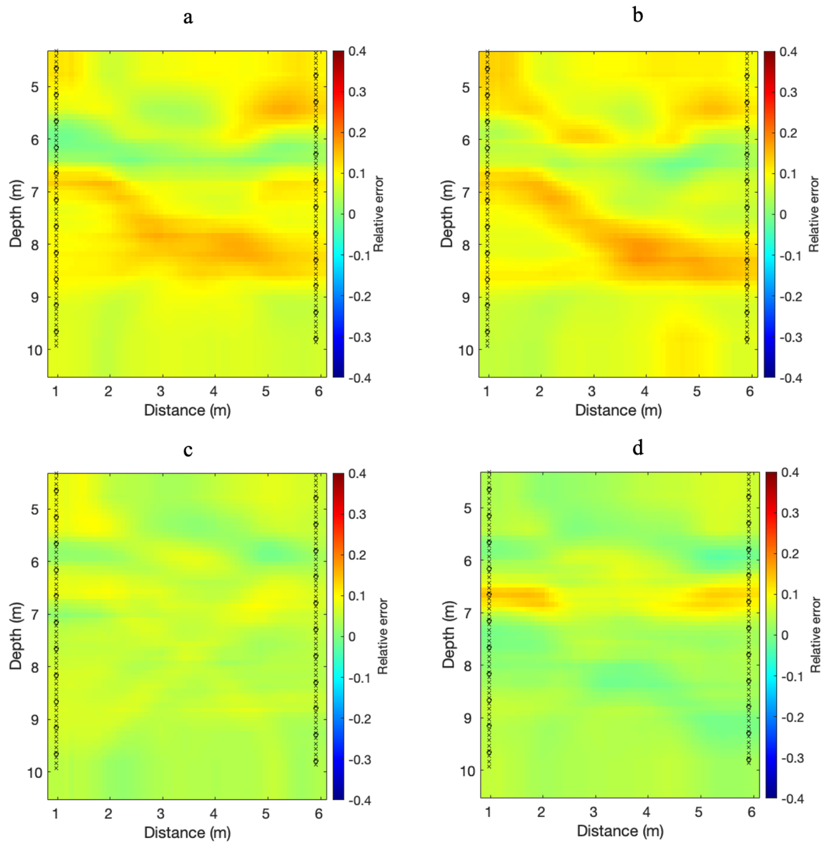

Figure 5.10: Relative difference in estimated ε_r of no borehole case in compare to a) traveltime inversion without BFEC b) traveltime inversion with limited angular aperture and without BFEC c) traveltime inversion with simple BFEC and d) traveltime inversion with true BFEC. Tx and Rx positions are indicated by circles and crosses, respectively.

Chapter 6

Final conclusion and outlook

6.1 Conclusions

Overall, this thesis presents approaches to improve high-resolution geophysical imaging by enhancing the modelling tools and data processing standard. We have investigated the performance gain of using the 3D modelling tools for GPR FWI for hydrogeological site characterisation. Later, we explored the opportunities raised using the 3D modelling tool to build a more detailed model of boreholes and RLFLA. We have utilised these findings by introducing a correction method that increases the consistency of the FWI tomograms. In the following, we will summarise the principal results that obtained in the framework of this thesis, and we will draw some general conclusions.

In chapter (3), we demonstrated that 3D to 2D asymptotic transformation function only works accurately in a simple subsurface cases. At the same time, it fails with complex structures such as high contrast layers that produce overlapping arrivals from several different features. Besides; it fails to map the amplitudes correctly from 3D to 2D traces in non-uniforms media. Our observation shows that applying the 3D to 2D transformation to measured data lowers the resolution of the data by reducing the high-frequency content. Thus, we substitute the 2D forward model with a 3D forward model that doesn't require a 3D to 2D conversion that minimises the associated errors in the crosshole GPR FWI results. The new FWI schema uses gprMax as a complete 3D FDTD modeling kernel, while computing the gradient descent optimisation in a a plan and therefore we named the method 2.5D FWI. We compared the performance of 2D FWI (with 3D to 2D transformation) and the 2.5D FWI for realistic synthetic data. The results for 2.5D FWI showed higher accuracy in estimated ε_r and σ and provided lower AE in tomograms. We observed that time shift caused by 3D to 2D transformation could place the transformed 2D data in less than half-wavelength from measured data, while the same data without the 3D to 2D transformation could be too far from the measured data to converge successfully. Thus, the ε_r starting model of the 2.5D FWI needed some modifications in comparison to the 2D starting model. Moreover, a slight decrease in the dominant frequency of the transformed data was observed, which caused a loss of high-frequency content. Despite the higher resolution and lower error of the 2.5D FWI, it requires significantly more computational resources. Therefore we study the possibility to decrease the intensity by developing more detailed starting models. Thus, we tried to use the 2D FWI intermediate results and updated starting model including the 2D FWI main features as the 2.5D FWI. We reduced the computational costs by more than 40% while maintaining accuracy and resolution by updating the starting model based on the main features obtained by 2D FWI. We verified the novel 2.5D FWI for experimental data by GPR data from the Widen test site in Switzerland. The results showed agreement with previous 2D works, and all the expected structures were identified. As expected, the main improvement was that the σ tomogram shows higher values in zones of higher ε_r and high contrast layers.

In the chapter (4), we investigated the effect of the borehole-fluid and RLFLA on EM wave travel time and angular-dependency of the emitted wavelet. Our detailed 3D simulations and historical data obtained from fairly homogeneous test sites confirmed that borehole-fluid effect and RLFLA angular-dependency have a complex and intertwine affect travel times, wavelet-shape and the amplitude assigned to the EM waves. We introduced borehole-fluid and RLFLA models that we have verified in a series of bench-marking efforts. The new detailed crosshole model including the borehole and the RLFLA overcomes the restrictions of the infinitesimal dipole source assumption and to minimises the associated errors in angular-dependency of the wavelet. Moreover, we have extend the 3D forward model of our 2.5D crosshole GPR FWI that we introduced in chapter (3) to include the borehole-fluid model. We compared the performance of conventional 2D FWI, vanilla 2.5D FWI and the 2.5D FWI with the borehole-fluid integrated for realistic synthetic and it showed the new FWI results have a higher accuracy in estimated ε_r and provided lower AE in tomograms. The better performance of the FWI with borehole-fluid integration is in agreement with our hypothesis as borehole-fluid significantly contributes to travel time of the EM wave that associated with the ε_r of the target medium. In chapter (4), we showed that improvement in the forward kernel has a direct impact on the accuracy of the simulation results.

Chapter (5) investigates the effect of the borehole-fluid and the refraction of the EM waves at the borehole interface between water and subsurface on the apparent velocities. Previous studies indicated a consistent increase in apparent velocity for crosshole GPR data is often observed for increasing. Performed modelling points out that increased apparent velocity is majorly influenced by refraction at the borehole interface between water and subsurface. Due to the substantial change in wave velocity in the borehole fluid compared to the EM wave velocity in the saturated subsurface medium present between the boreholes, the apparent velocity is increasing for increasing raypath angle. The effect of the borehole-fluid is amplified for a larger borehole radius and causes more considerable apparent-velocity differences. The increased apparent velocity is limited to crosshole GPR data in compare to crosshole seismic as the velocity changes at the borehole interface are much more substantial for EM waves than acoustic waves. The conventional method to prevent the inconsistency in the apparent velocity for crosshole GPR data is to limit the angular-aperture that reduce the lateral resolution. We introduce a simple BFEC and a true BFEC method that uses an approximated and true refraction at the borehole interfaces between the water and subsurface, respectively to compensate for the increased apparent velocity. We verified the performance of the new pre-processing method for a homogeneous model. The maximum errors in the apparent velocity obtained for RBI of the medium between water-filled boreholes with a radius of 5 cm reduced from 3.6% to 0.25% and 0.14% for the simple BFEC and true BFEC approach, respectively. In addition, the performance of the simple BFEC and true BFEC is verified for synthetic heterogeneous crosshole data based on realistic FWI results from the river Thur in Switzerland. By applying identical damping and smoothing parameters in curved RBI without BFEC, with the simple BFEC and true BFEC, the subsurface structures were reconstructed with more details for the simple BFEC and true BFEC data and the average relative error model reduced from 13% to 9% and 8% with simple BFEC and true BFEC respectively.Our novel BFEC method achieves a consistent RBI with the use of an increased ray-angle range that results in more-accurate and higher-resolution tomographic inversion results without excluding the high-angle.

In context of this thesis, we demonstrated that detailed FDTD modelling enhances the performance of the crosshole GPR FWI and help us to achieve a better understanding of the physics behind the geophysical phenomena. A detailed 3D FDTD helps to include more details in the simulation that increase the accuracy of the simulated data. Better simulated data can fit the measured data better and reduce the ambiguity of the data. The particular strength of the 2.5D FWI lies in the elimination of asymptotic 3D to 2D transformation. Moreover, a 3D FDTD enables us to incorporate more detailed subsurface, borehole and antenna design. A tool that helped us to quantify the contribution of the realistic borehole-fluid and RLFLA on EM waves travel time and radiation patterns. A new understanding of the borehole-fluid effect was used to improve the 2.5D FWI by integrating the borehole-fluid model that increased the ε_r. Besides, a better understanding of the refraction behaviour for water-filled borehole helped us to formulate the effect in an analytical correction. A method that showed can improve the robustness of the RBI without compromising the consistency of the travel-time inversions.

6.2 Outlook

The main outcome of the approached presented in this thesis relies on the detailed 3D FDTD modelling of the subsurface, boreholes and RLFLA. The next logical steps could be divided into further development of the FDTD and further developments of the models that use this 3D kernel. A 3D FDTD kernel that supports sub-grid meshing will significantly increase the forward model's capability. A dense meshing could be used to model detailed structures such as borehole-fluid, RLFLA with more detailed features, while the computational intensity could be reduced. Moreover, a FDTD forward model that uses GPU acceleration for calculating matrix's application will be giant leap forward. On the other hand, a detailed RLFLA that includes the details of the antenna design could improve the forward model results. Experimental verification of the RLFLA versus the simulation data and calibrating the source wavelet will bring a new level of realism to the modelling of the crosshole GPR.

The crosshole GPR FWI method could be improved by enhancing the linear regression method. Currently, the least square method is used to optimise the cost function. The least-square is a famously non-convex function that is vulnerable to local minimum/maxima. By substation of the least square method with a more complex optimiser such as cross-entropy loss, the initialisation point is less crucial. That means, regardless of the possible shortcomings of the starting models, the cost function will gradually converge to the global maxima/minima. Besides, implementation of the gradient's preconditioning could improve the performance of the 2.5D FWI in the area near the boreholes by reducing the artefacts and the possible blank area. To increase the inversion code's performance, the vectorisation of the parameters will significantly improve the matrix operation as it could theoretically decrease the gradient calculation up to five folds. In addition; and further development of the FDTD that is mentioned above inherently will improve the performance of the FWI as inversion uses the FDTD intensively. The 2.5D FWI is provided with the necessary tool for integrating the crosshole and surface GPR inversion together that is required integration of the surface data and corresponding source wavelet should be integrated into inversion. A dataset acquired with a combination of the surface and crosshole GPR system with a certain depth/ distance and fine sampling is required.

In follow up of the effort to understand and compensate for the effect of the borehole-fluid and RLFLA on crosshole GPR data, more experimental studies are suggested. The effect could be verified versus experimental data for boreholes with different diameters, casing, and different degrees of heterogeneity in the target medium. Besides, the BFEC could be extended to include the air-filled boreholes as pre-processing correction steps. The method also could be verified by more experimental data.

Acknowledgments

Many thanks to all the great people at Jülich whom I had the privilege to meet and work with during my PhD.

Foremost, I want to thank Jan van der Kruk, who initiated this PhD project and trusted me.

I would like to thank Klaus Reicherter, who took the responsibility to supervise me in my PhD in later stages.

I am equally grateful to Anja Klotzsche, who invested so much time into me, and without her help and guidance, this thesis will never have been finished. In addition, I like to thank Harry Vereecken, Craig Warren and Antonis Giannopoulos for all the insight and support.

I would like to thank my doctoral committee, Klaus Reicherter, Harry Vereecken and the committee head Florian Wellmann, for coordinating the session and fascinating discussion.

I am deeply grateful to Martin Schultz at JSC, who generously encouraged me to finish the PhD and provided me with all the support I could ever have wished for.

This work certainly wouldn't have been possible without Jan, Anja, Zhen, Nils, Harry, Craig, Antonis, whose assistance helps in maturing ideas and developing them into the thesis, is highly appreciated.

It was a great pleasure to work and socialise with the other PhD students, post-docs, and colleagues at FZJ (IBG-3, JSC,..). Thanks to Anne, Annelie, Archie, Asta, Bing , Clara, Cosmio, Daniela, Emil, Igor, Inge, Jay, Jess, Jessica, Magdalena, Mahfuj, Mai, Manuella, Markus, Mauricio, Michael, Mirjam, Nazli, Pegah, Scarlet, Sean, Shirin, Tarig, Tao, Theresa, Yi, Ying, Zhen.

A special mention to my parents and Alireza and Parisa, whom I can always count on. Finally, thanks to Helena for sharing everything with me and being the most important person in my life.

Amirpasha Mozaffari

Updated February 14, 2022

Email: a.mozaffari@fz-juelich.de
Phone: +49 172 9541722
Website: amirpasha.me
Twitter: @apmozaffari
Address: Jülich 52428
Linkedin: @amirpasha-mozaffari

Research interests

Data Science, Machine Learning, Geosciences, Exascale machines / HPC, Open science, Data Management

Education

RWTH Aachen University — Aachen, Germany
PhD in Geoscience, — 02.2015 – Present
Towards 3D crosshole GPR FWI
Mentors: Prof. Dr. Klaus Reicherter & Prof. Jan van der Kruk.

Stuttgart University — Stuttgart, Germany
M.Sc in Water Resources Eng.& Man. — 09-2011 – 12.2014
Mentor: Prof. Johan Alexander Huisman

Amirkabir University — Tehran, Iran
BSc. Eng. in Mining Engineering — 09.2007 – 06.2011
Mentor: Prof. Morteza Osanloo

Research experience

Data & Workflow Manager — Jülich, Germany
Jülich Supercomputing Center (JSC) — 05.2019 – Present
Workflow specialist of ML. group in air quality and weather forecast / workflow developer for HPC system /Coordinating multiple computing projects / website development and maintenance

Research Assistant — Jülich, Germany
IBG-3: Agrosphäre — 02.2015 – 05.2019
Numerical and statistical analysis of complex environmental data (Synthetic and Experimental data) / Development and optimization of high-performance numerical modelling algorithms /Developing analytical solutions for short-comings in practical environmental problems

Student assistant — Jülich, Germany
IBG-3: Agrosphäre — 05.2014 – 01.2015
Improving the performance of environmental monitoring systems by numerical modeling and sensitivity analysis

Selected Publications

3-D Electromagnetic Modeling Explains Apparent-Velocity Increase in Crosshole GPR Data-Borehole Fluid Effect Correction Method Enables to Incorporating High-Angle Traveltime Data

Mozaffari, A., Klotzsche, A., Zhou, Z., Vereecken, & H., van der Kruk, J.
IEEE TGRS, 2021.

2.5D crosshole GPR full-waveform inversion with synthetic and measured data
Mozaffari, A., Klotzsche, A., Warren, C., He, G., Giannopoulos, A., Vereecken, & H., van der Kruk, J.
Geophysics, 2020.

Towards 3D full-waveform inversion of crosshole GPR data
Mozaffari, A., Klotzsche, A., He, G., Warren, C., Giannopoulos, A., Vereecken, H., & van der Kruk, J.
International Conference on Ground Penetrating Radar, GPR 2016.

Can deep learning beat numerical weather prediction?
Schultz, M., Betancourt, C., Gong, B., Kleinert, F.,Langguth, M., Leufen, L., **Mozaffari, A.**., & Stadtler, S.
Philosophical Transactions of The Royal Society A Mathematical Physical and Engineering Sciences, 2021.

GPR full-waveform inversion, recent developments, and future opportunities
van der Kruk, J., Liu, T., **Mozaffari, A.**., Gueting, N., Klotzsche, A., Vereecken, H., Warren, C., & Giannopoulos, A.
International Conference on Ground Penetrating Radar, GPR 2018.

Crosshole GPR full-waveform inversion and waveguide amplitude analysis: Recent developments and new challenges
Klotzsche, A., van der Kruk, J., **Mozaffari, A.**., Gueting, N., & Vereecken, H.
International Workshop on Advanced Ground Penetrating Radar, IWAGPR 2015.

Skills

Computer Science
Programming : Python (TF., PyTorch,Xarray, Dask, mpi4py..), Shell, Matlab, C, HTML, git, Containers (Docker, Singularity)
Distributed Sys.: MPI, OpenMP, multithreading

Languages
Farsi/Persian (fluent), English (advanced), German (intermediate)

Talks and tutorials

FAIRness in the multi-services data infrastructure of the Tropospheric Ozone Assessment Report (TOAR) and Artificial Intelligence for Air Quality (IntelliAQ) project 03.2020
Poster presentation in RDA Virtual Plenary 15, Melbourne , Australia

On the use of containers for machine learning and visualization workflows on JUWELS 02.2020
Poster presentation in NIC Symposium 2020, Jülich , Germany

A detailed 3D crosshole GPR Antenna model 09.2017
Presentation in GPR round table, Aachen , Germany

Towards 3D crosshole GPR FWI 12.2016
Poster presentation in AGU fall meeting , San Francisco, United States

2.5D crosshole GPR FWI 05.2016
Presentation in 16th international GPR conference, Hong Kong, Hong Kong

Towards 3D crosshole GPR FWI 02.2016
Presentation in near surface FWI workshop, Zürich , Switzerland

Towards 3D crosshole GPR FWI 09.2015
Presentation in GPR round table, Aachen , Germany

List of Figures

List of Tables

Glossary

ABC absorbing boundary condition

AE average error

BFEC borehole-fluid effect correction

BHRS Boise Hydrological Research Site

CFL Courant–Friedrichs–Lewy

CPU central processing unit

EM electromagnetic

ERT electrical resistivity tomography

FDFD Finite-difference frequency-domain

FDM finite-difference methods

FDTD finite-difference time-domain

FLA finite-length antenna

FWI full-waveform inversion

GPR ground penetrating radar

GPU graphics processing unit

HPC high performance computing

LAE lateral average error

MOG multi-offset gather

MPI message passing interface

PEC perfect electric conductor

PML perfectly matched layer

RBI ray-based inversion

RLA resistive loaded antennas

RLFLA resistive loaded finite-length antennas

RMS root mean square

Rx receiver

S/N signal-to-noise ratio

SDG sustainable development goals

Tx transmitter

UN United Nations

WHO world health organisation

ZOP zero offset profiling

Bibliography

[1] Agudo et al. "Acoustic full-waveform inversion in an elastic world". In: *Geophysics* 83.3 (2018), R257–R271. ISSN: 19422156. DOI: 10.1190/geo2017-0063.1.

[2] Alumbaugh et al. "Estimating moisture contents in the vadose zone using cross-borehole ground penetrating radar: A study of accuracy and repeatability". In: *Water Resources Research* 38.12 (2002), p. 1309. ISSN: 0043-1397. DOI: 10.1029/2001WR000754.

[3] Alumbaugh et al. "Investigating Vadose-zone flow and transport processes using cross borehole GPR and electrical resistivity". In: (2003). URL: https://library.seg.org/doi/pdf/10.1190/1.1817850.

[4] Annan. "Chapter 1 - Electromagnetic Principles of Ground Penetrating Radar". In: *Ground Penetrating Radar Theory and Applications*. Ed. by Jol. Amsterdam: Elsevier, 2009, pp. 1–40. ISBN: 978-0-444-53348-7. DOI: http://dx.doi.org/10.1016/B978-0-444-53348-7.00001-6. URL: http://www.sciencedirect.com/science/article/pii/B9780444533487000016.

[5] Annan. "GPR-History,Trends and Future Developments". In: *Subsurface Sensing Technologies and Applications* 3.4 (2002), pp. 253–270. ISSN: 1566-0184. DOI: 10.1023/A:1020657129590.

[6] Auer et al. "A critical appraisal of asymptotic 3D-to-2D data transformation in full-waveform seismic crosshole tomography". In: *Geophysics* 78.6 (2013), R235–R247. ISSN: 0016-8033. DOI: 10.1190/geo2012-0382.1. URL: http://library.seg.org/doi/abs/10.1190/geo2012-0382.1.

[7] Backus and Gilbert. "Numerical Applications of a Formalism for Geophysical Inverse Problems". In: *Geophysical Journal of the Royal Astronomical Society* 13.1-3 (1967), pp. 247–276. ISSN: 1365246X. DOI: 10.1111/j.1365-246X.1967.tb02159.x.

[8] Bakushinsky and Goncharsky. *Ill-Posed Problems: Theory and Applications*. Springer Science+Business Media Dordrecht, 1994. ISBN: 9789401044479. DOI: 10.1007/978-94-011-1026-6.

[9] Barnaby. "Do nations go to war over water?" In: *Nature* 458.7236 (2009), pp. 282–283. ISSN: 1476-4687. DOI: 10.1038/458282a. URL: https://doi.org/10.1038/458282a.

[10] Bateman. *January 2020 was Earth's hottest January on record*. https://www.noaa.gov/news/january-2020-was-earth-s-hottest-january-on-record. Accessed 26/11/2020. 2020.

[11] Becht et al. "Inversion strategy in crosshole radar tomography using information of data subsets". In: *Geophysics* 69.1 (2004), p. 222. ISSN: 00168033. DOI: 10.1190/1.1649390.

[12] Belina, Ernst, and Holliger. "Inversion of crosshole seismic data in heterogeneous environments: Comparison of waveform and ray-based approaches". In: *Journal of Applied Geophysics* 68.1 (2009), pp. 85–94. ISSN: 09269851. DOI: 10.1016/j.jappgeo.2008.10.012. URL: http://dx.doi.org/10.1016/j.jappgeo.2008.10.012.

[13] Belina et al. "Waveform inversion of crosshole georadar data: Influence of source wavelet variability and the suitability of a single wavelet assumption". In: *IEEE Transactions on Geoscience and Remote Sensing* 50.11 (2012), pp. 4610–4625. ISSN: 01962892. DOI: 10.1109/TGRS.2012.2194154.

[14] Berenger. "A perfectly matched layer for the absorption of electromagnetic waves". In: *ournal of Computational Physics* 114 (1994), pp. 185–200. ISSN: 0021-9991. DOI: 10.1006/jcph.1994.1159. URL: http://portal.acm.org/citation.cfm?id=195266.

[15] Binley et al. "High-resolution characterization of vadose zone dynamics using cross-borehole radar". In: *Water Resources Research* 37.11 (2001), pp. 2639–2652.

[16] Binley et al. "The emergence of hydrogeophysics for improved understanding of subsurface processes over multiple scales". In: *Water Resources Research* 51.6 (2015), pp. 3837–3866. DOI: https://doi.org/10.1002/2015WR017016. eprint: https://agupubs.onlinelibrary.wiley.com/doi/pdf/10.1002/2015WR017016. URL: https://agupubs.onlinelibrary.wiley.com/doi/abs/10.1002/2015WR017016.

[17] Bleibinhaus, Lester, and Hole. "Applying waveform inversion to wide-angle seismic surveys". In: *Tectonophysics* 472.1-4 (2009), pp. 238–248. ISSN: 00401951. DOI: 10.1016/j.tecto.2008.08.023. URL: http://dx.doi.org/10.1016/j.tecto.2008.08.023.

[18] Bleistein. "Two and half dimension in-plane wave propagation". In: *Geophysical Prospecting* 34.5 (1986), pp. 686–703. ISSN: 1365-2478. DOI: 10.1111/j.1365-2478.1986.tb00488.x. URL: http://dx.doi.org/10.1111/j.1365-2478.1986.tb00488.x.

[19] Brantley et al. *Frontiers in Exploration of the Critical Zone: Report of a workshop sponsored by the National Science Foundation (NSF)*. Tech. rep. National Science Foundation (NSF), 2006, 30p. URL: https://www.czen.org/sites/default/files/CZEN%7B%5C_%7DBooklet.pdf.

[20] Brauchler et al. "A field assessment of high-resolution aquifer characterization based on hydraulic travel time and hydraulic attenuation tomography". In: *Water Resources Research* 47 (2011).

[21] Bregman, Bailey, and Chapman. "Ghosts in tomography: The effects of poor angular coverage in {2-D} seismic traveltime inversion". In: *J. Can. Soc. Expl. Geophys.* 25.1 (1989), pp. 7–27.

[22] Brenders and Pratt. "Full waveform tomography for lithospheric imaging: Results from a blind test in a realistic crustal model". In: *Geophysical Journal International* 168.1 (2007), pp. 133–151. ISSN: 0956540X. DOI: 10.1111/j.1365-246X.2006.03156.x.

[23] Brossier, Operto, and Virieux. "Seismic imaging of complex onshore structures by 2D elastic frequency-domain full-waveform inversion". In: *Geophysics* 74.6 (2009), WCC105–WCC118. ISSN: 0016-8033. DOI: 10.1190/1.3215771. URL: http://library.seg.org/doi/10.1190/1.3215771.

[24] Busch, van der Kruk, and Vereecken. "Improved characterization of fine-texture soils using on-ground GPR full-waveform inversion". In: *IEEE Transactions on Geoscience and Remote Sensing* 52.7 (2014), pp. 3947–3958. ISSN: 01962892. DOI: 10.1109/TGRS.2013.2278297.

[25] Butler. "1. What Is Near-Surface Geophysics?" In: *Near-Surface Geophysics* (2005), pp. 1–6. DOI: 10.1190/1.9781560801719.ch1.

[26] Butzer, Kurzmann, and Bohlen. "3D elastic full-waveform inversion of small-scale heterogeneities in transmission geometry". In: *Geophysical Prospecting* 61.6 (2013), pp. 1238–1251. ISSN: 1365-2478. DOI: 10.1111/1365-2478.12065. URL: http://dx.doi.org/10.1111/1365-2478.12065.

[27] Cerveny. *Seismic Ray Theory*. Cambridge University Press, 2001, p. 722. ISBN: 9780521366717. URL: https://books.google.de/books/about/Seismic_Ray_Theory.html?id=LrplpwAACAAJ&redir_esc=y.

[28] Cerveny and Psencik. "Seismic, Ray Theory". In: *Encyclopedia of Solid Earth Geophysics*. Ed. by Gupta. Dordrecht: Springer Netherlands, 2011, pp. 1244–1258. ISBN: 978-90-481-8702-7. DOI: 10.1007/978-90-481-8702-7{_}53. URL: https://doi.org/10.1007/978-90-481-8702-7_53.

[29] Chang and Alumbaugh. "An analysis of the cross-borehole GPR tomography for imaging the development of the infiltrated fluid plume". In: *Journal of Geophysics and Engineering* 8.2 (2011), pp. 294–307. ISSN: 17422132. DOI: 10.1088/1742-2132/8/2/014.

[30] Chang et al. "Cross-borehole ground-penetrating radar for monitoring and imaging solute transport within the vadose zone". In: *Water Resources Research* 42.10 (2006), pp. 1–16. ISSN: 00431397. DOI: 10.1029/2004WR003871.

[31] Chang et al. “The application of ground penetrating radar attenuation tomography in a vadose zone infiltration experiment”. In: *Journal of Contaminant Hydrology* 71.1-4 (2004), pp. 67–87. ISSN: 01697722. DOI: `10.1016/j.jconhyd.2003.09.011`.

[32] Chunduru, Sen, and Stoffa. “Hybrid optimization methods for geophysical inversion”. In: *Geophysics* 62.4 (1997).

[33] Cirpka et al. “Analyzing bank filtration by deconvoluting time series of electric conductivity”. In: *Ground Water* 45.3 (2007), pp. 318–328. ISSN: 0017467X. DOI: `10.1111/j.1745-6584.2006.00293.x`.

[34] Cordua, Hansen, and Mosegaard. “Monte Carlo full waveform inversion of tomographic crosshole data using complex geostatistical a priori information Monte Carlo full waveform inversion”. In: (2010), pp. 4291–4296.

[35] Coscia et al. “3D crosshole ERT for aquifer characterization and monitoring of infiltrating river water”. In: *Geophysics* 76.2 (2011), G49–G59. ISSN: 00168033. DOI: `10.1190/1.3553003`.

[36] Courant, Friedrichs, and Lewy. “Über die partiellen Differenzengleichungen der mathematischen Physik”. In: *Kurt Otto Friedrichs* (1927), pp. 53–95. DOI: `10.1007/978-1-4612-5385-3{\_}7`.

[37] Crase et al. “Robust elastic nonlinear waveform inversion: Application to real data”. In: *Geophysics* 55.5 (1990), pp. 527–538. ISSN: 0016-8033. DOI: `10.1190/1.1442864`. URL: `http://library.seg.org/doi/10.1190/1.1442864`.

[38] Deiana et al. “Calibration of a vadose zone model using water injection monitored by GPR and electrical resistance tomography”. In: *Vadose Zone Journal* 7.1 (2008), pp. 215–226. ISSN: 1539-1663. DOI: `10.2136/vzj2006.0137`.

[39] Dessa and Pascal. “Combined traveltime and frequency-domain seismic waveform inversion: A case study on multi-offset ultrasonic data”. In: *Geophysical Journal International* 154.1 (2003), pp. 117–133. ISSN: 0956540X. DOI: `10.1046/j.1365-246X.2003.01956.x`.

[40] Dickens. “Diffraction tomography for crosswell imaging of nearly layered media”. In: *Geophysics* 59.05 (1994), pp. 694–706. ISSN: 0016-8033. DOI: `10.1190/1.1443627`.

[41] Diem, Vogt, and Hoehn. “Räumliche Charakterisierung der hydraulischen Leitfähigkeit in alluvialen Schotter-Grundwasserleitern: Ein Methodenvergleich”. In: *Bulletin fuer Angewandte Geologie* 15.2 (2010), pp. 53–58. ISSN: 14206846. DOI: `10.1007/s00767-010-0153-6`.

[42] Doetsch et al. “The borehole-fluid effect in electrical resistivity imaging”. In: *Geophysics* 75.4 (2010), pp. 107–114. URL: `http://library.seg.org/doi/abs/10.1190/1.3467824`.

[43] Doetsch et al. “Zonation for 3D aquifer characterization based on joint inversions of multimethod crosshole geophysical data”. In: *Geophysics* 75.6 (2010), pp. 53–64. ISSN: 00168033. DOI: 10.1190/1.3496476.

[44] Dorn et al. “Single-hole GPR reflection imaging of solute transport in a granitic aquifer”. In: *Geophysical Research Letters* 38.8 (2011), pp. 1–5. ISSN: 00948276. DOI: 10.1029/2011GL047152.

[45] Englert. “Measurement , Estimation and Modelling of Groundwater Flow Velocity at Krauthausen Test Site”. In: (2003), p. 109.

[46] Ernst et al. “Application of a new 2D time-domain full-waveform inversion scheme to crosshole radar data”. In: *Geophysics* 72.5 (2007), J53. ISSN: 00168033. DOI: 10.1190/1.2761848.

[47] Ernst et al. “Full-Waveform Inversion of Crosshole Radar Data Based on 2-D Finite-Difference Time-Domain Solutions of Maxwell ’ s Equations”. In: *Ieee* 45.9 (2007), pp. 2807–2828.

[48] Ernst et al. “Realistic FDTD modelling of borehole georadar antenna radiation: Methodolgy and application”. In: *Near Surface Geophysics* 4.1 (2006), pp. 19–30. ISSN: 15694445. DOI: 10.3997/1873-0604.2005028.

[49] Fichtner. “Full Seismic Waveform Modelling and Inversion”. In: *Advances* (2011), pp. 83–88. ISSN: 1098-6596. DOI: 10.1007/978-3-642-15807-0. URL: http://www.springerlink.com/index/10.1007/978-3-642-15807-0.

[50] Giannakis, Giannopoulos, and Warren. “Realistic FDTD GPR antenna models optimised using a novel linear / non-linear Full Waveform Inversion”. In: *IEEE Transactions on Geoscience and Remote Sensing* PP (2018), pp. 1–11. ISSN: 0196-2892. DOI: 10.1109/TGRS.2018.2869027.

[51] Giannopoulos. *GprMax2D/3D User’s Manual*. Tech. rep. 2005, p. 78. URL: gprmax.org.

[52] Giannopoulos. “Modelling ground penetrating radar by GprMax”. In: *Construction and Building Materials* 19.10 (2005), pp. 755–762. ISSN: 09500618. DOI: 10.1016/j.conbuildmat.2005.06.007.

[53] Gilson, Redman, and Annan. “Near Surface Applications Of Borehole Radar”. In: *9th EEGS Symposium on the Application of Geophysics to Engineering and Environmental Problems*. Keystone, Colorado, USA: European Association of Geoscientists & Engineers, 1996. DOI: https://doi.org/10.3997/2214-4609-pdb.205.1996{_}060. URL: https://www.earthdoc.org/content/papers/10.3997/2214-4609-pdb.205.1996_060.

[54] Givetash. *Australian wildfires declared among the ’worst wildlife disasters in modern history’*. https://www.nbcnews.com/news/world/australian-wildfires-declared-among-worst-wildlife-disasters-modern-history-n1235071. Accessed 26/11/2020. 2020.

[55] Glassner. *An Introduction to Ray Tracing*. Morgan Kaufmann, 1989, p. 368. ISBN: 9780080499055.

[56] Gleick. "Water and Conflict: Fresh Water Resources and International Security". In: *International Security* 18.1 (1993), pp. 79–112. ISSN: 01622889, 15314804. URL: http://www.jstor.org/stable/2539033.

[57] Goodfellow, Bengio, and Courville. *Deep Learning*. http://www.deeplearningbook.org. MIT Press, 2016.

[58] Greenhalgh et al. "Numerical study of seismic scattering and waveguide excitation in faulted coal seams". In: *Geophysical Prospecting* 55.2 (2007), pp. 185–198. ISSN: 00168025. DOI: 10.1111/j.1365-2478.2007.00604.x.

[59] Gueting et al. "High resolution aquifer characterization using crosshole GPR full-waveform tomography: Comparison with direct-push and tracer test data". In: *Water Resources Research* 53.1 (2017), pp. 49–72. ISSN: 1944-7973. DOI: 10.1002/2016WR019498. URL: http://dx.doi.org/10.1002/2016WR019498.

[60] Hagness and Taflove. "Finite-Difference Time-Domain (FDTD) Computational Electrodynamics Simulations of Microlaser Cavities in One and Two Spatial Dimensions". In: *Computational Electromagnetics and Its Applications*. Ed. by Campbell, Nicolaides, and Salas. Dordrecht: Springer Netherlands, 1997, pp. 229–251. ISBN: 978-94-011-5584-7. DOI: 10.1007/978-94-011-5584-7{_}11. URL: https://doi.org/10.1007/978-94-011-5584-7_11.

[61] Hanafy and al Hagrey. "Ground-penetrating radar tomography for soil-moisture heterogeneity". In: *Geophysics* 71.1 (2006), K9. ISSN: 00168033. DOI: 10.1190/1.2159052.

[62] Hansen et al. "Accounting for imperfect forward modeling in geophysical inverse problems — Exemplified for crosshole tomography". In: *Geophysics* 79.3 (2014), H1–H21. ISSN: 0016-8033. DOI: 10.1190/geo2013-0215.1. URL: http://library.seg.org/doi/10.1190/geo2013-0215.1.

[63] Hardage. *Crosswell seismology & reverse VSP*. Geophysical Press, 1992, p. 304. ISBN: 094663145X, 9780946631452.

[64] He, Pan, and Tanaka. "The short-term impacts of COVID-19 lockdown on urban air pollution in China". In: *Nature Sustainability* (2020). ISSN: 2398-9629. DOI: 10.1038/s41893-020-0581-y. URL: https://doi.org/10.1038/s41893-020-0581-y.

[65] Hollender, Tillard, and Corin. "Multifold borehole radar acquisition and processing". In: *Geophysical Prospecting* 47.6 (1999), pp. 1077–1090. ISSN: 00168025. DOI: 10.1046/j.1365-2478.1999.00166.x.

[66] Holliger and Maurer. “Effects of stochastic heterogeneity on ray-based tomographic inversion of crosshole georadar amplitude data”. In: *Journal of Applied Geophysics* 56.3 (2004), pp. 177–193. ISSN: 09269851. DOI: 10.1016/j.jappgeo.2004.06.001. URL: http://linkinghub.elsevier.com/retrieve/pii/S0926985104000515.

[67] Holliger, Musil, and Maurer. “Ray-based amplitude tomography for crosshole georadar data: A numerical assessment”. In: *Journal of Applied Geophysics* 47.3-4 (2001), pp. 285–298. ISSN: 09269851. DOI: 10.1016/S0926-9851(01)00072-6.

[68] Holliger et al. “Realistic modeling of surface georadar antenna systems”. In: *2003 SEG Annual Meeting* (2003), pp. 14–16.

[69] Hubbard, Rubin, and Majer. “Ground-penetrating-radar-assisted saturation and permeability estimation in bimodal systems”. In: *Water Resources Research* 33.5 (1997), pp. 971–990. ISSN: 00431397. DOI: 10.1029/96WR03979.

[70] Hubbard et al. “Hydrogeological characterization of the South Oyster Bacterial Transport Site using geophysical data”. In: *Water Resources Research* 37.10 (2001), pp. 2431–2456.

[71] Hunziker, Laloy, and Linde. “Inference of multi-Gaussian relative permittivity fields by probabilistic inversion of crosshole ground-penetrating radar data”. In: *Geophysics* 82.5 (2017), H25–H40. ISSN: 0016-8033. DOI: 10.1190/geo2016-0347.1. URL: http://library.seg.org/doi/10.1190/geo2016-0347.1.

[72] Irving and Knight. “Effect of antennas on velocity estimates obtained from crosshole GPR data”. In: *Geophysics* 70.5 (2005), K39–K42. ISSN: 00168033. DOI: 10.1190/1.2049349.

[73] Irving, Knoll, and Knight. “Improving crosshole radar velocity tomograms: A new approach to incorporating high-angle traveltime data”. In: *Geophysics* 72.4 (2007), J31–J41. ISSN: 0016-8033. DOI: 10.1190/1.2742813. URL: http://library.seg.org/doi/abs/10.1190/1.2742813.

[74] Johnson. *Notes on Perfectly Matched Layers (PMLs)*. Tech. rep. 4. 2010, pp. 1–18.

[75] Kabanikhin. “Definitions and examples of inverse and ill-posed problems”. In: *Journal of Inverse and Ill-Posed Problems* 16.4 (2008), pp. 317–357. ISSN: 09280219. DOI: 10.1515/JIIP.2008.019.

[76] Kanda. “A Relatively Short Cylindrical Broadband Antenna with Tapered Resistive Loading for Picosecond”. In: 3 (1978), pp. 439–447.

[77] Kemna et al. “Imaging and characterisation of subsurface solute transport using electrical resistivity tomography (ERT) and equivalent transport models”. In: *Journal of Hydrology* 267.3-4 (2002), pp. 125–146.

[78] Keskinen et al. "Full-waveform inversion of Crosshole GPR data: Implications for porosity estimation in chalk". In: *Journal of Applied Geophysics* 140 (2017), pp. 102–116. ISSN: 09269851. DOI: 10.1016/j.jappgeo.2017.01.001. URL: http://dx.doi.org/10.1016/j.jappgeo.2017.01.001.

[79] Klotzsche, Vereecken, and van der Kruk. "Review of Crosshole GPR Full-waveform Inversion of Experimental Data: Recent Developments, Challenges and Pitfalls". In: *Geophysics* (2019).

[80] Klotzsche et al. "3-D characterization of high-permeability zones in a gravel aquifer using 2-D crosshole GPR full-waveform inversion and waveguide detection". In: *Geophysical Journal International* Vol.195.No.2 (2013), pp. 932–944. ISSN: 0956-540X. DOI: 10.1093/gji/ggt275. URL: http://gji.oxfordjournals.org/cgi/doi/10.1093/gji/ggt275.

[81] Klotzsche et al. "Characterizing a Gravel Aquifer by Full-waveform Inversion of Crosshole Ground Penetrating Radar Data". In: 12.May (2010), p. 7742.

[82] Klotzsche et al. "Crosshole GPR full-waveform inversion and waveguide amplitude analysis: Recent developments and new challenges". In: *2015 8th International Workshop on Advanced Ground Penetrating Radar, IWAGPR 2015* (2015), pp. 1–6. DOI: 10.1109/IWAGPR.2015.7292647.

[83] Klotzsche et al. "Crosshole GPR full-waveform inversion of waveguides acting as preferential flow paths within aquifer systems". In: *Geophysics* 77.4 (2012), H57. ISSN: 00168033. DOI: 10.1190/geo2011-0458.1. URL: http://link.aip.org/link/GPYSA7/v77/i4/pH57/s1&Agg=doi%5Cnhttp://library.seg.org/doi/abs/10.1190/geo2011-0458.1.

[84] Klotzsche et al. "Detection of spatially limited high-porosity layers using crosshole GPR signal analysis and full-waveform inversion". In: *Water Resources Research* (2014), pp. 6966–6985. DOI: 10.1002/2013WR015177.Received. URL: http://onlinelibrary.wiley.com/doi/10.1002/2013WR015177/full.

[85] Klotzsche et al. "Full-waveform inversion of cross-hole ground-penetrating radar data to characterize a gravel aquifer close to the Thur River, Switzerland". In: *Near Surface Geophysics* 8.6 (2010), pp. 635–649. ISSN: 15694445. DOI: 10.3997/1873-0604.2010054.

[86] Klotzsche et al. "Measuring Soil Water Content with Ground Penetrating Radar: A Decade of Progress". English. In: *Vadose Zone Journal* 17 (2018). DOI: 10.2136/vzj2018.03.0052. URL: http://dx.doi.org/10.2136/vzj2018.03.0052.

[87] Klysz et al. "Simulation of direct wave propagation by numerical FDTD for a GPR coupled antenna". In: *NDT & E International* 39.4 (2006), pp. 338–347. ISSN: 0963-8695. DOI: https://doi.org/10.1016/j.ndteint.2005.10.001. URL: http://www.sciencedirect.com/science/article/pii/S0963869505001490.

[88] Krause and Thörnig. “JURECA: General-purpose supercomputer at Jülich Supercomputing Centre”. In: *Journal of large-scale research facilities JLSRF* 2 (2016), A62. ISSN: 2364-091X. DOI: 10.17815/jlsrf-2-121. URL: http://jlsrf.org/index.php/lsf/article/view/121.

[89] Kuroda, Takeuchi, and Kim. “Full-waveform inversion algorithm for interpreting crosshole radar data: A theoretical approach”. In: *Geosciences Journal* 11.3 (2007), pp. 211–217. ISSN: 12264806. DOI: 10.1007/BF02913934.

[90] Lambot et al. “Full-waveform modeling of ground-coupled GPR antennas for wave propagation in multilayered media: The problem solved ?” In: *Proceedings of the 13th Internarional Conference on Ground Penetrating Radar, GPR 2010* (2010), pp. 6–10. DOI: 10.1109/ICGPR.2010.5550146.

[91] Lampe and Holliger. “Resistively loaded antennas for ground-penetrating radar: A modeling approach”. In: *Geophysics* 70.3 (2005), K23–K32. ISSN: 0016-8033. DOI: 10.1190/1.1926574. URL: http://library.seg.org/doi/abs/10.1190/1.1926574.

[92] Lanz, Maurer, and Green. “Refraction tomography over a buried waste disposal site”. In: *Geophysics* 63.4 (1998), pp. 1414–1433. ISSN: 0016-8033. DOI: 10.1190/1.1444443. URL: https://library.seg.org/doi/10.1190/1.1444443.

[93] Lassen et al. “Monitoring CO2 gas-phase migration in a shallow sand aquifer using cross-borehole ground penetrating radar”. In: *International Journal of Greenhouse Gas Control* 37 (2015), pp. 287–298. ISSN: 17505836. DOI: 10.1016/j.ijggc.2015.03.030. URL: http://dx.doi.org/10.1016/j.ijggc.2015.03.030.

[94] Lavoué. “2D Full waveform inversion of ground penetrating radar data”. PhD thesis. 2014.

[95] Lavoué et al. “2D full waveform inversion of GPR surface data: Permittivity and conductivity imaging”. In: *IWAGPR 2013 - Proceedings of the 2013 7th International Workshop on Advanced Ground Penetrating Radar* 1.1 (2013). DOI: 10.1109/IWAGPR.2013.6601521.

[96] Lestari, Yarovoy, and Ligthart. “RC-loaded bow-tie antenna for improved pulse radiation”. In: *IEEE Transactions on Antennas and Propagation* 52.10 (2004), pp. 2555–2563. ISSN: 0018926X. DOI: 10.1109/TAP.2004.834444.

[97] Niklas Linde, Stefan Finsterle, and Susan Hubbard. “Inversion of tracer test data using tomographic constraints”. In: *Water Resources Research* 42.4 (2006), pp. 1–15. ISSN: 00431397. DOI: 10.1029/2004WR003806.

[98] Linde et al. “Improved hydrogeophysical characterization using joint inversion of cross-hole electrical resistance and ground-penetrating radar traveltime data”. In: *Water Resources Research* 42.12 (2006), pp. 1–16. ISSN: 00431397. DOI: 10.1029/2006WR005131.

[99] Linde et al. “Joint inversion of crosshole radar and seismic traveltimes acquired at the South Oyster Bacterial Transport Site”. In: *Geophysics* 73.4 (2008), G29–G37.

[100] Lindow, Richter, and Petzold. “Bodenradar”. In: *Handbuch zur Erkundung des Untergrundes von Deponien und Altlasten Band 3: Geophysik*. Ed. by Klaus Knödel, Heinrich Krummel, and Gerhard Lange. Berlin: Springer Verlag Berlin, Heidelberg, 1997. Chap. Chapter 6, pp. 369–404. ISBN: 978-3-662-07723-8. URL: https://www.springer.com/de/book/9783662077238.

[101] Liu, Su, and Mao. “FDTD analysis of ground-penetrating radar antennas with shields and absorbers”. In: *Frontiers of Electrical and Electronic Engineering in China* 3.1 (2008), pp. 90–95. ISSN: 1673-3584. DOI: 10.1007/s11460-008-0023-5. URL: https://doi.org/10.1007/s11460-008-0023-5.

[102] Lochbühler et al. “Conditioning of Multiple-Point Statistics Facies Simulations to Tomographic Images”. In: *Mathematical Geosciences* 46.5 (2014), pp. 625–645. ISSN: 18748953. DOI: 10.1007/s11004-013-9484-z.

[103] Looms et al. “Geostatistical inference using crosshole ground-penetrating radar”. In: *Geophysics* 75.6 (2010), J29–J41. ISSN: 00168033. DOI: 10.1190/1.3496001.

[104] Looms et al. “Mapping sand layers in clayey till using crosshole ground-penetrating radar”. In: *Geophysics* 83.1 (2018), A21–A26. ISSN: 0016-8033. DOI: 10.1190/geo2017-0297.1. URL: https://library.seg.org/doi/10.1190/geo2017-0297.1.

[105] Looms et al. “Monitoring Unsaturated Flow and Transport Using Cross-Borehole Geophysical Methods”. In: *Vadose Zone Journal* 7.1 (2008), p. 227. ISSN: 1539-1663. DOI: 10.2136/vzj2006.0129. URL: https://www.soils.org/publications/vzj/abstracts/7/1/227.

[106] Susanta Mahato, Swades Pal, and Krishna Gopal Ghosh. “Effect of lockdown amid COVID-19 pandemic on air quality of the megacity Delhi, India”. In: *Science of The Total Environment* 730 (2020), p. 139086. ISSN: 0048-9697. DOI: https://doi.org/10.1016/j.scitotenv.2020.139086. URL: http://www.sciencedirect.com/science/article/pii/S0048969720326036.

[107] Maurer and Musil. “Effects and removal of systematic errors in crosshole georadar attenuation tomography”. In: *Journal of Applied Geophysics* 55.3-4 (2004), pp. 261–270. ISSN: 09269851. DOI: 10.1016/j.jappgeo.2004.02.003.

[108] Maxwell. *A Treatise On Electricity and Magnetism*. 2nd. New York, 1954, p. 532. ISBN: 486-60637-6.

[109] McGlashan et al. “Field GPR monitoring of biostimulation in saturated porous media”. In: *Journal of Applied Geophysics* 78 (2012), pp. 102–112. ISSN: 09269851. DOI: 10.1016/j.jappgeo.2011.08.006.

[110] Meles et al. “A new vector waveform inversion algorithm for simultaneous updating of conductivity and permittivity parameters from combination crosshole/borehole-to- surface GPR data”. In: *IEEE Transactions on Geoscience and Remote Sensing* 48.9 (2010), pp. 3391–3407. ISSN: 01962892. DOI: 10.1109/TGRS.2010.2046670.

[111] Meles et al. “Tackling the non-linearity problem in GPR waveform inversion”. In: *Proceedings of the 13th Internarional Conference on Ground Penetrating Radar, GPR 2010* (2010), pp. 6–11. DOI: 10.1109/ICGPR.2010.5550233.

[112] Menard. *Logistic Regression: From Introductory to Advanced Concepts and Applications*. Thousand Oaks, California, 2010. DOI: 10.4135/9781483348964. URL: https://methods.sagepub.com/book/logistic-regression-from-introductory-to-advanced-concepts-and-applications.

[113] Menke. “The resolving power of cross-borehole tomography”. In: *Geophysical research letters* 11 (1984), pp. 105–108.

[114] Miksat, Müller, and Wenzel. “Simulating three-dimensional seismograms in 2.5-dimensional structures by combining two-dimensional finite difference modelling and ray tracing”. In: *Geophysical Journal International* 174.1 (2008), pp. 309–315. ISSN: 0956540X. DOI: 10.1111/j.1365-246X.2008.03800.x.

[115] Mohammadian, Shankar, and Hall. “Computation of electromagnetic scattering and radiation using a time-domain finite-volume discretization procedure”. In: *Computer Physics Communications* 68.1-3 (1991), pp. 175–196. ISSN: 00104655. DOI: 10.1016/0010-4655(91)90199-U.

[116] Monorchio et al. “A hybrid time-domain technique that combines the finite element, finite difference and method of moment techniques to solve complex electromagnetic problems”. In: *IEEE Transactions on Antennas and Propagation* 52.10 (2004), pp. 2666–2674. ISSN: 0018926X. DOI: 10.1109/TAP.2004.834431.

[117] Moret et al. “Investigating the stratigraphy of an alluvial aquifer using crosswell seismic traveltime tomography”. In: *Geophysics* 71.3 (2006), B63–B73. ISSN: 0016-8033. DOI: 10.1190/1.2195487. URL: http://library.seg.org/doi/10.1190/1.2195487.

[118] Morton and Mayers. *Numerical Solution of Partial Differential Equations*. 2nd editio. Cambridge University Press, 2005. ISBN: 9780511812248. DOI: https://doi.org/10.1017/CBO9780511812248. URL: https://www.cambridge.org/core/books/numerical-solution-of-partial-differential-equations/EB8E5037C4A49F78D91C0AF7EE4CC7FA#fndtn-information.

[119] Mozaffari et al. “2.5D crosshole GPR full-waveform inversion with synthetic and measured data”. In: *GEOPHYSICS* 85.4 (2020), H71–H82. ISSN: 0016-8033. DOI: 10.1190/geo2019-0600.1. URL: https://doi.org/10.1190/geo2019-0600.1.

[120] Mozaffari et al. "Towards 3D full-waveform inversion of crosshole GPR data". In: *GPR conference 2016*. Hong Kong, 2016, pp. 5–8.

[121] Mulder, Perkins, and Van De Rijzen. "2D Acoustic Full Waveform Inversion of a Land Seismic Line". In: *Eage* June 2010 (2010), pp. 14–17.

[122] National Research Council. *Basic Research Opportunities in Earth Science*. Washington, DC: The National Academies Press, 2001. ISBN: 978-0-309-07133-8. DOI: 10.17226/9981. URL: https://www.nap.edu/catalog/9981/basic-research-opportunities-in-earth-science.

[123] Navarro et al. "Application of PML superabsorbing boundary condition to non-orthogonal FDTD method". In: *Electronics Letters* 30.20 (1994), pp. 1654–1656. ISSN: 0013-5194. DOI: 10.1049/el:19941139. URL: https://digital-library.theiet.org/content/journals/10.1049/el_19941139.

[124] Ng, Katanforoosh, and Mourri. *Neural Networks and Deep Learning by DeepLearning.AI*. https://www.coursera.org/learn/neural-networks-deep-learning/home/info. Accessed 19/11/2020. 2018.

[125] Oberröhrmann et al. "Optimization of acquisition setup for cross-hole GPR full-waveform inversion using checkerboard analysis". In: *Near Surface Geophysics* 11.2 (2013), pp. 197–209. ISSN: 15694445. DOI: 10.3997/1873-0604.2012045.

[126] Olver. *Introduction to Partial Differential Equations*. 1st ed. Vol. 1. Undergraduate Texts in Mathematics. Springer International Publishing, 2014, p. 652. ISBN: 978-3-319-02098-3. DOI: 10.1007/978-3-319-02099-0. URL: http://link.springer.com/10.1007/978-3-319-02099-0.

[127] Overshootday.org. *Past Earth Overshoot Days*. https://www.overshootday.org/newsroom/past-earth-overshoot-days/. Accessed 26/11/2020. 2020.

[128] Peterson. "Pre-inversion corrections and analysis of radar tomographic data". In: *Journal of Environmental and Engineering Geophysics* 6.1 (2001), pp. 1–18. ISSN: 1083-1363.

[129] Pierre-Louis and Schwartz. *Australian wildfires declared among the 'worst wildlife disasters in modern history'*. https://www.nytimes.com/article/why-does-california-have-wildfires.html. Accessed 26/11/2020. 2020.

[130] Pinchover and Rubinstein. *An Introduction to Partial Differential Equations*. Cambridge University Press, 2005. ISBN: 9780511801228. DOI: 10.1017/CBO9780511801228. URL: https://www.cambridge.org/core/product/identifier/9780511801228/type/book.

[131] Pirot et al. "Probabilistic inversion with graph cuts: Application to the Boise Hydrogeophysical Research Site". In: *Water Resources Research* 53.2 (2017), pp. 1231–1250. ISSN: 19447973. DOI: 10.1002/2016WR019347.

[132] Popper. *The Logic of Scientific Discovery*. 1st. Hutchinson, London: Hutchinson & Co., 1955. ISBN: 978-0415278447.

[133] Pratt. "Seismic waveform inversion in the frequency domain, Part 1: Theory and verification in a physical scale model". In: *Geophysics* 64.3 (1999), pp. 888–901. ISSN: 0016-8033. DOI: `10.1190/1.1444597`. URL: `http://library.seg.org/doi/10.1190/1.1444597`.

[134] Pratt, Shin, and Hicks. "Gauss-Newton and full Newton methods in frequency-space seismic waveform inversion". In: *Geophysical Journal International* 133.2 (1998), pp. 341–362. ISSN: 0956540X. DOI: `10.1046/j.1365-246X.1998.00498.x`. URL: `http://doi.wiley.com/10.1046/j.1365-246X.1998.00498.x`.

[135] Rabbel. "Seismic methods". In: *Groundwater Geophysics: A Tool for Hydrogeology*. Ed. by Kirsch. Berlin, Heidelberg: Springer Berlin Heidelberg, 2006, pp. 23–83. ISBN: 978-3-540-29387-3. DOI: `10.1007/3-540-29387-6_2`. URL: `https://doi.org/10.1007/3-540-29387-6_2`.

[136] Rector and Washbourne. "Characterization of resolution and uniqueness in crosswell direct-arrival traveltime tomography using the Fourier projection slice theorem". In: 59.11 (1994), pp. 1642–1649.

[137] Rietsch. "The maximum entropy approach to inverse problems". In: *Geophysics* 42 (1977), pp. 489–506.

[138] Rubin and Hubbard. *Hydrogerphysics*. Springer Netherlands, 2005, p. 527. ISBN: 9781402031014. DOI: `10.1007/1-4020-3102-5`. URL: `https://www.springer.com/gp/book/9781402031014`.

[139] Rumelhart, Hinton, and Williams. "Learning representations by back-propagating errors". In: *Nature* 323.6088 (1986), pp. 533–536. ISSN: 1476-4687. DOI: `10.1038/323533a0`. URL: `https://doi.org/10.1038/323533a0`.

[140] Schmalzbauer and Visbeck. *The Contribution of Science in Implementing the Sustainable Development Goals*. February. 2016, p. 52. ISBN: 9783981306859. URL: `www.dkn-future-earth.org`.

[141] Sirgue, Etgen, and Albertin. "3D frequency domain waveform inversion using time domain finite difference methods". In: *70th EAGE Conference & Exhibition* 2008 (2008), pp. 9–12. URL: `http://www.earthdoc.org/publication/publicationdetails/?publication=9830`.

[142] Slater et al. "Electrical imaging of saline tracer migration for the investigation of unsaturated zone transport mechanisms". In: *Hydrology and Earth ...* (1997). URL: `http://www.hydrol-earth-syst-sci.net/1/291/1997/`.

[143] Slater et al. "Use of electrical imaging and distributed temperature sensing methods to characterize surface water-groundwater exchange regulating uranium transport at the Hanford 300 Area, Washington". In: *Water Resources Research* 46 (2010).

[144] Song and Williamson. "Frequency-domain acoustic-wave modeling and inversion of crosshole data: Part I—2.5-D modeling method". In: 60.3 (1995), pp. 784–795. URL: https://doi.org/10.1190/1.1443817.

[145] Stadler and Igel. "A numerical study on using guided GPR waves along metallic cylinders in boreholes for permittivity sounding". In: *2018 17th International Conference on Ground Penetrating Radar, GPR 2018* (2018). DOI: 10.1109/ICGPR.2018.8441666.

[146] Stratton. "Electromagnetic Theory". In: *Electromagnetic Theory* (1941), pp. 1–6. ISSN: 00319228. DOI: 10.1063/1.2807887. URL: http://books.google.com/books?hl=en&lr=&id=zFeWdS2luE4C&oi=fnd&pg=PA1&dq=Electromagnetic+Theory&ots=8U0f2pbhvl&sig=UWbaZbWf1fQLzS6-JfA1Yh94d_M.

[147] Streich and van der Kruk. "Accurate imaging of Multicomponent GPR data based on exact radiation patterns". In: *IEEE Transactions on Geoscience and Remote Sensing* 45.1 (2007), pp. 93–103. ISSN: 01962892. DOI: 10.1109/TGRS.2006.883459.

[148] Streich and van der Kruk. "Characterizing a GPR antenna system by near-field electric field measurements". In: *Geophysics* 72.5 (2007), A51. ISSN: 00168033. DOI: 10.1190/1.2753832.

[149] Tabarovsky and Rabinovich. "2 . 5-D Modeling in electromagnetic". In: *Applied Geophysics* 35 (1996), pp. 261–284. DOI: 10.1016/0926-9851(96)00025-0.

[150] Tarantola. "A strategy for nonlinear elastic inversion of seismic reflection data". In: *Geophysics* 51.10 (1986), p. 1893. ISSN: 1070485X. DOI: 10.1190/1.1442046. URL: http://library.seg.org/doi/pdf/10.1190/1.1442046.

[151] Tarantola. *Inverse problem theory and Methods for Model Parameter Estimation.* Philadelphia, PA: Society for Industrial and Applied Mathematics, 2005, pp. 1–358. ISBN: 0898715725. URL: http://www.ipgp.fr/~tarantola/Files/Professional/SIAM/InverseProblemTheory.pdf%0Apapers2://publication/uuid/62A7A164-F0E3-4298-AA2B-222FF673BF4E.

[152] Tarantola. *Mapping of Probabilities: Theory for the Interpretation of Uncertain Physical Measurements.* Cambridge University Press, 2007, p. 305.

[153] Tarantola and Valette. "Inverse problems = Quest for information". In: *Journal of Geophysics* 50.1 (1982), pp. 159–170. URL: papers3://publication/uuid/07031B0D-E787-4664-97F4-8BB2E085913D.

[154] Tronicke and Holliger. "Short Note Effects of gas- and water-filled boreholes on the amplitudes of crosshole georadar data as inferred from experimental evidence". In: *Geophysics* 69.5 (2004), pp. 1255–1260. ISSN: 0016-8033. DOI: 10.1190/1.1801942.

[155] Tronicke et al. “Improved crosshole radar tomography by using direct and reflected arrival times”. In: *Journal of Applied Geophysics* 47.2 (2001), pp. 97–105. ISSN: 0926-9851. DOI: https://doi.org/10.1016/S0926-9851(01)00050-7. URL: http://www.sciencedirect.com/science/article/pii/S0926985101000507.

[156] Tronicke et al. “Joint application of surface electrical resistivity- and GPR-measurements for groundwater exploration on the island of Spiekeroog - northern Germany”. In: *Journal of Hydrology* 223.1-2 (1999), pp. 44–53.

[157] Uduwawala. *A Comprehensive Study of Resistor-Loaded Planar Dipole Antennas for Ground Penetrating Radar Applications.* 2006. ISBN: 9171784268.

[158] United Nations. *Transforming our world : The 2030 agenda for sustainable development.* Tech. rep. 2015. DOI: 10.1201/b20466-7. URL: https://sustainabledevelopment.un.org/content/documents/21252030%20Agenda%20for%20Sustainable%20Development%20web.pdf.

[159] Van Coevorden et al. “GA design of a thin-wire bow-tie antenna for GPR applications”. In: *IEEE Transactions on Geoscience and Remote Sensing* 44.4 (2006), pp. 1004–1009. ISSN: 01962892. DOI: 10.1109/TGRS.2005.862264.

[160] van der Kruk. “Three diensional imaging of multi-comonent ground penetrating radar data”. PhD thesis. Technische Universiteit Delft, 2001.

[161] van der Kruk et al. “GPR full-waveform inversion, recent developments, and future opportunities”. In: *2018 17th International Conference on Ground Penetrating Radar, GPR 2018* May 2020 (2018), pp. 1–6. DOI: 10.1109/ICGPR.2018.8441667.

[162] van der Kruk et al. “Improved three dimensional image reconstruction technique for mulit-component ground penetrating radar data”. In: *Subsurface Sensing Technologies and Applications* 4 (2003), pp. 61–99.

[163] Van Vorst et al. “Three-dimensional to two-dimensional data conversion for electromagnetic wave propagation using an acoustic transfer function: application to cross-hole GPR data”. In: *Geophysical Journal International* 198.1 (2014), pp. 474–483. ISSN: 0956-540X. DOI: 10.1093/gji/ggu111. URL: http://gji.oxfordjournals.org/cgi/doi/10.1093/gji/ggu111.

[164] Vidale. “Finite-difference calculation of traveltimes in three dimensions”. In: *GEOPHYSICS* 55.5 (1990), pp. 521–526. DOI: 10.1190/1.1442863. eprint: https://doi.org/10.1190/1.1442863. URL: https://doi.org/10.1190/1.1442863.

[165] Virieux and Operto. “An overview of full-waveform inversion in exploration geophysics”. In: *Geophysics* 74.6 (2009), WCC1–WCC26. DOI: 10.1190/1.3238367. URL: http://geophysics.geoscienceworld.org/content/74/6/WCC1.abstract.

[166] Wada et al. "Global depletion of groundwater resources". In: *Geophysical Research Letters* 37.20 (2010), pp. 1–5. ISSN: 00948276. DOI: 10.1029/2010GL044571.

[167] Warner et al. "Anisotropic 3D full-waveform inversion". In: *Geophysics* 78.2 (2013), R59–R80. ISSN: 0016-8033. DOI: 10.1190/geo2012-0338.1. URL: http://library.seg.org/doi/abs/10.1190/geo2012-0338.1.

[168] Warren and Giannopoulos. "Creating FDTD models of commercial GPR antennas using Taguchi's optimisation method". In: (2011). ISSN: 00168033. DOI: 10.1190/1.3548506. URL: http://hdl.handle.net/1842/5614.

[169] Warren, Giannopoulos, and Giannakis. "gprMax: Open source software to simulate electromagnetic wave propagation for Ground Penetrating Radar". In: *Computer Physics Communications* 209 (2016), pp. 163–170. ISSN: 00104655. DOI: 10.1016/j.cpc.2016.08.020. URL: http://dx.doi.org/10.1016/j.cpc.2016.08.020.

[170] Watson. "Towards 3D full-wave inversion for GPR". In: *2016 IEEE Radar Conference, RadarConf 2016* (2016). DOI: 10.1109/RADAR.2016.7485323.

[171] Weihermüller et al. "Mapping the spatial variation of soil water content at the field scale with different ground penetrating radar techniques". In: *Journal of Hydrology* 340.3-4 (2007), pp. 205–216. ISSN: 00221694. DOI: 10.1016/j.jhydrol.2007.04.013.

[172] Wiggins. "The general linear inverse problem: Implication of surface waves and free oscillations for Earth structure". In: *Reviews of Geophysics* 10.1 (1972), pp. 251–285. ISSN: 8755-1209. DOI: 10.1029/RG010i001p00251. URL: https://doi.org/10.1029/RG010i001p00251.

[173] Williamson. "A guide to the limits of resolution imposed by scattering in ray tomography". In: *Geophysics* 56.2 (1991), p. 202. ISSN: 1070485X. DOI: 10.1190/1.1443032.

[174] Williamson and Pratt. "A critical review of acoustic wave modeling procedures in 2.5 dimensions". In: *Geophysics* 60.2 (1995), p. 591. ISSN: 1070485X. DOI: 10.1190/1.1443798.

[175] Williamson and Worthington. "Resolution limits in ray tomography due to wave behavior: Numerical experiments". In: *Geophysics* 58.5 (1993), p. 727. ISSN: 1070485X. DOI: 10.1190/1.1443457.

[176] World Health Organization. *Protecting Groundwater for Health.* 2006. ISBN: 92 4 154668 9. URL: https://www.who.int/water%7B%5C_%7Dsanitation%7B%5C_%7Dhealth/publications/PGWsection1.pdf?ua=1.

[177] Wu and Toksöz. "Diffraction tomography and multisource holography applied to seismic imaging". In: *Geophysics* 52.1 (1987), pp. 11–25. ISSN: 0016-8033. DOI: 10.1190/1.1442237. URL: http://library.seg.org/doi/10.1190/1.1442237.

[178] Yee. “Numerical solution of initial boundary value problems involving maxwell’s equations in isotropic media”. In: *IEEE Transactions on Antennas and Propagation* 14.3 (1966), pp. 302–307. ISSN: 0018-926X. DOI: 10.1109/TAP.1966.1138693. URL: http://ieeexplore.ieee.org/document/4091372/%20http://ieeexplore.ieee.org/document/1138693/.

[179] Yue et al. “Electromagnetic Full Waveform Inversion based on Bayesian Markov-chain Monte-Carlo Method”. In: January (2016), pp. 428–431. DOI: 10.2991/iceeg-16.2016.115.

[180] Zheng, Bianchi, and Gorelick. “Lessons Learned from 25 Years of Research at the MADE Site”. In: *Groundwater* 49.5 (2011), pp. 649–662. DOI: https://doi.org/10.1111/j.1745-6584.2010.00753.x. eprint: https://ngwa.onlinelibrary.wiley.com/doi/pdf/10.1111/j.1745-6584.2010.00753.x. URL: https://ngwa.onlinelibrary.wiley.com/doi/abs/10.1111/j.1745-6584.2010.00753.x.

[181] Zheng and Gorelick. “Analysis of solute transport in flow fields influenced by preferential flowpaths at the decimeter scale”. In: *Ground Water* 41.2 (2003), pp. 142–155.

Band / Volume 560
Machine Learning in Modeling of the Dynamics of Polymer Electrolyte Fuel Cells
W. Zou (2021), vii, 139 pp
ISBN: 978-3-95806-601-4

Band / Volume 561
Introduction Strategies for Hydrogen Infrastructure
S. Cerniauskas (2021), viii, 179 pp
ISBN: 978-3-95806-602-1

Band / Volume 562
Noble Metal Coated Porous Transport Layers for Polymer Electrolyte Membrane Water Electrolysis
C. Liu (2021), 139 pp
ISBN: 978-3-95806-603-8

Band / Volume 563
Modeling and Diagnosis of the Stratospheric Circulation
E. J. Charlesworth (2021), v, 103, A2 pp
ISBN: 978-3-95806-605-2

Band / Volume 564
Potentialfeldmessungen zur Qualitätsbewertung von Bipolarplatten
M. Sietmann (2021), ix, 160 pp
ISBN: 978-3-95806-606-9

Band / Volume 565
Sequential and coupled inversion of time-lapse borehole GPR measurements for vadose zone model parameterization
Y. Yu (2022), XX, 121 pp
ISBN: 978-3-95806-607-6

Band / Volume 566
Cirrus clouds in the extratropical tropopause and lowermost stratosphere region
I. Bartolomé García (2022), iii, 155 pp
ISBN: 978-3-95806-610-6

Band / Volume 567
Stationary and Transient Behaviour of Polymer Electrolyte Fuel Cells
Y. Shi (2022), viii, 172 pp
ISBN: 978-3-95806-611-3

Band / Volume 568
14th Carolus Magnus Summer School on Plasma and Fusion Energy Physics
D. Reiser (Ed.), (2022), 207 pp
ISBN: 978-3-95806-613-7

Band / Volume 569
Spectral induced polarization of calcite precipitation in porous media
S. Izumoto (2022), xviii, 106 pp
ISBN: 978-3-95806-614-4

Band / Volume 570
Technische und ökonomische Bewertung der Polymer-Elektrolyt-Membran Elektrolyse
S. M. Saba (2022), IV, 263 pp
ISBN: 978-3-95806-615-1

Band / Volume 571
Advanced Sintering of Garnet-Based Ceramic Composite Cathodes for All-Solid-State Lithium Batteries
M. Ihrig (2022), VIII, 160 pp
ISBN: 978-3-95806-616-8

Band / Volume 572
Developing an integrated value-based institutional framework for analyzing nexus governance challenges – the case study of Germany
C. Märker (2022), 290 pp
ISBN: 978-3-95806-617-5

Band / Volume 573
Ecological sanitation via thermophilic co-composting of humanure and biochar as an approach to climate-smart agriculture
D. Castro Herrera (2022), XVIII, 127 pp
ISBN: 978-3-95806-622-9

Band / Volume 574
Towards 3D crosshole GPR full-waveform inversion
A. Mozaffari (2022), viii, 122 pp
ISBN: 978-3-95806-623-6

Weitere ***Schriften des Verlags im Forschungszentrum Jülich*** unter
http://wwwzb1.fz-juelich.de/verlagextern1/index.asp

Energie & Umwelt / Energy & Environment
Band / Volume 574
ISBN 978-3-95806-623-6

JÜLICH
Forschungszentrum